

Figure 4.21 SEM photomicrograph of hydrotalcite membrane prepared from slip casting: two-layer casting and then calcined at 400°C (Top: 10 K mag, Bottom: 20K mag)

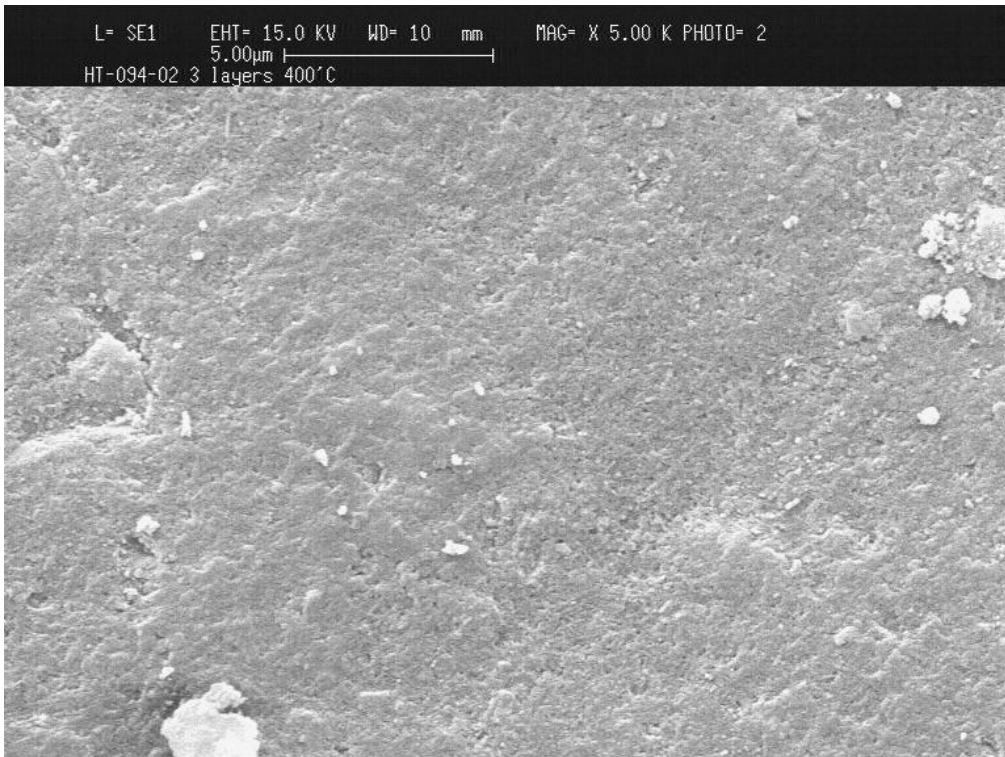
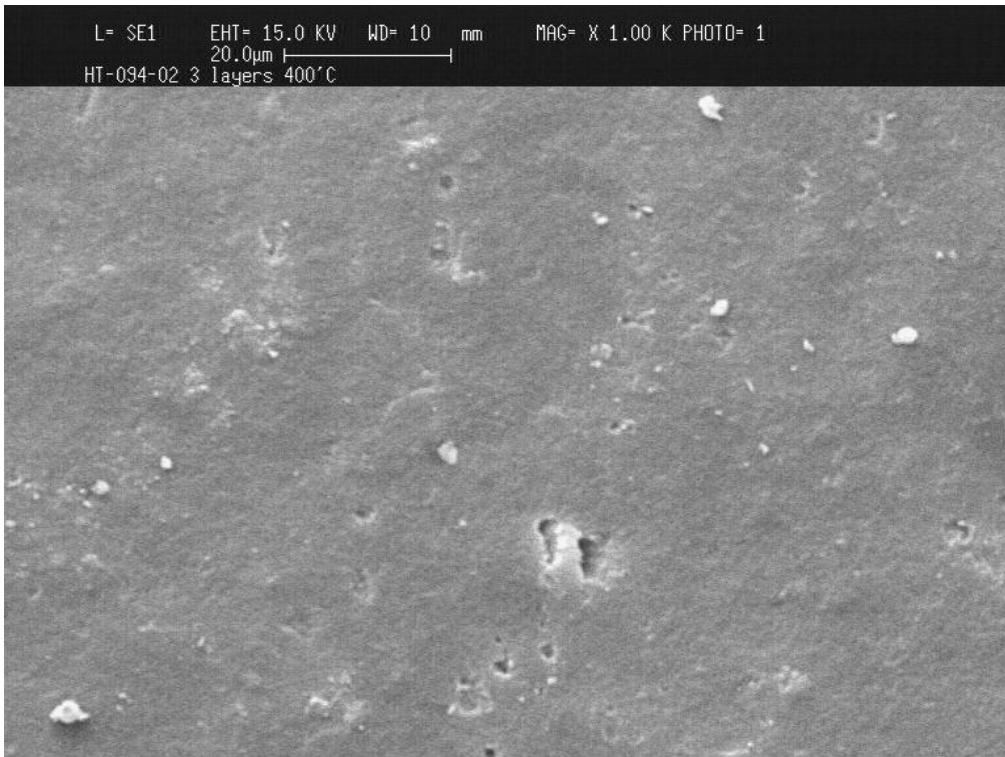


Figure 4.22 SEM photomicrograph of hydrotalcite membrane prepared from slip casting: three-layer casting and then calcined at 400°C (Top: 1 K mag, Bottom: 5K mag)

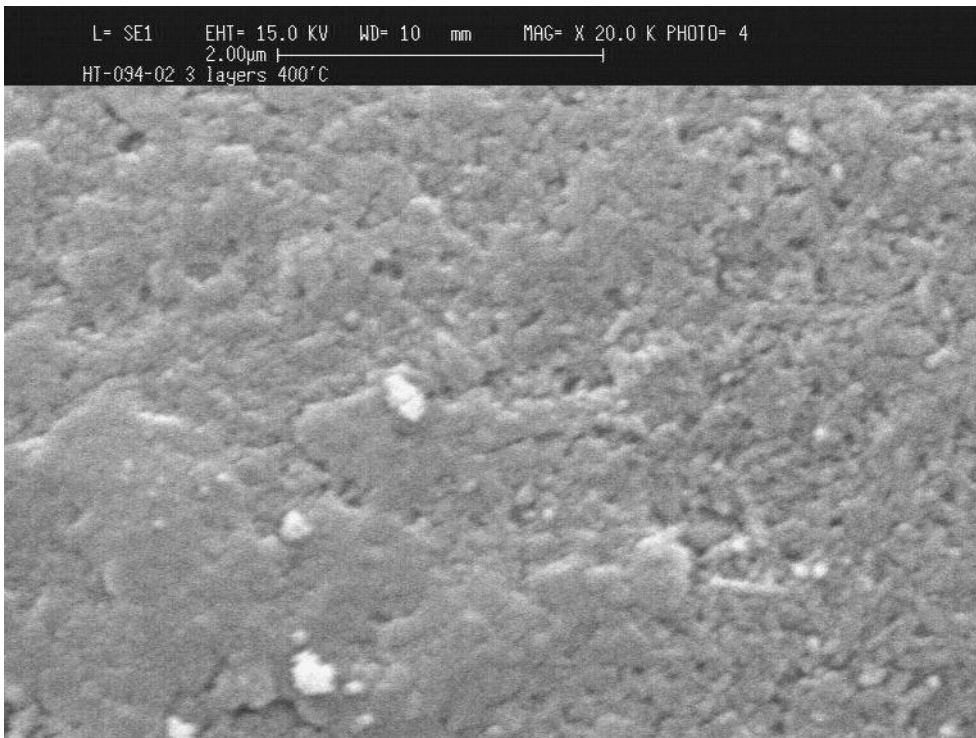
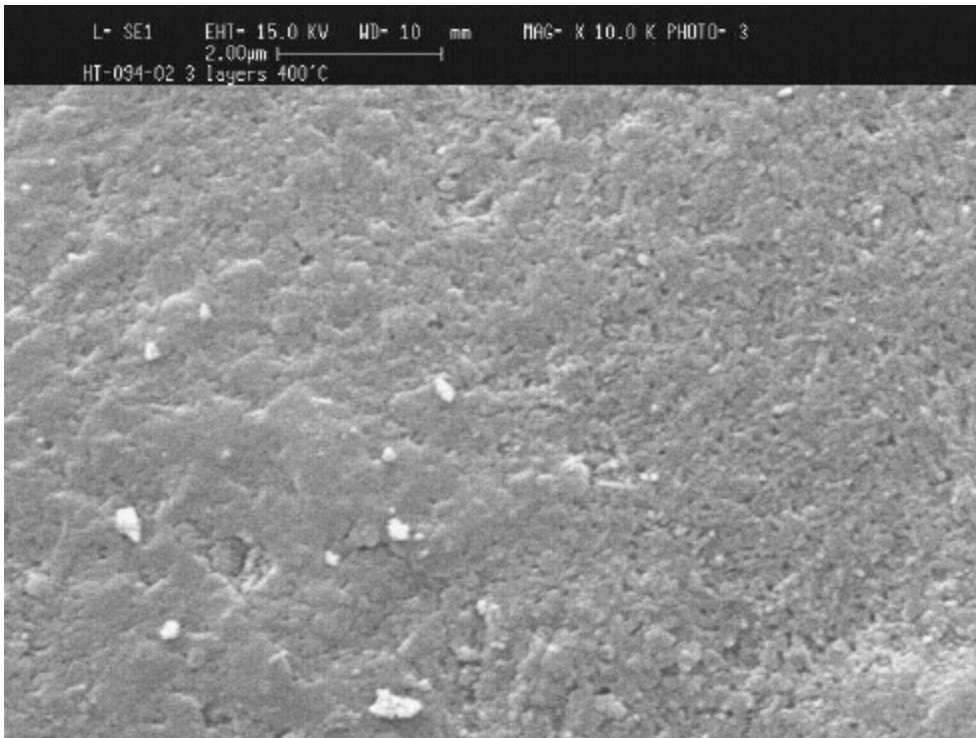


Figure 4.23 SEM photomicrograph of hydrotalcite membrane prepared from slip casting: three layer casting and then calcined at 400°C (Top: 10 K mag, Bottom: 20K mag)

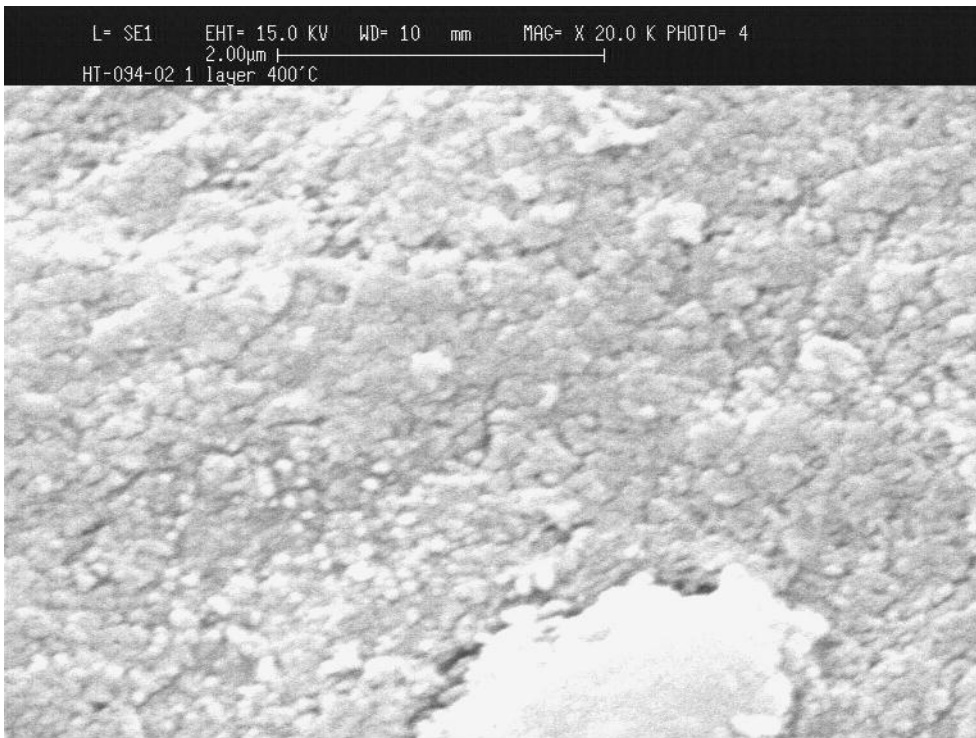
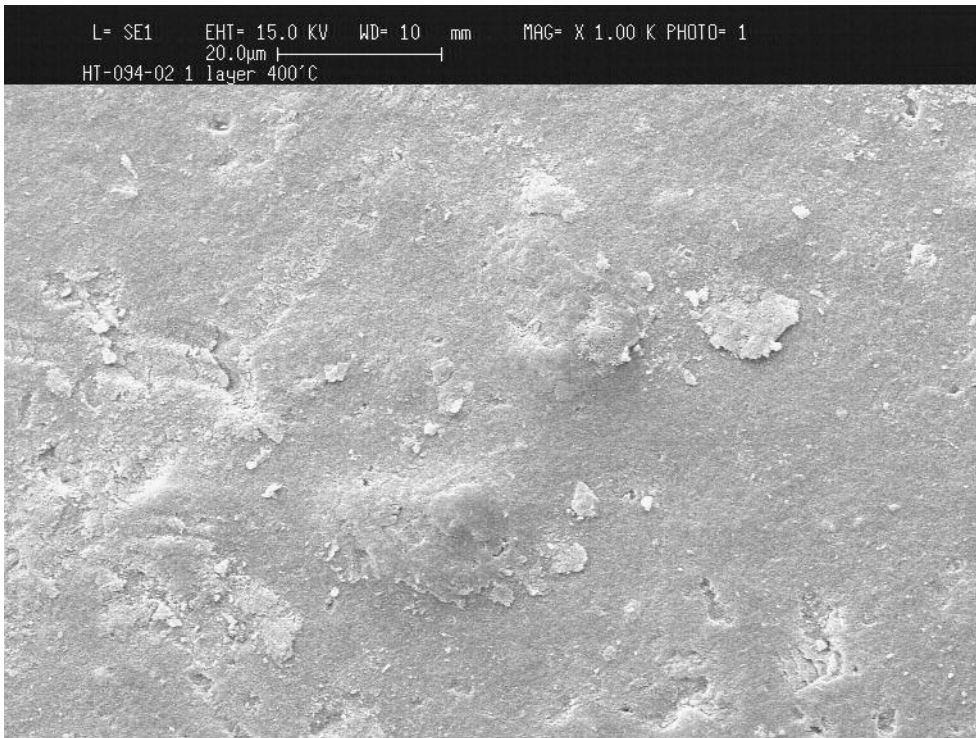


Figure 4.24 SEM photomicrograph of hydrothermal membrane prepared from slip casting: one layer casting, calcined at 400°C, another layer casting and calcined at 400°C. (Top: 1 K mag, Bottom: 20K)

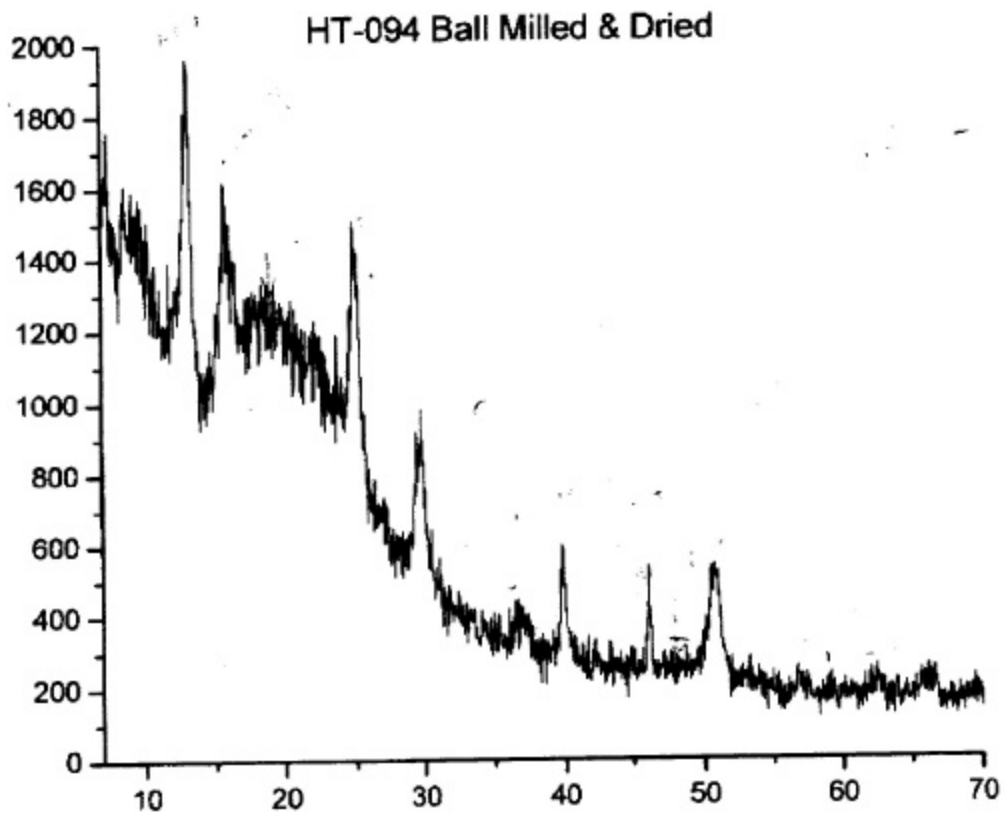


Figure 4.25 XRD of the starting materials used to prepare HT-094-7-1/2 and HT-094-7-1)

## 4.4 Post Treatment via Chemical Vapor Deposition

To avoid non-selective transport through voids between crystals and the base substrate, a chemical vapor deposition/infiltration (CVD/I) technique was proposed. The method has been developed and used by us in the development of our hydrogen selective membranes (SiO<sub>2</sub> and SiC based) [1,2]. Our past experience indicates that a thin (~1 micron) silicon-based film can be deposited on top of the 40Å membrane using tetraethylorthosilicate (TEOS) as a precursor at the temperature of 300°C. To avoid the potential plugging of the hydrotalcite opening, the deposition temperature was lowered to 200°C based upon the TGA study of the hydrotalcite material. CO<sub>2</sub> intercalated within hydrotalcite begin to release at the temperature of ~180°C. It is hoped that TEOS precursor can selectively plug the residual opening at this temperature range. After the deposition, the membrane can be calcined at >200°C to open the channel for reversible transport of CO<sub>2</sub>. Certainly, calcination of the deposited silica layer at the temperature higher than the deposition temperature may introduce additional undesirable pore opening, which is not specific to CO<sub>2</sub>. We do not take this factor into consideration at this moment.

### 4.4.1 Estimation of CO<sub>2</sub> Enhancement by Hydrotalcite Membrane after CVD/I

#### 4.4.1.1 *Experimental*

- To prove the technical feasibility during this project effort, M&P's existing CVD/I technique was employed without modifications in the precursor selection and deposition condition. The precursor used is tetraethylorthosilicate(TEOS), the deposition condition is 300°C. At this temperature, the TGA data obtained previously shows that part of the CO<sub>2</sub> transport channels are opened. However, the TEOS precursor molecule is too large to penetrate these openings in the range of 3 to 6Å. In the feasibility tests, the CVI process was stopped when the reduction in He/O<sub>2</sub> carrier gas permeance was negligible with time.
- Permeances of single components, including He, N<sub>2</sub> and CO<sub>2</sub>, were measured at 300, 400 and 500°C to determine whether the membrane showed any affinity to CO<sub>2</sub>. In our TEOS CVD/I based hydrogen (and helium) selective membranes, the permeance of N<sub>2</sub> (and CO<sub>2</sub>) strictly results from Knudsen flow through defects in the SiO<sub>2</sub> infiltrated layer. Hence, a CO<sub>2</sub> permeance above that expected from Knudsen flow through the defects (which can be estimated from the N<sub>2</sub> permeance) must result from selective transport of CO<sub>2</sub> through the hydrotalcite crystals in the membrane.
- Enhancement of the CO<sub>2</sub> transport by the hydrotalcite material peaks between 300 and 400°C according to the TGA study of this hydrotalcite material. The enhancement diminishes to negligible levels as the temperature is increased much beyond 400°C, since the hydrotalcite material begins to undergo phase change to a mixed oxide at these temperatures.

#### 4.4.1.2 Results and Discussions

- The CVD/I technique was demonstrated to reduce the residual pore openings of the membrane that remained following the in-situ crystallization. Table 4.6 shows that the permeance of a hydrotalcite membrane was reduced from 1.36 to 0.37 m<sup>3</sup>/m<sup>2</sup>/hr/bar at 300°C, indicating that the selected CVD/I condition was sufficient to plug the residual pore openings following in-situ hydrotalcite crystallization.
- SEM/EDX analysis of a 500Å substrate following CVD/I shows that the silicon oxide deposition does not increase the layer thickness of the substrate membrane as evidenced by the grain structure of the top surface of the substrate shown in Figure 4.27. On the other hand, the EDX analysis shows that significant silicon deposition occurs in the first several microns inside the outer surface of the substrate. Thus, it is believed that the CVD/I technique employed here satisfies our performance requirement, specifically, penetration and plugging of the pore openings without indiscriminant deposition of an overlayer on the top of the existing substrate.
- At 300°C, the CO<sub>2</sub> permeance doubled as a result of the enhancement by the hydrotalcite embedded in the pores as shown in Table 4.6. The total CO<sub>2</sub> permeance was 0.26 m<sup>3</sup>/m<sup>2</sup>/hr/bar. It is estimated that the contribution to the CO<sub>2</sub> permeance from defects in the membrane is 0.14 m<sup>3</sup>/m<sup>2</sup>/hr/bar based upon the measured nitrogen permeance and the Knudsen selectivity. Thus, 0.12 m<sup>3</sup>/m<sup>2</sup>/hr/bar is the contribution to the CO<sub>2</sub> permeance due to transport of CO<sub>2</sub> through the CO<sub>2</sub> channels in the hydrotalcite crystals.
- The enhancement at 400°C is reduced to 0.02 m<sup>3</sup>/m<sup>2</sup>/hr/bar using a similar analysis as above. The enhancement is expected to be reduced under this experimental condition, since the low partial pressure of CO<sub>2</sub> does not promote adsorption of the CO<sub>2</sub> molecule at this temperature level. In addition, most of the hydroxyl groups available for forming CO<sub>2</sub> via the carbonate ion may be lost so that the injection of water is also likely to be necessary to promote CO<sub>2</sub> permeance enhancement.

#### 4.4.2 Post-Treatment via Chemical Vapor Deposition

##### 4.4.2.1 Experimental

Two hydrotalcite membranes were CVD/Ied under this section. The first one, HT-IA-40-01 (TEOS-04) was deposited for about ~10 hours at 200°C. A hydrotalcite membrane, HT-IA-45-01, prepared according to the protocol described in Sec. 4.2 (its XRD characterization shown in Figure 4.25) was CVD/I post treated. The permeances of the starting membranes at room temperature are listed below:

Sample ID	No. of In-situ Crystallization	He Permeance (m <sup>3</sup> /m <sup>2</sup> /hr/bar)	N <sub>2</sub> Permeance (m <sup>3</sup> /m <sup>2</sup> /hr/bar)	Selectivity (He/N <sub>2</sub> )
HT-IA-45-01	1	10.75	4.52	2.38
HT-IA-45-01	2	2.47	0.94	2.64

The membrane selectivity of He/N<sub>2</sub> after the 2<sup>nd</sup> in-situ crystallization is about Knudsen selectivity, indicating the membrane likely has minimal defects and is suitable as a starting membrane for CVD/I post treatment.

#### 4.4.2.2 Results/Discussion

The permeances (at room temperature) before and after deposition are listed below:

Treatment	He Permeance (m <sup>3</sup> /m <sup>2</sup> /hr/bar)	N <sub>2</sub> Permeance (m <sup>3</sup> /m <sup>2</sup> /hr/bar)	Selectivity, ideal (He/N <sub>2</sub> )
Before CVD	9.65	3.51	2.75
After CVD	0.1380	0.024	6

The permeances of nitrogen and helium were reduced to a very low level during this extended CVD/I. The selectivity improvement was resulted from the creation of the nanopore by the deposited silica known for its permeability to He and H<sub>2</sub>.

Since the membrane was CVD/Ied at 200°C and then its permeance was measured at >250°C, two factors have to be taken into consideration in data interpretation:

- Membranes treated at the temperature (i.e., 250 and 300°C) higher than the CVD/Ied temperature (200°C) could undergo densification of the CVD/I film, resulting in the decrease in He permeance according to our past experience.
- According to the TGA study, most free water releases at temperature <180°C. Thus, CO<sub>2</sub> permeation after CVD/I takes place in the absence of water. However, if the membrane was stored in the atmosphere subsequently, the permeation could take place in the presence of water adsorbed during the storage.

The helium permeance does not follow Knudsen diffusion as expected. However, it is very obvious that CO<sub>2</sub> permeance is enhanced to higher than Knudsen diffusion as shown in the table. More importantly, the membrane permeance at 300°C follows Knudsen diffusion in terms of N<sub>2</sub>/CO<sub>2</sub> ratio, while the enhancement increases when the temperature decreases from 300 to 250°C and then decreases when the temperature further decreases to 100°C. The maximum CO<sub>2</sub> enhancement in the range of 200 to 300°C is consistent with the TGA study. The unique enhancement at the temperature of 200 to 300°C is indicative of the affinity of CO<sub>2</sub> by hydrotalcite. The enhancement at the low temperature could be contributed by the surface interaction of CO<sub>2</sub> with the metal oxide of the deposited silicon-based material. A similar study with another membrane is presented in Table 4.8, showing a similar trend. More study is required to differentiate the contribution by surface interaction vs intercalated CO<sub>2</sub>.



To double-check this result on enhancement, this membrane was re-measured after storage for several days. The measurement started from room temperature and then went up to 300°C. The result is presented in the same table. In general the trend of the CO<sub>2</sub> enhancement at the temperature 200 to 300°C is reproducible. In this case, however, the helium permeance follows Knudsen diffusion; most likely that the membrane densified as a result of moisture during storage, losing its microporosity for helium permeance. Nitrogen permeance follows Knudsen diffusion except at the low temperature of 100°C, which results from the interaction of CO<sub>2</sub> and metal oxide surface to form carbonate bonds in the presence of water.

To further determine the effectiveness of CVD/I, this membrane was CVD/Ied at 300°C for many hours, to determine the CO<sub>2</sub> permeance under the condition that most defects were plugged. The result is presented in Table 4.9. Evidently the permeances of all gases diminished dramatically. The helium permeance increases significantly due to the formation of micropores at this CVD/I temperature. Again, the CO<sub>2</sub> enhancement was evidently in the temperature range of 200°C.

#### 4.4.3 Effect of CVD/I Time on CO<sub>2</sub> Enhancement

##### 4.4.3.1 Experimental

This membrane was CVDed for up to 40 hours at 200°C. Its permeance was periodically checked during the deposition. Thus, we can determine the degree of CO<sub>2</sub> enhancement vs N<sub>2</sub> permeance decrease. A hydrotalcite membrane (HT-IA-47-3) was selected for this study as shown in Figure 4.26. Its residual permeance after in-situ crystallization is presented in Table 4.10. Its helium permeance increases along with the temperature, likely resulted from the release of water from the membrane during heating.

##### 4.4.3.2 Results and Discussion

Table 4.11 and Figure 4.27 show the He, N<sub>2</sub>, and CO<sub>2</sub> permeances as a function of the CVD/I time. The CO<sub>2</sub> permeance becomes higher than nitrogen permeance after 35 hours of CVD/I at 200°C with this membrane. When the CVD/I was stopped at 40 hours, the N<sub>2</sub>/CO<sub>2</sub> is ~0.8, which is much lower than the Knudsen selectivity of 1.25 at 200°C. The permeance of this membrane was then characterized as a function of temperature from 60 to 250°C as shown in Table 4.12. It was found that both nitrogen and CO<sub>2</sub> permeances increase inversely with the temperature, which is different from the membrane prepared in the previous section. We believe that in addition to CO<sub>2</sub> enhancement by hydrotalcite, it is possible that some surface diffusion may contribute the enhancement at the low temperature.

## 4.5 Conclusions

The LDH-based permselective membrane via the in-situ crystallization technique was successfully developed in this chapter. The performance of this membrane was well characterized. Key conclusions can be drawn from this study as follows:

- Combining the observations from permeance, pore size distribution, EDAX and SEM, we concluded that the hydrotalcite crystals were deposited within the pore size of the starting membranes with the pore sizes of 40Å, 500 Å, and 0.2µm. >90% gas permeance was reduced and the pore size was reduced dramatically, capable of delivering Knudsen selectivity or better. This LDH-based membrane via in-situ crystallization is suitable for post-treatment by the CVD/I technique.
- The permeance reduction and the observations under SEM both offer clear evidence that the post treatment by CVD with the protocol we developed is effective in reducing the residual permeance to a minimum. For instance, the CO<sub>2</sub> permeance of 0.26 m<sup>3</sup>/m<sup>2</sup>/hr/bar at 300°C was observed for one of the membranes after the post treatment by CVD/I technique. Further, our analysis indicates that >50% of the CO<sub>2</sub> permeance is likely attributed to the enhancement by the LDH materials. The balance is contributed by defects remaining in the membrane.
- The ideal selectivity for CO<sub>2</sub>/N<sub>2</sub> ~1.6 at 100 to 300°C was obtained for the hydrotalcite membrane prepared via in-situ crystallization and the CVD/I post treatment. In comparison with the ideal selectivity through Knudsen diffusion of 0.8, the selectivity obtained here is about double of what delivered by the Knudsen diffusion. Evidently, the enhanced selectivity is not sufficient to be commercially viable. An optimization study is necessary to reduce the defect to a minimum via the membrane synthesis; thus, minimal post treatment is required to achieve the CO<sub>2</sub> enhancement without sacrificing permeance significantly.
- The slip casting technology developed here successfully developed a hydrotalcite membrane with the residual pore size of <40Å while remaining most of original permeance intact, i.e., 30 to 40 m<sup>3</sup>/m<sup>2</sup>/hr/bar, which could be an ideal starting material for the post treatment with CVD/I. No post treatment study is performed for this type of the LDH membrane due to the time constraint.

In summary, the CO<sub>2</sub> enhancement via the LDH material was demonstrated in several experimental membranes prepared in this chapter. The two synthesis techniques and one post-treatment technique developed here successfully demonstrated the technical feasibility of the formation of the LDH-based membrane. Additional work with the focus on minimization of defects is recommended to upgrade the CO<sub>2</sub> selectivity and permeance for future commercial use.

Table 4.5 Chemical Vapor Infiltration as a Backpatch for Hydrotalcite Membranes

Samples	Temperature [°C]	Helium Permeance [m <sup>3</sup> /m <sup>2</sup> /hr/bar]	Nitrogen Permeance [m <sup>3</sup> /m <sup>2</sup> /hr/bar]	Experimental He/N <sub>2</sub> Selectivity	Theoretical He/N <sub>2</sub> Selectivity
Before CVD	300	1.36	0.59	2.32	2.65
After CVD	300	0.37	0.16	2.23	2.65

Table 4.6 Chemical Vapor Infiltration as a Backpatch for the Hydrotalcite Membrane. The Improvement in CO<sub>2</sub> Permeance due to Active Transport is shown at various. The CO<sub>2</sub> Permeance in the Defects is Determined Using the Nitrogen Permeance and the Knudsen Selectivity. Permeance is in m<sup>3</sup>/m<sup>2</sup>/hr/bar.

	Temp [°C]	Pres [psi]	He Perm	N <sub>2</sub> Perm	CO <sub>2</sub> Perm	CO <sub>2</sub> Permeance due to Defects	<i>CO<sub>2</sub> Permeance due to Enhanced Transport</i>
Before CVD	300		1.36	0.59	-	-	-
After CVD	300		0.37	0.16	-	-	-
Post -CVD	300	15	0.36	0.17	0.26	0.14	<b>0.13</b>
Post -CVD	400	15	0.46	0.19	0.17	0.15	<b>0.02</b>
Post -CVD	500	15	0.84	0.36	0.29	0.29	<b>0.00</b>

Sample ID	No. of Crystallization	Permeance (m <sup>3</sup> /m <sup>2</sup> /hr/bar)		Selectivity
		He	N <sub>2</sub>	
40Å, typical		~60	~30	~2
HT-IA-60-6	1 <sup>st</sup>	23.34	8.93	2.61
HT-IA-40-4	1 <sup>st</sup>	28.57	11.47	2.49
	2 <sup>nd</sup>	13.98	6.19	2.26
HT-IA-40-5	1 <sup>st</sup>	16.93	6.67	2.54
	2 <sup>nd</sup>	8.75	3.19	2.74
	3 <sup>rd</sup>	8.47	3.24	2.61
Knudsen, theoretical				2.65

Temperature	Permeance (m <sup>3</sup> /m <sup>2</sup> /hr/bar)			Selectivity, ideal			CO <sub>2</sub> Knudsen
	He	N <sub>2</sub>	CO <sub>2</sub>	He/N <sub>2</sub>	He/CO <sub>2</sub>	N <sub>2</sub> /CO <sub>2</sub>	
21	0.507	0.211	0.224				
100	0.686	0.285	0.262	2.41	2.62	1.09	
200	0.713	0.279	0.273	2.56	2.61	1.02	
250	0.708	0.265	0.276	2.67	2.57	0.96	
300	0.82	0.309	0.254	2.65	3.23	1.22	
Theoretical, Knudsen Diffusion				2.65	3.32	1.25	

The membrane was CVDed at 200°C on 7/21 for 4 hrs. Then its performance was measured up to 300°C

Temperature	Permeance (m <sup>3</sup> /m <sup>2</sup> /hr/bar)			Effect of Temperature, (lower T/higher T)			
	He	N <sub>2</sub>	CO <sub>2</sub>	Theoretical	He	N <sub>2</sub>	CO <sub>2</sub>
301	0.82	0.309	0.254				
250	0.708	0.265	0.276	1.048	0.863	0.858	1.087
200	0.713	0.279	0.273	1.052	1.007	1.053	0.989
110	0.686	0.285	0.262	1.051	0.962	1.022	0.960
Theoretical, Knudsen Diffusion							

7/24/2003 (repeated the measurement of the above sample, water may have adsorbed during storage)

Temperature	Permeance (m <sup>3</sup> /m <sup>2</sup> /hr/bar)			Selectivity, ideal			
	He	N <sub>2</sub>	CO <sub>2</sub>	Theoretical	He	N <sub>2</sub>	CO <sub>2</sub> Knudsen
110	0.898	0.377	0.382	2.38	2.35	0.99	
201	0.834	0.324	0.31	2.57	2.69	1.05	
250	0.799	0.311	0.328	2.57	2.44	0.95	
301	0.7911	0.286		2.77			
Theoretical, Knudsen Diffusion				2.65	3.32	1.25	

Temperature	Permeance (m <sup>3</sup> /m <sup>2</sup> /hr/bar)			Effect of Temperature, (lower T/higher T)			
	He	N <sub>2</sub>	CO <sub>2</sub>	Theoretical	He	N <sub>2</sub>	CO <sub>2</sub> Knudsen
301	0.7911	0.286					
250	0.799	0.311	0.328	1.048	1.010	1.087	
200	0.834	0.324	0.31	1.052	1.044	1.042	0.945
110	0.898	0.377	0.382	1.065	1.077	1.164	1.232

7/28/2003	Permeance (m <sup>3</sup> /m <sup>2</sup> /hr/bar)			Selectivity, ideal			
Temperature	He	N <sub>2</sub>	CO <sub>2</sub>	He/N <sub>2</sub>	He/CO <sub>2</sub>	N <sub>2</sub> /CO <sub>2</sub>	CO <sub>2</sub> Knudsen
106	0.0384	0.00186	0.00178	20.65	21.57	1.04	
200	0.0582	0.00117	0.0016	49.74	36.38	0.73	
Theoretical, Knudsen Diffusion				2.65	3.32	1.25	

	Permeance (m <sup>3</sup> /m <sup>2</sup> /hr/bar)			Effect of Temperature, (lower T/higher T)			
Temperature	He	N <sub>2</sub>	CO <sub>2</sub>	Theoretical	He	N <sub>2</sub>	CO <sub>2</sub> Knudsen
200	0.0582	0.00117	0.0016	1.052			
106	0.0384	0.00186	0.00178	1.056	0.660	1.590	1.113

Table 4.10 Permeance vs Temperature of Hydrotalcite Membrane before CVD: TEOS-10 (HT)-47-3

**TEOS-HT-10 (HT-47-3)**

As received				2.65 (theoretical)	3.32 (theoretical)	1.25 (theoretical)
Temp ©	He (m <sup>3</sup> /m <sup>2</sup> /hr/bar)	N <sub>2</sub> (m <sup>3</sup> /m <sup>2</sup> /hr/bar)	CO <sub>2</sub> (m <sup>3</sup> /m <sup>2</sup> /hr/bar)	He/N <sub>2</sub>	He/CO <sub>2</sub>	N <sub>2</sub> /CO <sub>2</sub>
25	2.98	1.53		1.95		
200	3.18	1.61	1.29	1.98	2.47	1.25

Table 4.11 Permeances vs CVD Time of Hydrotalcite Membrane TEOS-HT-10 (HT-IA-47-3)A

8/18/2003							CO <sub>2</sub> Knudsen	at 200C CVD (hr)	Cumulative CVD(hr)	
Temp	He	N <sub>2</sub>	CO <sub>2</sub>	He/N <sub>2</sub>	He/CO <sub>2</sub>	N <sub>2</sub> /CO <sub>2</sub>				
200	3.18	1.61	1.29	1.98	2.47	1.25		0	0	
200	2.67	1.08	0.897	2.47	2.98	1.20		3.2	3.2	
200	1.74	0.692	0.598	2.51	2.91	1.16		11	14.2	
200	1.14	0.417	0.385	2.73	2.96	1.08		9.3	23.5	
201	0.69	0.278	0.265	2.48	2.60	1.05		6.6	30.1	
200	0.45	0.144	0.143	3.13	3.15	1.01		5.3	35.4	
250	0.505	0.189	0.162	2.67	3.12	1.17		0	36	35.4 actual
200	0.596	0.185	0.219	3.22	2.72	0.84		0	36.5	cool down overnight
250	0.556	0.142	0.167	3.92	3.33	0.85		3.7	40.2	before reheating to 200C
200	0.586	0.155	0.193	3.78	3.04	0.80		0	40.5	40.2

Table 4.12 Permeance vs Temperature of Hydrotalcite Membrane after CVD: TEOS-10 (HT-47-3)  
8/27/2003

Temperature ©	Permeance (m3/m2/hr/bar)			Selectivity, ideal			
	He	N2	CO2	He/N2	He/CO2	N2/CO2	CO2 Knudsen
250	0.556	0.142	0.169	3.92	3.29	0.84	
200	0.5855	0.155	0.193	3.78	3.03	0.80	
150	0.578	0.156	0.2195	3.71	2.63	0.71	
100	0.566	0.166	0.255	3.41	2.22	0.65	
60	0.548	0.181	0.288	3.03	1.90	0.63	
Theoretical, Knudsen Diffusion				2.65	3.32	1.25	

Temperature ©	Permeance (m3/m2/hr/bar)			Effect of Temperature, (lower T/higher T)			
	He	N2	CO2	Theoretical	He	N2	CO2
250	0.556	0.142	0.169				
200	0.5855	0.155	0.193	1.052	1.053	1.092	1.142
150	0.578	0.156	0.2195	1.056	0.987	1.006	1.137
100	0.566	0.166	0.255	1.065	0.979	1.064	1.162
60	0.548	0.181	0.288	1.058	0.968	1.090	1.129

Note: Theoretical ratio is based upon Knudsen diffusion

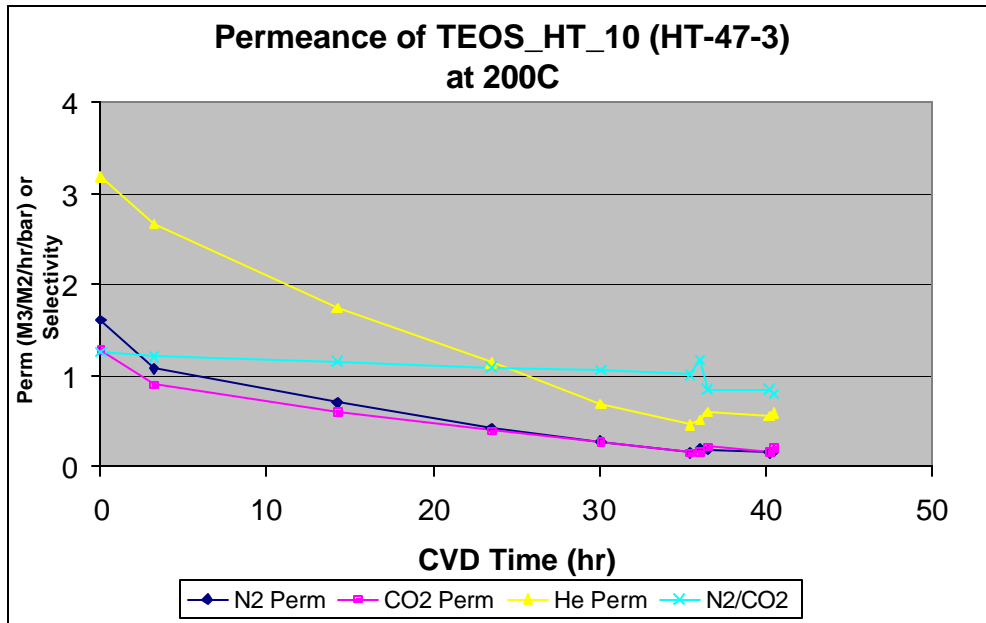


Figure 4.26 Permeance of TEOS HT 10(HT-47-3) at 200C

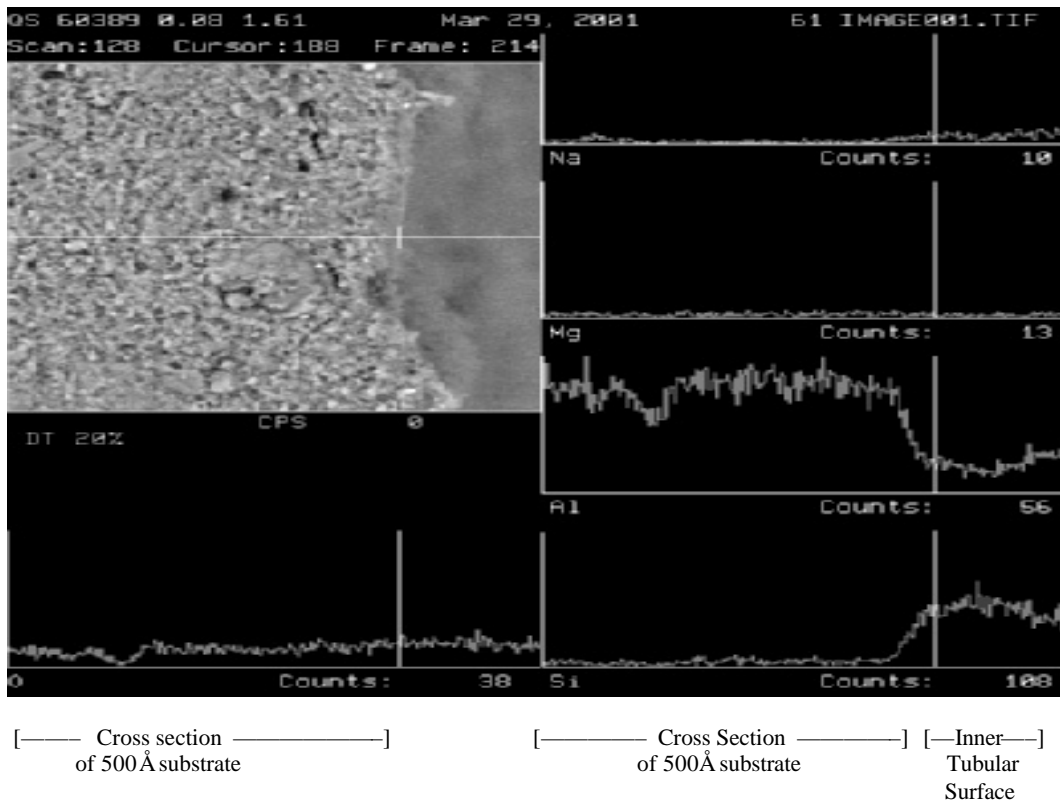


Figure 4.27 SEM Photomicrograph and EDX of the substrate after CVI. No visible layer deposition was observed from SEM. Significant SiC precursor of CVD was observed on the inner tubular surface with very limited penetration into the substrate. The results indicate the CVD/I infiltrates into the porous structure of the substrate to form an ultra-thin effective membrane.

### **Literature Cited**

1. Wu., J.C.S., Sabol, H.K., Smith, OW., Flowers, D.F., Liu, P.K.T., J. Membrane Science,96, 275 (1994).
2. Liu, P.K.T., and Wu, J.C.S., U.S. Patent 5.415.891, May 16(1995).
3. Corning Ceramic Bulletin on Pyroceram.



## Chapter 5

### Development of CO<sub>2</sub>-Affinity Membranes with Carbonaceous

#### 5.1 Introduction/Literature Study

Two different types of CO<sub>2</sub>-affinity membranes were explored throughout this project for the purpose of hydrogen production with concomitant CO<sub>2</sub> removal via water gas shift reaction. One (Type I) as discussed in Chapter 4 is based upon the LDH material which has demonstrated a unique affinity to CO<sub>2</sub> at a high temperature in the presence of steam. The other one (Type II), the carbonaceous microporous membrane, which exhibits surface affinity to CO<sub>2</sub>, is discussed in this chapter. These two materials offer commercially viable separation media for implementing the membrane reactor concept (MR) for WGS reaction. In this chapter, the representative performance of the Type II membranes we prepared and characterized is presented.

A literature search was performed to review the literature available for CO<sub>2</sub>/N<sub>2</sub> or CO<sub>2</sub>/CH<sub>4</sub> separation at a high temperature, i.e., >100°C as an indication of the CO<sub>2</sub> affinity for the proposed application environment. Moon *et al.* [2] reported the selectivity of CO<sub>2</sub>/N<sub>2</sub> of ~12 at 100°C, and then declined to ~10 at 168°C in a mixture separation environment using the membrane of methyltriethoxysilane templating silica/α-alumina composite membrane. Another study [1] using polybenzimidazole membrane exhibited the selectivity of ~50 for CO<sub>2</sub>/CH<sub>4</sub> at ~300°C. Its selectivity is lower at a lower temperature. However, its permeance of CO<sub>2</sub> is extremely low, e.g., ~0.002 to 0.003 m<sup>3</sup>/m<sup>2</sup>/hr/bar. There are several zeolitic and other membranes published for CO<sub>2</sub>/CH<sub>4</sub> separations at a lower temperature range [3,4]. In summary, there are few literature studies known to us showing membranes with CO<sub>2</sub> affinity at a high temperature.

In this chapter, the CO<sub>2</sub> permeance and selectivity of the proposed Type II membrane experimentally determined at the LTS/WGS reaction temperature, i.e., 200-250°C are presented.

#### 5.2 Experimental

Using our commercial ceramic membranes as starting substrates, numerous CO<sub>2</sub>-affinity carbonaceous thin film has been deposited on the inside of the tubular membrane for the proposed CO<sub>2</sub> sequestration application with the concomitant hydrogen production. Experimental activities involved in this type of membranes are highlighted below:

1. A series of Type II membranes (10" L) have been prepared using our commercial ceramic membranes as substrate. They are first deposited with selected polymeric precursors and then calcined at a selected temperature to form the desired pore size and surface properties. The single component gas permeation study was performed to

measure their permeances of CO<sub>2</sub>, N<sub>2</sub> and others at 25, 120, 180 and sometimes 220°C.

2. The protocol developed for 10" L was employed for the preparation of the 30" L membrane to evaluate its scale up possibility. The 30" L membranes were characterized for its CO<sub>2</sub> and N<sub>2</sub> permeances at a similar temperature range.
3. One of the 10" L membranes was deposited an additional membrane layer to evaluate the potential improvement in selectivity via pore size reduction. The additional layer was prepared and characterized following a similar protocol as above.

### 5.3 Results and Discussion

- SEM photomicrograph was taken for the CMS membrane prepared in this chapter as shown in Figure 5.1. A very thin CMS layer was deposited on our commercial nanoporous ceramic membrane. The membrane surface appears smooth and defect free although the actual pore size is much smaller than the resolution achievable by SEM.
- Table 5.1 summarizes all the membranes prepared and characterized for this project. Their single component permeances (including He, H<sub>2</sub>, N<sub>2</sub>, and CO<sub>2</sub>, and CH<sub>4</sub>) at 23 to 220°C were presented. Then ideal selectivities were calculated. CO<sub>2</sub> permeance vs selectivity (over N<sub>2</sub>) at 120°C for all the 10" L membranes is presented in Figure 5.2. In general, the overall trend for permeance vs selectivity follows the familiar inverse relationship. When the CO<sub>2</sub> permeance is  $> 3 \text{ m}^3/\text{m}^2/\text{hr}/\text{bar}$ , the selectivity for CO<sub>2</sub>/N<sub>2</sub> ranges from 2 to 4. On the other hand, when the CO<sub>2</sub> permeance is  $< 0.5 \text{ m}^3/\text{m}^2/\text{hr}/\text{bar}$ , the selectivity between 6 and 12 is obtained. In comparison with the Knudsen selectivity of 0.798, our selectivities obtained here are definitely enhanced to much beyond the Knudsen selectivity.
- Majority of the membrane tubes were prepared with a lab scale substrate, i.e., 10" L as presented in Table 5.1. Four 30" long tubes were prepared following the same protocol as the 10" L tubes. The permeance and selectivity obtained from the 30" L are in line with the trend established by the 10" tubes. Thus, the scale-up from the lab scale (10" L) to the full scale of 30" L appears acceptable.
- The permeances and selectivities at 180 to 220°C were presented in Figure 5.3. This temperature range is the usual temperature range for the LTS-WGS as we proposed. Since the data points at these temperatures were much fewer than those of the 120°C shown in Figure 5.2, the permeance vs selectivity trend was not well defined. However, the permeance and selectivity fell within the range of 0.5 to 2.5  $\text{m}^3/\text{m}^2/\text{hr}/\text{bar}$  and 4 to 8, respectively. In comparison with the data obtained at a lower temperature, i.e., 120°C, the selectivity at the higher temperature is somewhat lower than that at the lower temperature.
- Figures 5.4a to 5.4c show the effect of temperature on the CO<sub>2</sub> permeance from 120 to 180°C. It appears that CO<sub>2</sub> permeance decreases along with the temperature increase. For Figure 5.4a and 5.4b, about 50% reduction of the CO<sub>2</sub> permeance was

observed along with the temperature increase in this range. The CO<sub>2</sub> permeance reduction ratio for Figure 5.4c, however, is <<50%. The helium permeance decreases in Figure 5.4b while increases in Figure 5.4c, so is the trend for the hydrogen permeance. It is possible that the majority of the pore size in Figure 5.4a and 5.4b are larger than those in Figure 5.4c; thus, the helium and hydrogen permeances are somewhat influenced by the Knudsen diffusion in Figure 5.4b, while the helium and hydrogen permeances are dominated by activated diffusion in Figure 5.4c. Since the CO<sub>2</sub> permeance reduction vs temperature in Figure 5.4a and 5.4b is much more severe than the theoretical prediction based upon the Knudsen diffusion (i.e., 7%), it is concluded that the permeance for CO<sub>2</sub> is at least partially contributed by another mechanism, surface diffusion. When the pore size is small enough as shown in Figure 5.4c, the surface diffusion contribution decreases and the molecular sieving effect becomes emerged. Even with the pore size decreases in Figure 5.4c, no improvement in CO<sub>2</sub> selectivity was observed. Thus, it is believed that the separation mechanism for this type of material is contributed by both surface diffusion and molecular sieving. At the temperature range interested to us, both mechanisms are likely involved.

- Table 5.2 presents the permeance and selectivity for the membrane with an additional layer of deposition and calcination for the purpose of narrowing the pore size. The result indicated no improvement in selectivity although the permeance was reduced dramatically, from 1.88 to 0.035 m<sup>3</sup>/m<sup>2</sup>/hr/bar. This is consistent with the mechanisms proposed above. The pore size reduction theoretically could improve the selectivity although the difference in the kinetic diameters of CO<sub>2</sub> vs N<sub>2</sub> is very smaller. On the other hand, when the pore size becomes small, the surface diffusion contribution is diminished. Thus, the permeance is reduced dramatically while no clear sign of selectivity improvement is observed.

## 5.4 Conclusions

The Type II CO<sub>2</sub> affinity membranes prepared in this project demonstrated significant selectivity for CO<sub>2</sub>/N<sub>2</sub>, i.e., 4 to 10, up to 220°C, which was much beyond the Knudsen selectivity. Surface affinity of the membrane toward CO<sub>2</sub> was identified as the dominating mechanism at this operating temperature range. Selectivity at this level is comparable or higher than the selectivity of CO<sub>2</sub>/N<sub>2</sub> reported in the literature at the proposed temperature reaction. Pore size reduction was attempted without any success in boosting the CO<sub>2</sub> affinity. Additional study including characterization of this type of membrane in a mixture environment is recommended for future development.

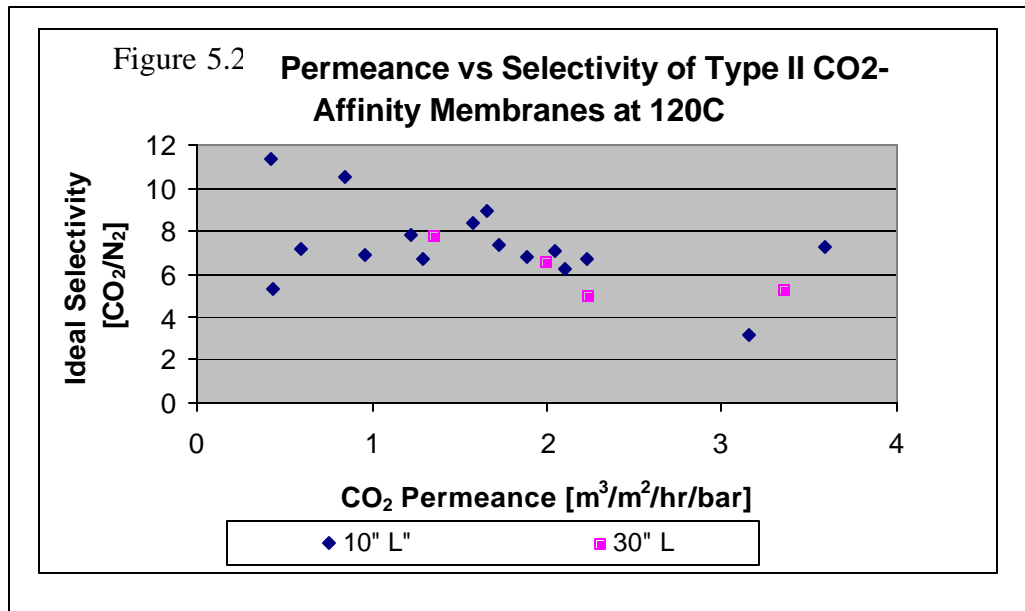
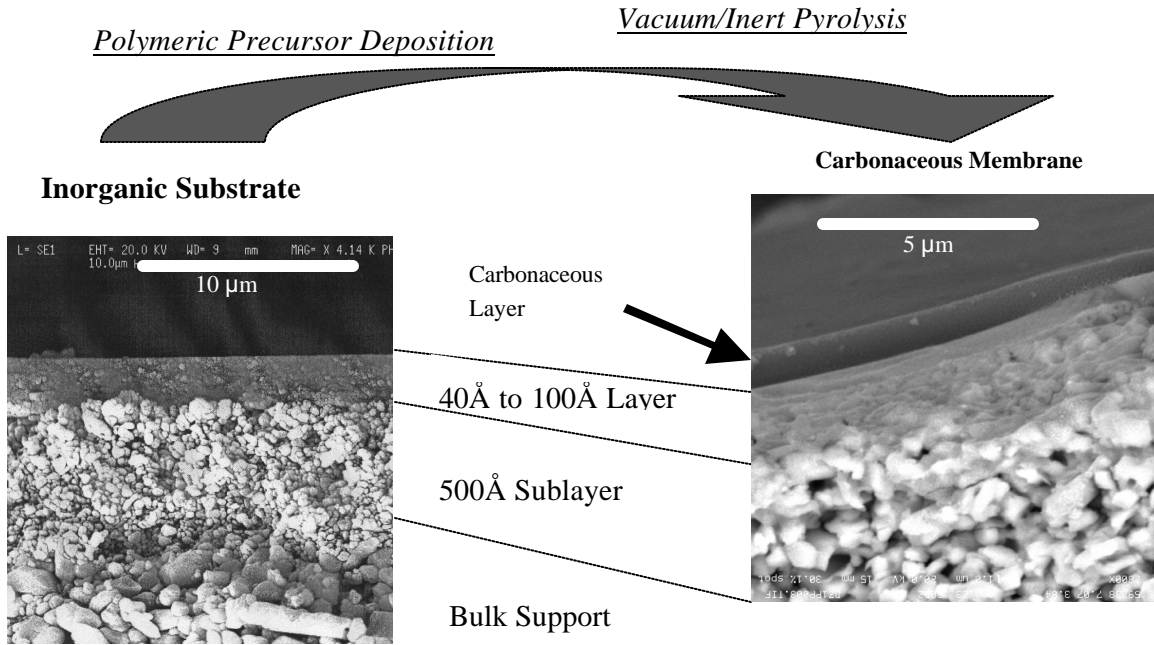
## Literature Cited

1. Pesiri, d. R., B. Jorgensen, and R. C. Dye, "Thermal optimization of polybenzimidazole meniscus membranes for the separation of hydrogen, methane, and carbon dioxide", *J. Memb. Sci.*, 218, 11(2003)
2. Moon, J. H., Y. Park, M. Kim, s. Hyun, and C. Lee, "Permeation and separation of a carbon dioxide/nitrogen mixture in a methyltriethoxysilane templating silica/alumina composite membrane", *J. Memb. Sci.*, 250, 195(2005)
3. Houston, K. s., d. H. Weinkauf, f. F. Stewart, "Characterization of gas transport in selected rubbery amorphous polyphosphazene membranes", *J. Memb. Sci.*, 186, 249(2001)
4. Li, s., G. Alvarado, R. d. Noble, J. L. Falconer, "Effects of impurities on CO<sub>2</sub>/CH<sub>4</sub> separations through SAO-34 membranes", *J. Memb. Sci.*, 251, 59(2005).

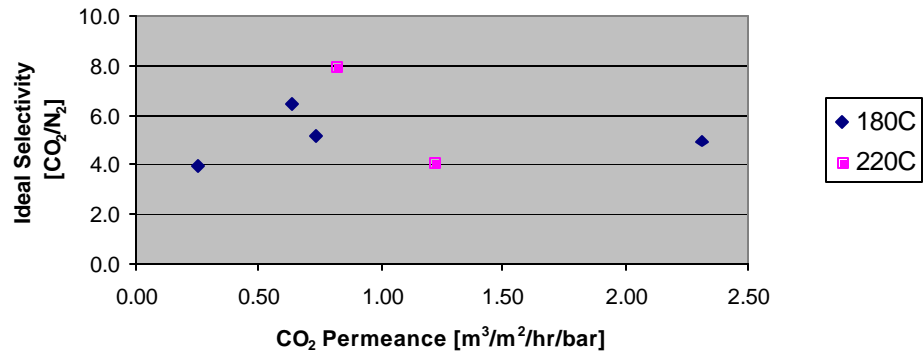
**Table 5.1 Summary of Type II CO<sub>2</sub> Affinity Membranes and their Performance Characterization**

Sample ID	Temp [c]	Press [psi]	Permeance			[m <sup>3</sup> /m <sup>2</sup> /hr/bar]			Ideal Selectivity			
			He	H <sub>2</sub>		N <sub>2</sub>	CO <sub>2</sub>	CH <sub>4</sub>	He/N <sub>2</sub>	H <sub>2</sub> /N <sub>2</sub>	CO <sub>2</sub> /N <sub>2</sub>	N <sub>2</sub> /CH <sub>4</sub>
<b>10" CO2 Affinity Membranes</b>												
NN-01-2	23	30	2.051	3.846	0.748	4.011			2.7	5.1	5.4	
	120	30	1.765	4.198	0.330	2.239			5.3	12.7	6.8	
NN-02&03	120	20	1.231	2.816	0.080	0.846			15.3	35.1	10.6	
	180	20	1.483	3.039	0.097	0.633			15.2	31.2	6.5	
NN-06-03	180	20	1.203	2.753	0.140	0.730	0.098		8.6	19.6	5.2	1.4
	120	20		2.939	0.155	1.216			19.0	7.8		
NN-10-03	120	20	0.541	1.373	0.081	0.432	0.059		6.7	16.9	5.3	1.4
	180	20	0.585	1.227	0.064	0.254			9.1	19.1	4.0	1.4
NN-14	120	30	2.804	5.529	0.998	3.152			2.8	5.5	3.2	
NN-15	120	20	1.171	1.866	0.083	0.595	0.089		14.2	22.6	7.2	0.9
NN-47	120	20	3.429	7.344	0.276	1.880	0.157		12.4	26.6	6.8	1.8
NN-66	120	20	2.420	6.362	0.188	1.578	0.092		12.9	33.9	8.4	2.0
NN-71	120	20	0.707	1.804	0.037	0.418			19.2	48.9	11.3	
NN-80	120	20	2.868	7.464	0.494	3.585	0.523		5.8	15.1	7.3	0.9
	180	20	3.215	7.285	0.470	2.315	0.458		6.8	15.5	4.9	1.0
	120	30	2.010	4.646	0.185	1.655	0.169		10.9	25.2	9.0	1.1
NN-81	120	20	2.642	6.129	0.289	2.048			9.1	21.2	7.1	
NN-82	120	20	1.654	4.349	0.234	1.726	0.112		7.1	18.6	7.4	2.1
NN-94	120	20	1.819	4.250	0.335	2.110	0.355		5.4	12.7	6.3	0.9
	120	20	1.545	3.462	0.191	1.288	0.173		8.1	18.1	6.7	1.1
<b>30" Length CO2 Affinity Membranes</b>												
NN-27	120	20	1.370	3.106	0.445	2.229			3.1	7.0	5.0	
NN-29	120	20	1.643	4.650	0.304	1.994	0.200		5.4	15.3	6.6	1.5
	220	20	2.015	4.544	0.299	1.222	0.215		6.7	15.2	4.1	1.4
NN-30	120	20	0.990	2.956	0.176	1.360			5.6	16.8	7.7	
	220	20	0.879	2.082	0.103	0.821			8.5	20.1	7.9	
NN-49	120	20	2.136		0.632	3.354			3.4		5.3	

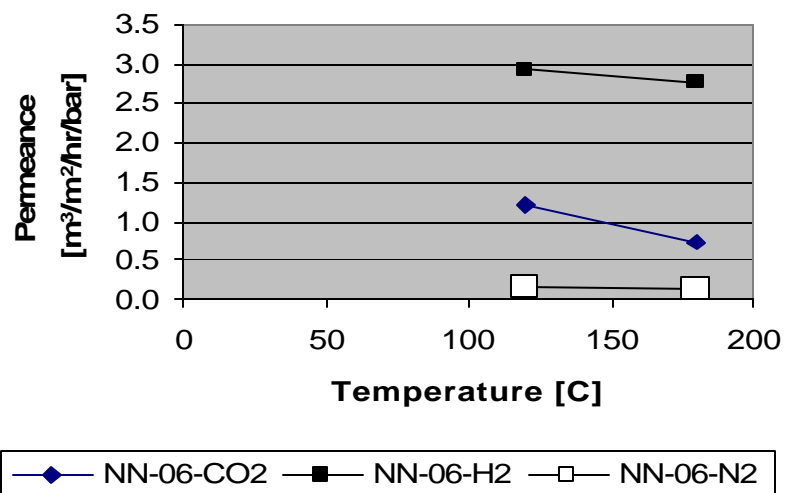
Figure 5.1 Synthesis of Carbonaceous CO<sub>2</sub>- Affinity Membrane



**Figure 5.3 Permeance vs Selectivity of Carbonaceous CO<sub>2</sub>-Affinity Membranes at 180 and 220°C**



**Figure 5.4a Permeance vs Temperature of Carbonaceous CO<sub>2</sub> Affinity Membrane (NN-06)**



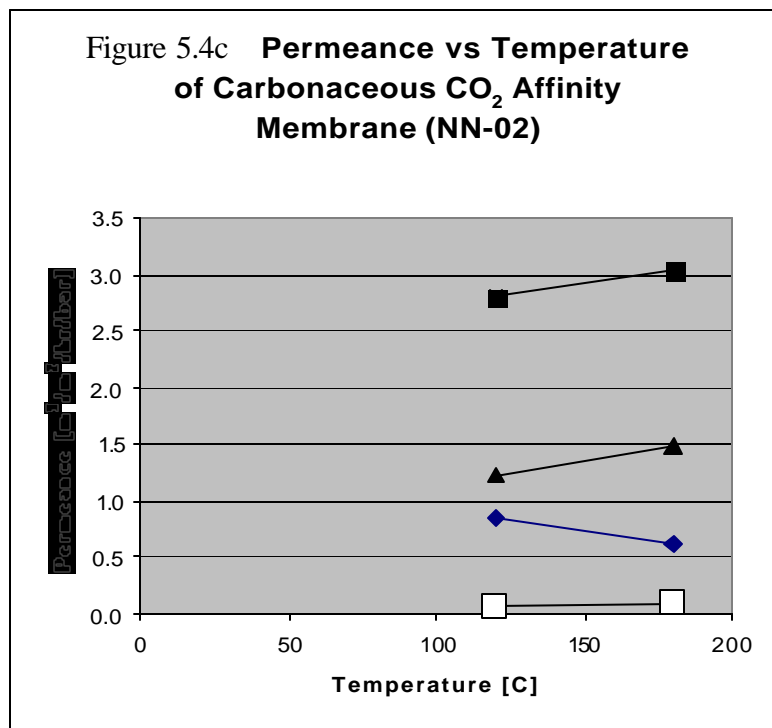
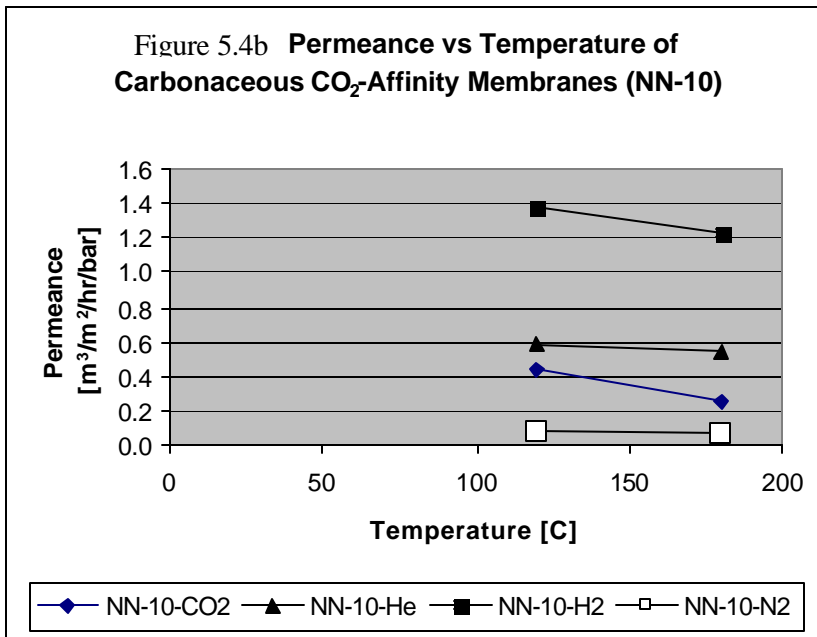


Table 5.2 Effect of Additional Layer Deposition on Performance of Type II CO<sub>2</sub>Affinity Membrane

Sample ID	Notes	Temp [c]	Press [psi]	Permeance [m <sup>3</sup> /m <sup>2</sup> /hr/bar]								
				He	H <sub>2</sub>	N <sub>2</sub>	CO <sub>2</sub>	CH <sub>4</sub>	He/N <sub>2</sub>	H <sub>2</sub> /N <sub>2</sub>	CO <sub>2</sub> /N <sub>2</sub>	N <sub>2</sub> /CH <sub>4</sub>
NN-47		120	20	3.429	7.344	0.276	1.880	0.157	12.4	26.6	6.8	1.8
	additional deposition and firing	120	20	0.665	0.965	0.044	0.035	0.044	15.2	22.0	0.8	1.0



## Chapter 6

### Diffusivity and Adsorption Isotherms of Carbon Dioxide in Mg-Al-CO<sub>3</sub> LDH at Elevated Temperatures

#### 6.1 Introduction/Literature Review

In addition to its use as a membrane, the LDH material is an ideal CO<sub>2</sub> adsorbent for CO<sub>2</sub> sequestration application. The CO<sub>2</sub> diffusivity and adsorption capacity of the LDH material allow us to gauge its value as an adsorbent. The transport characteristics and adsorption isotherms of carbon dioxide on Mg-Al-CO<sub>3</sub> LDH were investigated using CO<sub>2</sub> uptake data measured gravimetrically in the temperature range of 200~250 °C, targeting the low temperature shift of water gas shift reaction. The gravimetric method for uptake rate measurements is simple and straightforward. Several research groups reported the value of CO<sub>2</sub> diffusivity data measured by this method at ambient temperature, as shown in Table 6.1. For the transport properties reported here, the transient CO<sub>2</sub> uptake data were measured gravimetrically at each elevated temperature, and then the diffusion coefficient was estimated by fitting acquired experimental data to the solution of the relevant diffusion equation. In addition to providing the experimental results, the obtained diffusivities are compared with molecular dynamic simulation results from a parallel research project. Adsorption isotherm data were also acquired by the gravimetric method, and the experimental data were fitted with the Langmuir equation and various empirical adsorption isotherm equations.

Table 6.1 Diffusivity data ( $D/r^2$ ) for CO<sub>2</sub> measured by the gravimetric method.

Adsorbent	$D/r^2, s^{-1}$	Temperature, K	References
Coconut derived CMS	$7 \times 10^{-2}$	273	6
Bergbau Forschung CMS	$5 \times 10^{-6}$	298	7
Zr-pillared clay	$8 \times 10^{-2}$	298	8
Own zeolite crystals (7.3-34 $\mu\text{m}$ )	$4.7 \times 10^{-5}$	500	9
LDH2 ( $r \sim 100 \mu\text{m}$ )	$3.6 \times 10^{-4}$	473	This work

LDH2 ( $r \sim 100 \mu\text{m}$ )	$8.9 \times 10^4$	498	This work
LDH2 ( $r \sim 100 \mu\text{m}$ )	$1.3 \times 10^3$	523	This work

During the course of diffusivity and adsorption isotherm experiments, it was found that the equilibrium uptake amount of CO<sub>2</sub> by Mg-Al-CO<sub>3</sub> used in this study was dependent upon the particle size. When LDH2 was utilized for CO<sub>2</sub> uptake without fractionating the LDH2 particles by size, the overall equilibrium uptake amount was ~2 wt%. However, when the sieved LDH2 of the average radius of 100 μm particles was used, the overall uptake of CO<sub>2</sub> was ~1.1 wt%. Since the only difference between above experiments was particle size of LDH2 selected, it seems that particle size of LDH affects the transport and sorption properties. The LDH particle size effect on the CO<sub>2</sub> adsorption capacity has not been reported in the published literature so far, but several research groups have reported about particle size effect on their adsorption experiments. For example, Badruzzaman *et al.* observed that there was a nonlinear relationship between surface diffusivity and particle radius for arsenate adsorption onto granular ferric hydroxide[2]. And, unlike the observation of Badruzzaman *et al.*, Grande *et al.* reported that the adsorption capacity of propane and propylene was independent of the crystal size in their research with synthesized 4A zeolites[3].

## 6.2 Experimental

- Sample Preparation and Measurements for LDH2...One of Mg-Al-CO<sub>3</sub> LDH samples was provided by Media and Process Technology, Inc., of Pittsburgh, PA. The composition of the sample was Mg<sub>0.645</sub>Al<sub>0.355</sub>(OH)<sub>2</sub>(CO<sub>3</sub>)<sub>0.178</sub> · 0.105(H<sub>2</sub>O) as determined by ICP and TGA, and this was the LDH2 sample previously studied in Chapter 3 for sorption reversibility. Prior to the diffusivity and adsorption isotherm experiments the LDH2 sample was sieved, and only particles radii within the range 90~105 μm were retained. For CO<sub>2</sub> uptake measurement, 100-120 mg of a freshly sieved LDH2 sample was utilized for each diffusivity and isotherm experiments. UHP dry CO<sub>2</sub> and UHP dry argon gas mixtures were prepared with Brooks 5850E mass flow controllers and sorption data were recorded by a Cahn TGA 121 instrument. The LDH sample was spread out at room temperature, as thinly as possible, on a bowl-shape quartz container in order to minimize external mass transfer resistance. The sample was then heated to a preset temperature in UHP dry argon (at a flow rate of 30 mL/min) with a heating rate of 5°C/min. Ar was utilized as a purge gas in order to minimize the buoyancy force effect when the purge gas was switched to dry CO<sub>2</sub>. The temperature of experiments was selected between 200 and 250°C since (i) the interlayer water of LDH can be removed without significant transformation of LDH structure in this range as outlined in Chapter 2, and, (ii) based on the results of preliminary experiments at temperatures less than 190 °C, there was no significant uptake of CO<sub>2</sub> in LDH2. When the temperature reached the preset point, the sorption system was kept at the same temperature for 70 min to stabilize the TGA

microbalance. Only after the microbalance showed less than 10 $\mu$ g change, the purge gas was then switched to carbon dioxide with the flow rate of 30 ml/min. However, for the adsorption isotherm experiments, the purge gas was switched to an argon and CO<sub>2</sub> gas mixture with preset compositions instead of pure CO<sub>2</sub>.

- **Sample Preparation and Measurements for LDH3...** The other LDH sample (LDH3) was synthesized by the typical co-precipitation reaction from aqueous solution[4-5] to investigate the particle size effect, and its chemical composition was Mg<sub>0.743</sub>Al<sub>0.257</sub>(OH)<sub>2</sub>(CO<sub>3</sub>)<sub>0.129</sub>·0.098(H<sub>2</sub>O) as determined by ICP-MS and TGA. LDH3 was fractionated to 6 different particle sizes using Fisher Scientific U.S. Standard test sieves, for which mesh sieve designations were 325, 230, 200, 170, 120, 80, and 70 (corresponding nominal sieve opening is 43, 63, 75, 90, 125, 180, and 212  $\mu$ m respectively). For each sieved LDH3 sample with a given particle size, diffusivity and adsorption isotherm experiments for CO<sub>2</sub> were conducted at 200°C with the same manner as described for LDH2 previously. The surface area of each sieved LDH3 was determined by a Micrometrics ASAP 2010 BET instrument based upon the BET method at liquid nitrogen temperature; the micropore volume of LDH3 was also determined by the same instrument using the Horvath-Kawazoe method.

### 6.3 Results and Discussion

- **Mathematical Model for Diffusivity Measurement...** To estimate the diffusion constant of CO<sub>2</sub> in LDH2, Crank's model for diffusion into a spherical particle was used[10]. According to this model, the governing equation for the concentration  $C$  of a species diffusing into a homogeneous spherical particle of radius  $r$  is given as:

$$\frac{\partial C}{\partial t} = D \left( \frac{\partial^2 C}{\partial r^2} + \frac{2}{r} \frac{\partial C}{\partial r} \right) \quad (1)$$

where  $D$  is the diffusivity constant.

From the solution of Eqn. (1), the uptake  $M_t$  at time  $t$  is given by:

$$\frac{M_t}{M_\infty} = 1 - \frac{6}{\mathbf{p}^2} \sum_{n=1}^{\infty} \frac{1}{n^2} \exp(-n^2 \cdot \mathbf{p}^2 \cdot \frac{D}{r^2} \cdot t) \quad (2)$$

where  $M_\infty$  is the uptake at large times (equilibrium).

For small times ( $M_t/M_\infty < 0.25$ ) Eqn. (2) is approximated as:

$$\frac{M_t}{M_\infty} = \frac{6D^{1/2}t^{1/2}}{\mathbf{p}^{1/2}r} \quad (3)$$

Therefore, if Eqn. (3) applies, the plot of  $M_t/M_\infty$  versus  $t^{1/2}$  should give a linear relationship, with a slope of  $6D^{1/2}/\mathbf{p}^{1/2}r$ . However, as shown in Figure 6.1a, Figure 6.2a, and Figure 6.3a, the results do not match linear plots. The short-time nonlinear behavior implies the existence of a crystalline structure in LDH2 particles. Actually, it was also reported by Ruthven that the linearity of  $M_t/M_\infty$  against  $t^{1/2}$  is destroyed for some crystalline materials, but the reasons were not provided[11].

Since nonlinear behavior in the short time region was not observed, the long time region was selected for the diffusivity constant calculations. For long times ( $M_t/M_\infty > 0.5$ ) the higher-order terms in Eqn. (2) become negligible so that the expression simplifies to:

$$\frac{M_t}{M_\infty} = 1 - \frac{6}{p^2} \exp(-p^2 D \cdot t / r^2) \quad (4)$$

Therefore, a plot of  $\ln(1 - M_t/M_\infty)$  versus  $t$  is linear with a slope of  $-p^2 D/r^2$  and intercept of  $\ln(6/p^2)$ . In this region, fairly good linearity is observed with the experimental data at all three temperatures as shown in Figures 4. 1b, 4.2b, and 4.3b.

Table 6.2 Diffusivity constants measured by experiment and calculated by molecular dynamic simulation.

Temperature, °C	by molecular dynamic simulation, cm <sup>2</sup> /s	by experiment, cm <sup>2</sup> /s
200	3.23 x 10 <sup>-7</sup>	3.61 x 10 <sup>-8</sup>
225	4.84 x 10 <sup>-7</sup>	8.90 x 10 <sup>-8</sup>
250	5.78 x 10 <sup>-7</sup>	1.33 x 10 <sup>-7</sup>

Table 6.3 Langmuir adsorption parameters of CO<sub>2</sub> in LDH2.

Temperature, °C	$m_{CO_2}$ , mmol/g sample	$b_{CO_2}$ , bar <sup>-1</sup>
200	0.27904	15.6125
225	0.26136	17.8243
250	0.24189	22.1608

- Diffusivities Determination...The diffusion constants for CO<sub>2</sub> in LDH were estimated from the slopes of the plots at long times at each elevated temperature, and the results were summarized in Table 6.2. According to Ruthven, the linearity in the long time region implies that the distribution of the crystal size of LDH is not significantly wide[11]. As a parallel study, diffusion coefficients were also calculated by molecular dynamic simulations at each temperature[12]; it can be observed that the resulting values from molecular dynamic simulation are in good qualitative agreement with experiments, as shown in Table 6.2. The temperature dependence of diffusivity constant for CO<sub>2</sub> is shown in Figure 6.4, and the activation energy of diffusion was calculated as 52.86 kJ/mol (12.64 kcal/mol) by the Arrhenius equation.

- Adsorption Isotherms...To analyze the adsorption isotherm data, firstly the experimental data were fitted with the Langmuir equation. The Langmuir theory is based on a kinetic principle, by which the rate of adsorption is equal to the rate of desorption from the surface [16]. The Langmuir model for CO<sub>2</sub> adsorption isotherm can be written as

$$q_{CO_2} = \frac{m_{CO_2} b_{CO_2} P_{CO_2}}{1 + b_{CO_2} P_{CO_2}}$$

where  $q_{CO_2}$  is the equilibrium concentration of adsorbed CO<sub>2</sub>,  $m_{CO_2}$  is the Langmuir model constant for CO<sub>2</sub>,  $b_{CO_2}$  is the Langmuir model constant for CO<sub>2</sub>, and  $P_{CO_2}$  is partial pressure of gas phase CO<sub>2</sub>. The experimental data and the fitted curves are shown in Figure 6.5, and the values of parameters in Langmuir model are summarized in Table 6.3. The Langmuir constant  $b_{CO_2}$  is also called the affinity constant since it represents how strong the molecule is adsorbed onto an adsorbent surface. And the temperature dependence of  $b_{CO_2}$  can be written as

$$b_{CO_2} = b_{\infty} \exp(Q / R_g T)$$

where  $Q$  is the heat of adsorption ( $-DH_{ad}$ ) and is same as the activation energy for desorption, and  $R_g$  is ideal gas constant (8.314 J/mole·K). The heat of adsorption ( $Q$ ) of LDH2 was estimated as -2.8739 kJ/mol from the slope of a linear plot of  $\ln b_{CO_2}$  versus  $1/T$ , of which the negative value means that the process is endothermic.

Normally, the affinity constant decreases with the temperature increase since the heat of adsorption is usually positive, which adsorption is an exothermic process. For the adsorption to occur the free energy must decrease and the entropy change is also negative since the degree of freedom decreases. Therefore, the enthalpy change must be negative, and it means the heat is released from the adsorption process. However, it was observed that the value of  $b_{CO_2}$  increased with temperature, and consequently the calculated value of the heat of adsorption is negative. It implies that the adsorption isotherm with LDH2 is chemisorption rather than physisorption, and to understand the adsorption isotherm of LDH2 better, the acquired data need to be analyzed with different models as well.

One of the earliest empirical equations used to describe isotherm is the Freundlich equation [17]. The equation for CO<sub>2</sub> adsorption may be the following form:

$$q_{CO_2} = KP^{1/n}$$

where  $q_{CO_2}$  is the concentration of the adsorbed CO<sub>2</sub>,  $K$  and  $n$  is the parameter of the Freundlich equation. The parameter  $K$  and  $n$  are generally temperature-dependent. To find the parameters of the Freundlich equation, the data are usually plotted in  $\log_{10}(q_{CO_2})$  versus  $\log_{10}(P)$ , which yields a straight line with a slope of  $(1/n)$  and as intercept of  $\log_{10}(K)$ .

$$\log_{10}(q_{CO_2}) = \log_{10}(K) + \frac{1}{n} \log_{10}(P)$$

Since the Freundlich equation does not have a Henry law behavior in the low pressure, and since it does not have a finite limit in high pressure, the Freundlich equation is only valid in a narrow range of adsorption data. The selection of data is also arbitrary, and here the first five data points were chosen at each temperature. The calculated parameter values of Freundlich equation were summarized in Table 6.4, and the experimental data with linear fitting were shown in Figure 6.6. From the fitting data shown in Figure 6.6, it was observed that the parameter  $K$  decreases with temperature, but the parameter  $n$  increases. Since the temperature dependence of parameters of  $K$  and  $n$  is complex, and also since it may be incorrect outside of the range of validity, the trend of parameter  $K$  and  $n$  of the Freundlich equation have to be regarded as specific case. For example, Rudzinski and Everett also reported that the  $1/n$  value is proportional to temperature with the system of CO adsorption on charcoal, but it was taken as a specific trend rather than general one [18].

Table 6.4 Values of parameters of the Freundlich equation for CO<sub>2</sub> adsorption in LDH2.

Temperature, °C	$K$	$n$
200	0.5573	1.8842
225	0.4990	2.0544
250	0.4084	2.5003

Table 6.5 The Langmuir-Freundlich equation parameters for CO<sub>2</sub> in LDH2.

Temperature, °C	$m_{CO_2}$ , mmol/g sample	$b_{CO_2}$ , bar <sup>-1</sup>	$n$
200	0.25677	16.8464	0.69837
225	0.24339	18.6860	0.72111
250	0.23116	22.3253	0.79789

Similar to the Langmuir equation (but with additional parameter  $n$ ) with a finite limit at sufficiently high pressures, Sips proposed the Langmuir-Freundlich equation<sup>19</sup> written as:

$$q_{CO_2} = m_{CO_2} \frac{(b_{CO_2} P)^{1/n}}{1 + (b_{CO_2} P)^{1/n}}$$

When the parameter of  $n$  is unity, the equation becomes the Langmuir model, which is applicable for ideal surfaces. Therefore, the parameter  $n$  is usually regarded as the parameter characterizing the system heterogeneity. The larger is the parameter of  $n$ ,

the higher is the degree of heterogeneity, but the source of heterogeneity is not provided with this parameter. The heterogeneity could be caused by the solid structural properties, the solid energetic properties, the sorbate properties, or the combination of these. The experimental data and fitted curves with the Langmuir-Freundlich equation are shown in Figure 6.7. And the values of the parameters in the Langmuir-Freundlich model are summarized in Table 6.5. From Table 6.5, it is observed that the value of parameter  $n$  increases with temperature, and hence the system becomes apparently more heterogeneous as temperature increases.

The temperature dependence of  $b_{CO_2}$  and exponent  $n$  may take the following form [17]:

$$b_{CO_2} = b_{\infty} \exp(Q/R_g T) = b_0 \exp\left[\frac{Q}{R_g T_0} \left(\frac{T_0}{T} - 1\right)\right]$$

$$\frac{1}{n} = \frac{1}{n_0} + \alpha \left(1 - \frac{T_0}{T}\right)$$

where  $b_{\infty}$  is the adsorption affinity constant at infinite temperature,  $b_0$  is the adsorption affinity at reference temperature  $T_0$ ,  $n_0$  is the parameter  $n$  at the same temperature and  $\alpha$  is a constant parameter. In the Langmuir equation  $Q$  is the heat of adsorption and is not changed by the surface loading. However, in the Langmuir-Freundlich equation, the parameter  $Q$  is only a measure of the adsorption heat. Only when the fractional loading is equal to one half,  $Q$  is equal to the isosteric heat. Therefore, the parameter  $Q$  in Langmuir-Freundlich equation means the isosteric heat at the fractional loading of 0.5.

Though Langmuir-Freundlich equation provides some sense of the system heterogeneity, it does not possess the correct Henry law behavior. The Freundlich equation is not valid at high and low end of the pressure range. To satisfy the both end limits, Toth proposed the empirical adsorption isotherm equation, and the Toth equation describes well the system with sub-monolayer coverage [20, 21]. The Toth equation for the  $CO_2$  adsorption may be written as:

$$q_{CO_2} = m_{CO_2} \frac{bP}{[1 + (bP)^t]^{1/t}}$$

where  $t$  is a parameter, which  $t$  and  $b$  are specific for adsorbate-adsorbent pairs. When  $t$  is equal to 1, the Toth isotherm equation reduces to the Langmuir equation. Therefore, like the Langmuir-Freundlich equation, the parameter  $t$  can be regarded as the measure of the system heterogeneity. The experimental data and fitted curves are shown in Figure 6.8, and the values of the parameters in the Toth model are summarized in Table 6.6. It is observed that the values of the parameter  $t$  are greater than unity, which indicates a strong degree of heterogeneity of the system.

Table 6.6 The Toth equation parameters for CO<sub>2</sub> in LDH2.

Temperature, °C	$m_{CO_2}$ , mmol/g sample	$b_{CO_2}$ , bar <sup>-1</sup>	$t$
200	0.25218	10.19558	1.80226
225	0.24019	11.86695	1.64989
250	0.22934	15.97911	1.38246

Table 6.7 The exponential equation parameters for CO<sub>2</sub> in LDH2.

Temperature, °C	$q_{CO_2}$ , mmol/g	$b$ , bar <sup>-1</sup>
200	0.2455	11.9684
225	0.2318	13.2177
250	0.2175	15.8356

Although it is not widely used as other empirical equations, the exponential equation is also a useful empirical equation. The exponential equation for the CO<sub>2</sub> adsorption isotherm can be written as

$$q_{CO_2} = q_s(1 - e^{-bt})$$

$$b = b_\infty \exp(Q/R_g T)$$

where  $q_{CO_2}$  is equilibrium concentration of adsorbed CO<sub>2</sub>,  $q_s$  is saturation concentration, and  $b_\infty$  is the affinity at infinite temperature. At low pressure the exponential equation reduces to Henry's law, and at high pressure the equation reaches the saturation limit. The experimental data and nonlinear fitting curves are shown in Figure 6.9, and the values of parameters in the exponential model are summarized in Table 6.7. It is observed that  $q_{CO_2}$  is decreased as temperature increases, but  $b$  is increased as temperature increases like previous models.

For the empirical equations described, so far, the adsorption mechanism is assumed to be surface layering (formation of successive layers). However, for microporous solids, another important adsorption mechanism is pore filling, which was originally developed by Dubinin [22-25]. Also, according to the suggestion of Bering *et al.* [27, 28], the adsorption in pores less than 15Å should follow the pore filling mechanism rather than surface coverage. For the description of adsorption isotherm in microporous solids with pore filling mechanism, a widely used semi-empirical equation is the Dubinin-Radushkevich (DR) equation, which may be written as:



$$C = C_s \exp \left[ -\frac{1}{E^2} (R_g T \ln \frac{P}{P_0})^2 \right]$$

where  $C$  is the amount adsorbed,  $C_s$  is maximum adsorption capacity,  $E$  is characteristic energy,  $R_g$  is ideal gas constant. The increase of characteristic energy means the adsorption is stronger since the solid has stronger energy of interaction with adsorbate. To find the values of characteristic energy  $E$ , the adsorption data of different temperatures were plotted as the logarithm of the fractional loading versus the square of logarithm of reduced pressure. From the slopes of the linear fit, the values of  $E$  were calculated. The experimental data and linear fit are shown in Figure 6.10, and the summary of results is shown in Table 6.8. It is observed that the characteristic energy increased as the temperature increased, and, therefore, it implies that the interaction between LDH and  $\text{CO}_2$  also increases as temperature increases.

Table 6.8 The characteristic energies for  $\text{CO}_2$  in LDH2 with DR equation.

Temperature, °C	$E$ , kJ/mol
200	12.350
225	13.677
250	15.782

Table 6.9 The uptake amount and BET surface area of LDH3 particles.

Particle radius [ $\mu\text{m}$ ]	Uptake [mmol/g]	BET surface area [ $\text{m}^2/\text{g}$ ]	Normalized uptake [mmol/ $\text{m}^2$ ]
26.5	0.64545	36.2732	0.01779
34.5	0.57727	32.9144	0.01754
43.75	0.53500	30.8792	0.01733
53.75	0.49318	30.0916	0.01639
76.25	0.45227	25.4140	0.01780
98.75	0.43636	21.8627	0.01996

- Effect of Particle Size...It was observed that at the temperature of 200°C the uptake amount of CO<sub>2</sub> in LDH3 decreases as the particle radius increases (Figure 6.11), and it may be explained with surface area of LDH3 particles as shown in Table 6.9. According to Table 6.9, it is evident that the surface area of LDH3 particle decreases when the particle radius increases. And, when the uptake amount was normalized with corresponding surface area, it is found that the uptake amount is fairly constant all over the range of particle size.

Table 6.10 The Langmuir adsorption parameters of CO<sub>2</sub> in LDH3 at 200°C with different particle size.

Particle radius, μm	$m_{CO_2}$ , mmol/g sample	$b_{CO_2}$ , bar <sup>-1</sup>
26.5	0.75129	10.5694
34.5	0.65995	11.6985
43.75	0.56710	10.6203
53.75	0.52253	11.0997
76.25	0.51523	13.2044
98.75	0.43705	13.6583

The experimental data and the fitted curves with the Langmuir equation are shown in Figure 6.12, and the values of parameters are summarized in Table 6.10. According to Table 6.10 and Figure 6.12(b), it is evident that Langmuir parameter  $b_{CO_2}$  is relatively constant over the range of particle sizes. The  $b_{CO_2}$  value obtained here is close to the one obtained from Langmuir equation with LDH2 at 200°C in Table 6.5. The experimental data were also studied with Langmuir-Freundlich equation since

Table 6.11 The Langmuir-Freundlich equation parameters of CO<sub>2</sub> in LDH3 at 200°C with different particle size.

Particle radius, μm	$m_{CO_2}$ , mmol/g sample	$b_{CO_2}$ , bar <sup>-1</sup>	$n$
26.5	0.68824	12.33558	0.76988
34.5	0.6578	11.77357	0.79127
43.75	0.53429	11.85758	0.74523
53.75	0.48755	12.55263	0.71473
76.25	0.47115	12.96453	0.72593
98.75	0.41754	13.05532	0.74152

Langmuir-Freundlich equation provides more information and since the experimental data were better fitted with this equation than others. The nonlinear fitting curves are shown in Figure 6.15, and the values of parameters are summarized in Table 6.11. It was observed that the parameter values of  $b_{CO_2}$  and  $n$  are not changing significantly,

and hence it implies that the interaction between CO<sub>2</sub> and LDH3 does not change significantly with particle size, and that the heterogeneity of system is not changing, either.

## 6.4 Conclusions

Based upon the rate and equilibrium capacity measurement for the LDH materials, key conclusions are drawn here:

- Diffusivity constants and adsorption isotherms for carbon dioxide in Mg-Al-CO<sub>3</sub> LDH2 at 200 - 250°C were determined by the gravimetric method. Diffusivity constants determined by experiments and those obtained by molecular dynamic simulations are in good qualitative agreement.
- The experimental adsorption isotherms for CO<sub>2</sub> in LDH2 have been studied with the Langmuir isotherm equation and various empirical adsorption isotherm equations. It was observed that the heterogeneity of the material and the interaction between CO<sub>2</sub> and LDH2 increases with temperature. Also it was found that the experimental data were nonlinearly fitted best with the Toth equation based on  $\chi^2$  values.
- For the study of particle size effect on CO<sub>2</sub> uptake and adsorption isotherm experiments, it was observed that the amount of CO<sub>2</sub> uptake, and the BET surface area increased as the particle size decreased. When the uptake amount was normalized with BET surface area, it was found that the uptake amount was fairly constant for all the ranges of particle sizes. The adsorption isotherm data with different particle sizes of LDH3 were studied with Langmuir isotherm and Langmuir-Freundlich equation. It was observed that the values of  $b_{CO_2}$  and  $n$  were relatively constant for the whole range of particle sizes.

The parameters and the best fitted equation obtained in this chapter were used for simulating the CO<sub>2</sub> removal via an LDH adsorbents in an innovative membrane reactor as presented in Chapter 7.

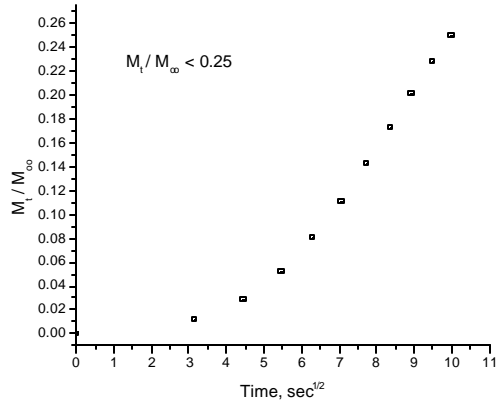
## Literature Cited

1. Callaghan, P. T. *Principles of NMR Microscopy*, Clarendon Press, Oxford, 1991.
2. Badruzzaman, M; Westerhoff, P; Knappe, D. R. U. Intraparticle diffusion and adsorption of arsenate onto granular ferric hydroxide., *Water Research*, **2004**, *38*, 4002-4012.
3. Grande, C. A.; Basaldella, E.; Rodrigues, A. E. Crystal size effect in vacuum pressure-swing adsorption for propane/propylene separation., *Ind. Eng. Chem. Res.*, **2004**, *43*, 7557-7565.
4. Miyata, S. The syntheses of hydrotalcite-like compounds and their structures and physico-chemical properties I. The systems magnesium(2+)-aluminum(3+)-

- nitrate(1-), -chloride(1-) and -perchlorate(1-), nickel(2+)-aluminum(3+)-chloride(1-), and zinc(2+)-aluminum(3+)-chloride(1-). *Clays and Clay Minerals*, **1975**, 23, 369.
5. Prinetto, F.; Ghiotti, G.; Graffin, P.; Tichit, D. Synthesis and characterization of sol-gel Mg/Al and Ni/Al layered double hydroxides and comparison with co-precipitated samples. *Microporous and Mesoporous Materials*, **2000**, 39, 229-247.
  6. Chagger, H. K.; Ndaji, F. E.; Sykes, M. L.; Thomas, K. M. Kinetics of adsorption and diffusional characteristics of carbon molecular sieves, *Carbon*, **1995**, 33, 1405.
  7. Kapoor, A.; Yang, T. Kinetic separation of methane-carbon dioxide mixture by adsorption on molecular sieve carbon, *Chem. Eng. Sci.*, **1989**, 44, 1723.
  8. Yang, R. T.; Baksh, M. S. A. Pillared clays as a new class of sorbents for gas separation, *AIChE J.*, **1991**, 37, 679.
  9. Yucel, H.; Ruthven, D. M. Diffusion of Carbon dioxide in 4A and 5A zeolite crystals, *J. Colloid Interface Sci.*, **1980**, 74, 186.
  10. Crank, J. *The Mathematics of Diffusion*, 2<sup>nd</sup> Edition, Clarendon Press, Oxford, 1975.
  11. Ruthven, D. M., in *Adsorption, Science and Technology* (Edited by Rodriguez, A. E.), Kluwer Academic Publishers, Netherlands, 87-114, 1989.
  12. Kim, N.; Kim, Y.; Tsotsis, T. T.; Sahimi, M., Molecular modeling of the thermal evolution of the structure of Mg-Al-CO<sub>3</sub> layered double hydroxide., presented at AIChE's Annual Meeting, November 16-21, San Francisco, CA, 2003.
  13. Kärger, J.; Pfeifer, H.; Heink, W. Principles and application of self-diffusion measurement by nuclear magnetic resonance, *Adv. Mag. Res.* **1988**, 12, 1.
  14. Abragam, A. Principles of Nuclear Magnetism, Oxford University Press, New York, 1961.
  15. Stejskal, E. O.; Tanner, J. E. Spin diffusion measurement: spin echoes in the presence of a time-dependent field gradient. *J. Chem. Phys.* **1965**, 42(1), 288.
  16. Langmuir, I. The adsorption of gases on plane surface of glass, mica, and platinum, *J. Ame. Chem. Soc.*, **1918**, 40, 1361.
  17. Freundlich, H. Kinetics and energetics of gas separation, *Trans. Farad. Soc.*, **1932**, 28, 195.
  18. Rudzinski, W.; Everett, D. H., *Adsorption of Gases on Heterogeneous Surfaces*, Academic Press, San Diego, 1992.
  19. Sips, R. Structure of catalyst surface, *J. Chem. Phys.*, **1948**, 16, 490.
  20. Do, D. D. *Adsorption Analysis: Equilibria and Kinetics*, Series on Chemical Engineering Vol. 2, Imperial College Press, London, 1988.
  21. Toth, J. Uniform interpretation of gas/solid adsorption, *Adv. Colloid Interface Sci.*, **1995**, 55, 1.
  22. Toth, J. *Adsorption. Theory, Modeling, and Analysis*, Dekker, New York, 2002.
  23. Dubinin, M. M., Porous structure and adsorption properties of active carbon, *Chemistry and Physics of Carbon*, **1966**, 2, 51.
  24. Dubinin, M. M., Adsorption in micropores, *J. Colloid Interface Sci.*, **1967**, 23, 487.

25. Dubinin, M. M., Fundamentals of the theory of physical adsorption of gases and vapors in micropores, *Adsorption – desorption Phenomena, Proc. Int. Conf.*, **1972**, 2nd, 3.
26. Dubinin, M. M., Physical adsorption of gases and vapors in micropores, *Progress in Surface and Membrane Science*, **1975**, 9, 1.
27. Bering, B. P.; Dubinin, M. M.; Serpinsky, V. V., Theory of volume filling for vapor adsorption, *J. Colloid Interface Sci.* **1966**, 21, 378.
28. Bering, B. P.; Dubinin, M. M.; Serpinsky, V. V., Thermodynamics in micropores, *J. Colloid Interface Sci.* **1972**, 38, 185.
29. Ruckenstein, E.; Vaidyanathan, A. S.; Youngquist, G. R., Sorption by solids with bidisperse pore structures, *Chem. Eng. Sci.* **1971**, 26, 1305.

(a)



(b)

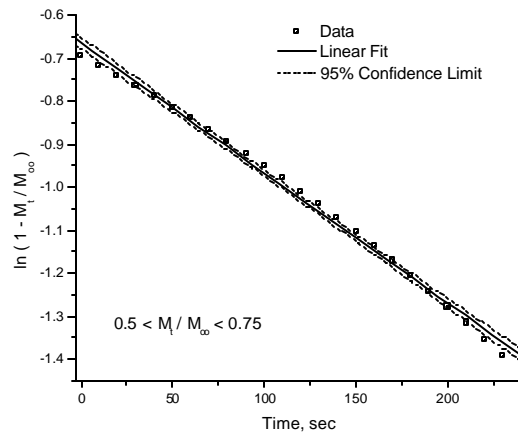
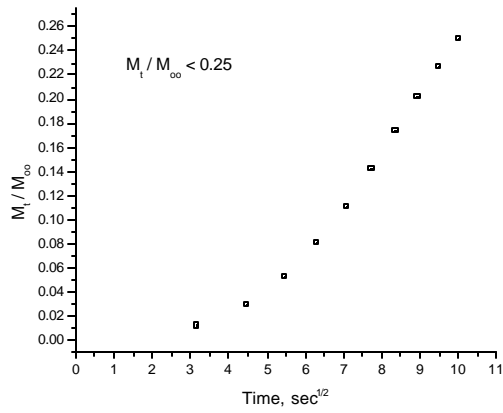


Figure 6.1 A graph of (a)  $M_t/M_\infty$  against  $t^{1/2}$ , and (b)  $\ln(1 - M_t/M_\infty)$  against  $t$  for the uptake of carbon dioxide at 200 °C.

(a)



(b)

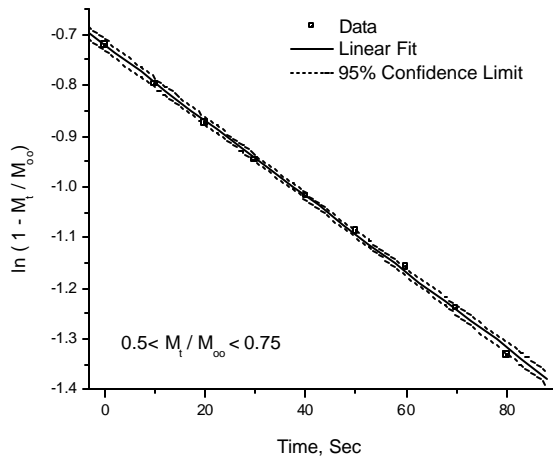
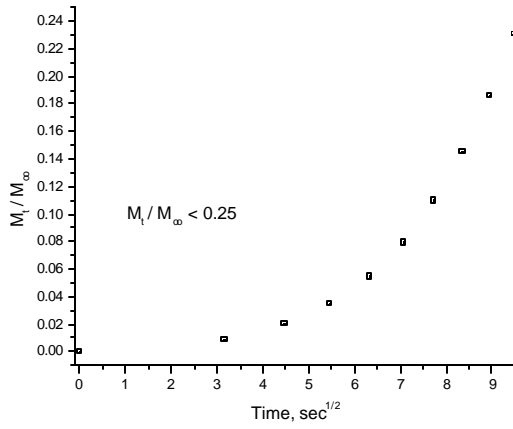


Figure 6.2 A graph of (a)  $M_t/M_\infty$  against  $t^{1/2}$ , and (b)  $\ln(1 - M_t/M_\infty)$  against  $t$  for the uptake of carbon dioxide at 225 °C.

(a)



(b)

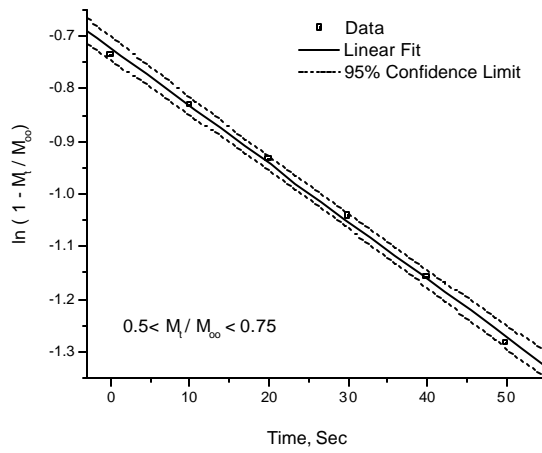


Figure 6.3 A graph of (a)  $M_t/M_\infty$  against  $t^{1/2}$ , and (b)  $\ln(1 - M_t/M_\infty)$  against  $t$  for the uptake of carbon dioxide at 250 °C.



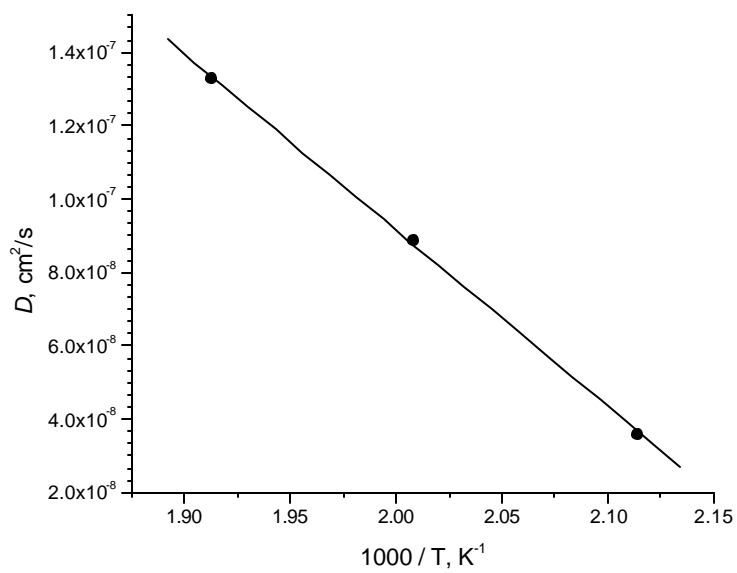


Figure 6.4 Temperature dependence of diffusion coefficient for CO<sub>2</sub> in LDH2.

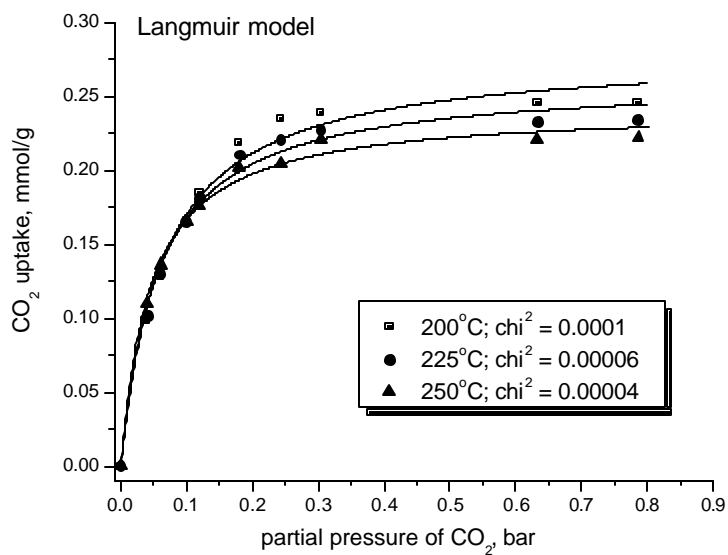


Figure 6.5 The experimental data and nonlinear curve fitting with the Langmuir equation for adsorption isotherm of CO<sub>2</sub> in LDH2.

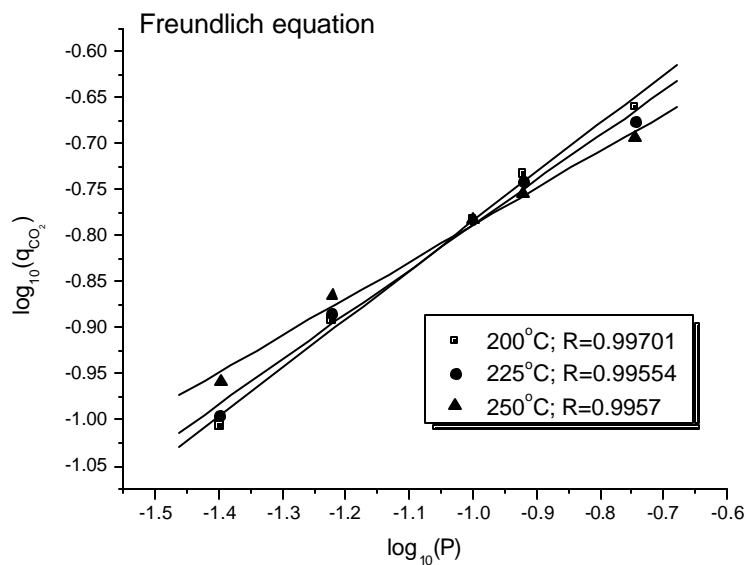


Figure 6.6 The experimental data and the fitting with the linearized Freundlich equation for adsorption isotherm of CO<sub>2</sub> in LDH2.

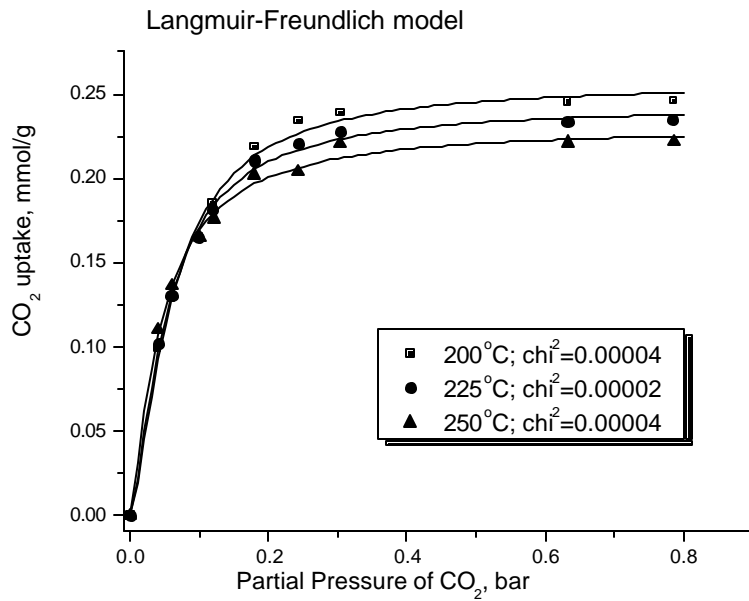


Figure 6.7 The experimental data and nonlinear curve fitting with the Langmuir-Freundlich equation for adsorption isotherm of CO<sub>2</sub> in LDH2.

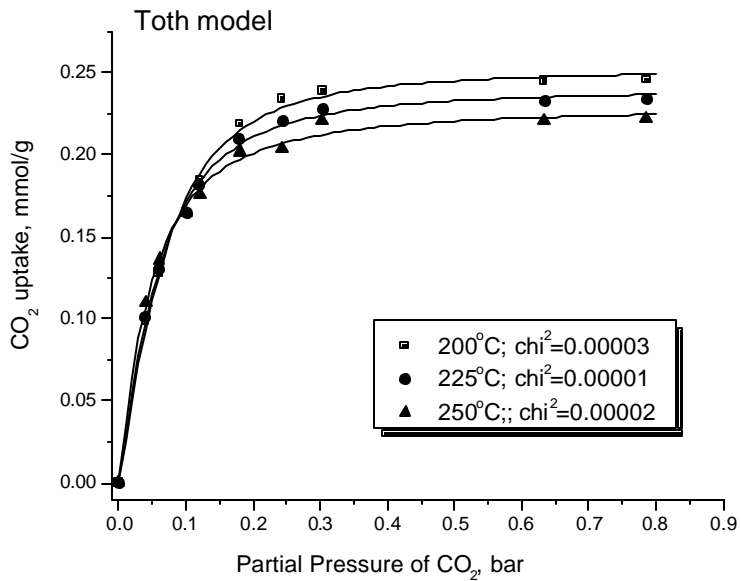


Figure 6.8 The experimental data and nonlinear curve fitting with the Toth equation for adsorption isotherm of CO<sub>2</sub> in LDH2.

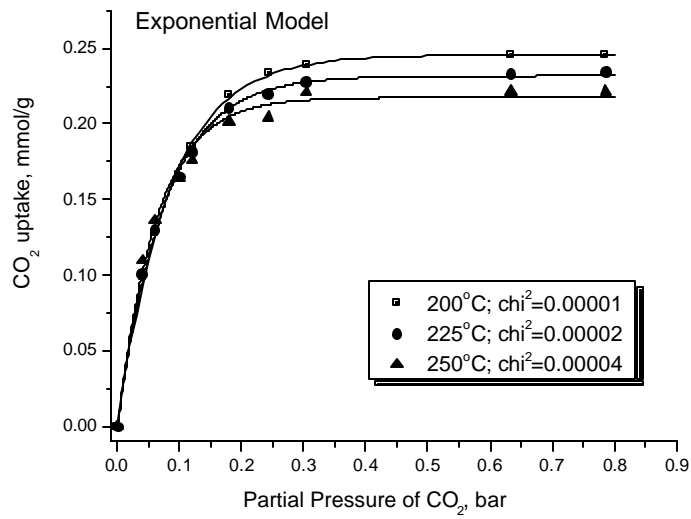


Figure 6.9 The experimental data and nonlinear curve fitting with exponential equation for adsorption isotherm of CO<sub>2</sub> in LDH2.

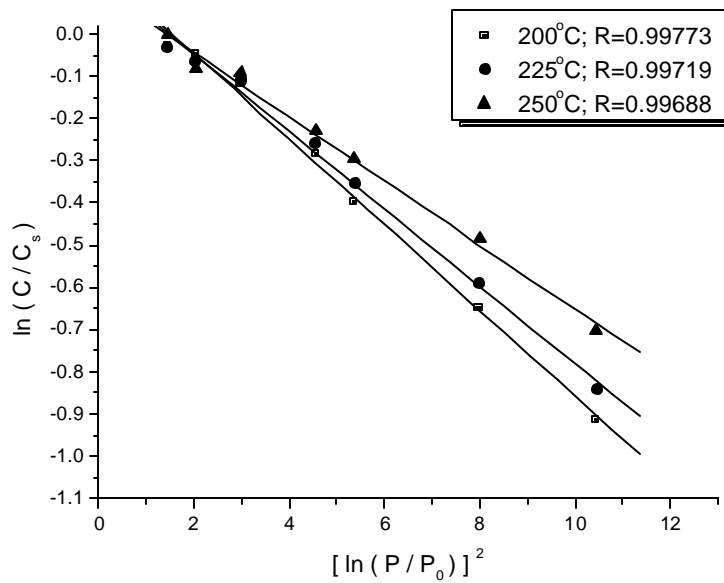


Figure 6.10 The experimental data and linear fitting with linearized DR equation for adsorption isotherm of CO<sub>2</sub> in LDH2.

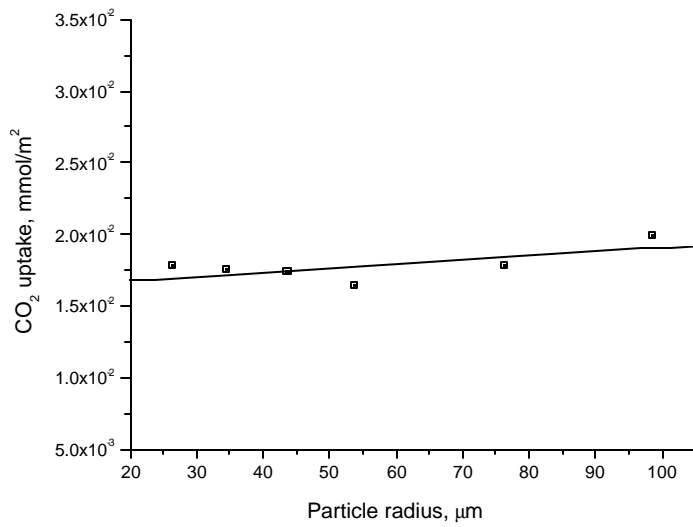
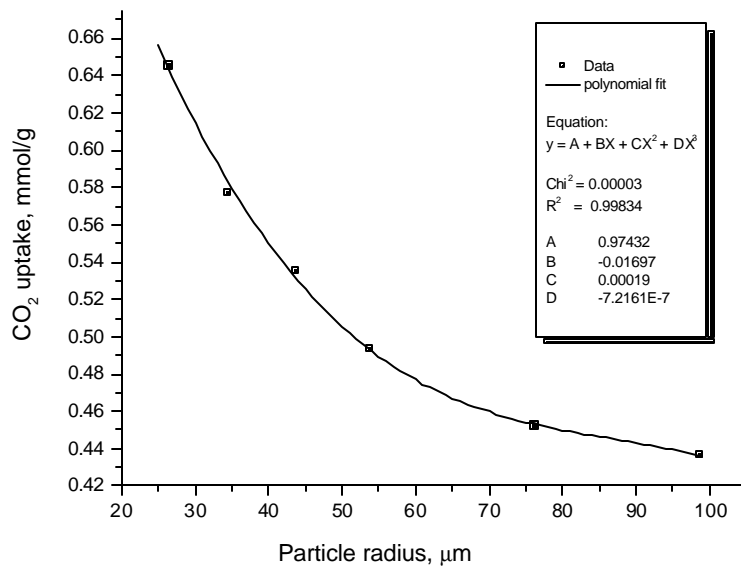


Figure 6.11 The uptake amount of CO<sub>2</sub> with different LDH3 particle sizes at 200°C

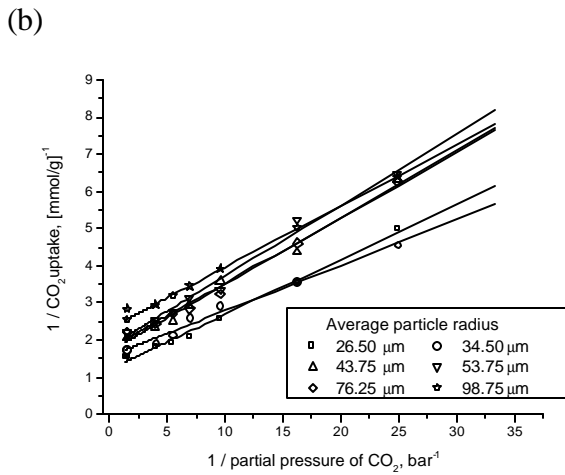
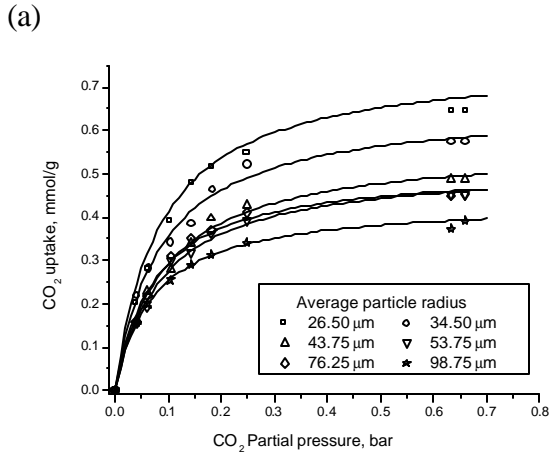
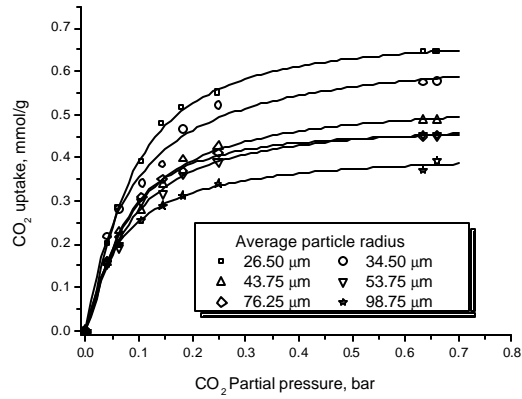


Figure 6.12 (a) The experimental data and nonlinear curve fitting with the Langmuir equation, and (b) the experimental data and linearized Langmuir equation for adsorption isotherm of  $\text{CO}_2$  in LDH3.

(a)



(b)

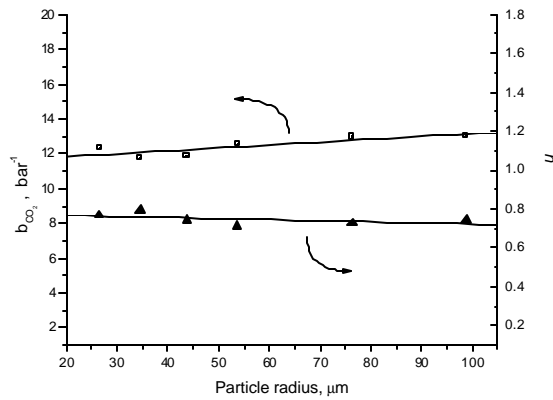


Figure 6.13 (a) The experimental data and nonlinear curve fitting with the Langmuir-Freundlich equation, and (b) the parameter values of Langmuir-Freundlich equation for adsorption isotherm of CO<sub>2</sub> in LDH3.

## Chapter 7

### Mathematical Simulation and Experimental Verification of Hydrogen Production with Concomitant CO<sub>2</sub> Recovery

#### 7.1 Introduction/Literature Review

Reactive separation processes have been attracting renewed interest for application in catalytic steam reforming and the water gas shift reaction. From the standpoint of hydrogen production with concomitant removal of CO<sub>2</sub>, reactive separation could offer a unique opportunity to reduce the hydrogen production cost via the separation of CO<sub>2</sub> from the reactor, making CO<sub>2</sub> ready for sequestration. Commonly discussed reactive separation processes include packed-bed catalytic membrane reactors (MR) [10-15] and, more recently, adsorptive reactor (AR) processes [16-26]. Their potential advantages over the more conventional reactors have been widely discussed. They include (i) increasing the reactant conversion and product yield through shifting the equilibrium towards the products, potentially allowing one to operate under milder operating conditions (e.g., lower temperatures, pressures and/or reduced steam consumption), and (ii) reducing the downstream purification requirements by in situ separating from the reaction mixture the desired product hydrogen (in the case of MR) or the undesired product CO<sub>2</sub> (in the case of AR). MR shows substantial promise in this area and, typically, utilizes nanoporous inorganic or metallic Pd or Pd-alloy membranes [15]. The latter are better suited for pure hydrogen production. However, metallic membranes are very expensive and become brittle during reactor operation [13] or deactivate in the presence of sulfur or coke. Nanoporous membranes are better suited for the steam-reforming environment. They are difficult to manufacture, however, without cracks and pinholes and, as a result, often have inferior product yield. In addition, the hydrogen in the permeate side contains other byproducts, and may require further treatment for use in fuel-cell-powered vehicles.

Adsorptive reactors also show good potential [16-20] for methane-steam-reforming and water gas shift. The challenge here, however, is in matching the adsorbent properties with those of the catalytic system. Two types of adsorbents have been suggested: potassium-promoted layered-double hydroxides (LDHs), which operate stably only at lower temperatures (less than 500°C [25-27]), and CaO or commercial dolomite, which can be utilized at the typical steam-reforming temperatures of 650-700°C [21] but requires temperatures higher than 850°C for regeneration [23,24]. These are very harsh conditions that result in gradual deterioration of the adsorbent properties and potentially sintering of the reforming catalyst [23,24]. The mismatch between the reaction and regeneration conditions is likely to result in significant process complications.

Here, what we propose for use is a novel reactor system, termed the hybrid adsorbent-membrane reactor (HAMR). The HAMR concept [1,2,28] couples the reaction and membrane separation steps with adsorption, which takes place in the reactor and/or membrane permeate side. The HAMR system investigated previously involved a hybrid pervaporation MR system and integrated the reaction and pervaporation steps through a



membrane with water adsorption. Coupling reaction, pervaporation, and adsorption demonstrated significant improvement in performance. Most recently, Elnashaie and co-workers [29-32] mathematically analyzed the behavior of a circulating fluidized-bed HAMR system utilizing Pd membranes. This reactor is assumed to operate at steady state by recirculating the catalyst and adsorbent through a second reactor for regeneration. The ability of Pd membranes to withstand the rigors of the fluidized-bed steam-reforming environment and of the adsorbents to undergo continuous recirculation and regeneration still remains the key challenge.

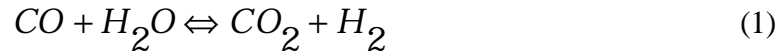
The HAMR configuration can be potentially used with equilibrium- or selectivity-limited reactions in which one of the products can be adsorbed while another (or the same) product can be simultaneously removed via a membrane. What limits the application of the concept is the availability of stable efficient adsorbents under reaction conditions. Esterification reactions (like the ethanol reaction with acetic acid to produce ethyl acetate previously studied by our group [1,2], through the use of water adsorbents), and the production of hydrogen (through steam reforming or the water gas shift reactions) are two key potential applications. Here, we investigate a HAMR system involving a hybrid packed-bed catalytic MR, coupling the water gas shift reaction through a porous inorganic H<sub>2</sub>-selective membrane with a CO<sub>2</sub> adsorption system. This HAMR system exhibits behavior that is more advantageous than either the MR or AR, in terms of the attained yields and selectivities. In addition, the HAMR system potentially allows for significantly greater process flexibility than either the MR or AR system. The membrane, for example, can potentially be used to separate the catalyst from the adsorbent phase, thus allowing for in situ continuous regeneration of the adsorbent. This offers a significant advantage over the ARs, which require the presence of multiple beds (one being in operation while the other is being regenerated) to achieve continuous operation. The HAMR system shows, furthermore, significant potential advantages with respect to the conventional MR system. Beyond the improved yields and selectivities, the HAMR system has the potential for producing a CO-free fuel-cell-grade hydrogen product, which is of significance for the proposed fuel-cell-based mobile applications of such systems.

In this chapter, a mathematical model for the HAMR system is presented and analyzed for a range of temperature and pressure conditions. Through numerical simulation, the behavior of the HAMR system is compared with the conventional packed-bed reactor, as well as a MR and an AR system. In addition, experimental data for the HAMR based on the hydrotalcite type adsorbent and the nanoporous H<sub>2</sub> selective membrane are presented for comparison with the mathematical simulation results.

## **7.2 Fundamentals**

### **7.2.1 Kinetics for Water Gas Shift Reaction.**

For the water gas shift reaction, we utilize an empirical power law-type reaction rate expression. Formation rates for the H<sub>2</sub>, and CO<sub>2</sub> products and the disappearance rates for CO and H<sub>2</sub>O are given by the following equations:



$$r = k \frac{P_{CO} * P_{H_2O}^{1.4}}{P_{H_2}^{0.9} P_{CO_2}^{0.7}} (1 - \mathbf{b}) \frac{1}{Pt^{0.4}} \quad (2)$$

$$\mathbf{b} = \frac{P_{CO_2} * P_{H_2}}{Ke * P_{H_2O} P_{CO}} \quad (3)$$

$$k = k_0 * \exp(-114218.6 / (R + (T + 273))) \quad (4)$$

### 7.2.2 Mathematical Model of the HAMR System.

A schematic of the HAMR system is shown in Figure 7.1. In this figure, the catalyst and adsorbent are packed in the exterior of the membrane (signified by the superscript F, or the feed side), with additional adsorbent also packed in the interior of the membrane volume (signified by the superscript P, or the permeate side). There are, of course, a number of other potential reactor configurations, as previously noted. For example, the catalyst may be loaded in the feed side, while the adsorbent may also be loaded in the permeate side, or the catalyst and adsorbent may only be loaded in the feed side, with no adsorbent or catalyst being present in the permeate side, which is the configuration that is analyzed here. To simplify matters, in the development of the model, we assume that the reactor operates isothermally, that external mass-transfer resistances are negligible for the transport through the membrane as well as for the catalysts, and that internal diffusion limitations for the catalyst, and internal or external transport limitations for the adsorbent, are accounted for by the overall rate coefficients. Moreover, plug-flow conditions are assumed to prevail for both the interior and exterior membrane volumes, as well as ideal gas law conditions.

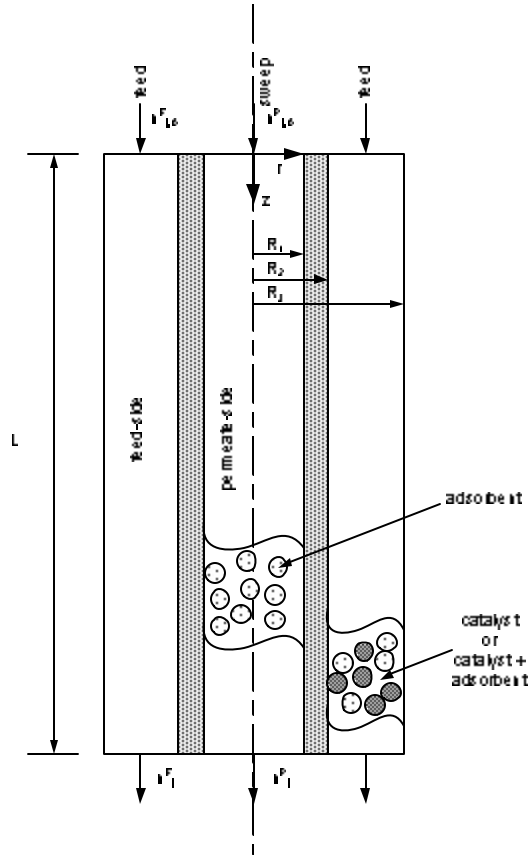


Figure 7.1 Schematic diagram of a HAMR system.

Mass transfer through the porous membrane is described by the following empirical equation:

$$F_j = U_j (P_j^F - P_j^P) \quad (5)$$

where  $F_j$  is the molar flux ( $\text{mol}/\text{m}^2 \cdot \text{s}$ ),  $P_j^F$  the partial pressure of component  $j$  on the membrane feed side (bar),  $P_j^P$  the partial pressure of component  $j$  on the membrane permeate side (bar), and  $U_j$  the membrane permeance for component  $j$  ( $\text{mol}/\text{m}^2 \cdot \text{bar} \cdot \text{s}$ ). Equation 5 is, of course, a simplified empirical expression for describing flux through a nanoporous membrane for which the size of the pores approaches that of the diffusing molecules. Substantial efforts are currently ongoing by our group and others for a better understanding of the phenomena that occur during molecular transport through such nanoporous systems. Simple analytical expressions for describing transport through such membranes are currently lacking, however, thus the choice of the commonly utilized empirical Equation 5 in this preliminary reactor modeling investigation.

The mass balance on the feed side of the reactor packed with water gas shift reaction catalyst and, potentially, an adsorbent is described by the following equations for  $\text{CO}_2$ ,  $\text{CO}$ ,  $\text{H}_2$ ,  $\text{H}_2\text{O}$  and an inert species (potentially used as a sweep gas or a blanketing agent);

for catalytic water gas shift reaction, a practical sweep gas would be either steam or hydrogen, however):

$$\mathbf{e}^F \frac{\partial C_j^F}{\partial t} + \frac{\partial n_j^F}{\partial V} = -\mathbf{a}_m U_j (P_j^F - P_j^P) + (1 - \mathbf{e}_b^F) \mathbf{b}_c \mathbf{r}_c R_j^F - (1 - \mathbf{e}_b^F)(1 - \mathbf{b}_c) \mathbf{r}_a G_j^F + \mathbf{e}_b^F (A^F)^2 \frac{\partial}{\partial V} \left( D_L^F \frac{\partial C_j^F}{\partial V} \right) \quad (6)$$

In Equation 6,  $n_j^F$  is the molar flow rate (mol/s) for species  $j$  and  $C_j^F$  is the gas-phase concentration (kmol/m<sup>3</sup>) equal to  $n_j^F / Q^F$ , where  $Q^F$  is the volumetric flow rate (m<sup>3</sup>/s).  $V$  is the feed-side reactor volume variable (m<sup>3</sup>),  $A^F$  the cross-sectional area for the reactor feed side (m<sup>2</sup>),  $\mathbf{a}_m$  the membrane area per feed-side reactor volume (m<sup>2</sup>/m<sup>3</sup>),  $\mathbf{e}_b^F$  the bed porosity on the feed side,  $\mathbf{e}^F$  the total feed-side bed porosity (it includes the bed porosity and catalyst porosity),  $\mathbf{b}_c$  the fraction of the solid volume occupied by catalysts ( $\mathbf{b}_c = 1$  when no adsorbent is present),  $\rho_c$  the catalyst density (kg/m<sup>3</sup>),  $\rho_a$  the adsorbent density (kg/m<sup>3</sup>), and  $R_j^F$  the reaction rate expression. Assuming that the adsorbent only adsorbs CO<sub>2</sub>,  $G_j^F$  is zero for all other components except CO<sub>2</sub>.  $D_L^F$  (m<sup>2</sup>/s) is the axial dispersion coefficient given by the following equation[34] generally applicable for describing dispersion phenomena through packed beds:

$$D_L^F = 0.73 D_m^F + \frac{0.5 u^F d_p^F}{1 + 9.49 (D_m^F / u^F d_p^F)} \quad (7)$$

where  $D_m^F$  is molecular diffusivity (m<sup>2</sup>/s),  $u^F$  is the velocity at the feed side (m/s), and  $d_p^F$  is the particle diameter in the feed side (m). One finds a number of approaches in the literature for describing  $G_{CO_2}^F$ . Ideally, one would like to account explicitly for both external and internal mass transport and finite rates of adsorption. Such an approach goes beyond the scope of this preliminary investigation, however, in addition to the fact that there are currently no experimental high-temperature transport/adsorption CO<sub>2</sub> data to justify this level of mathematical detail. Traditionally, in the modeling of ARs, simpler models have been utilized instead [22,27]. Two such models have received the most attention. They are (i) the model based on the assumption of instantaneous local adsorption equilibrium between the gas and adsorbent phases [2, 22, 27, 28] and (ii) the linear driving force (LDF) models, according to which  $G_{CO_2}^F$  is described by the following expression[35]:

$$\frac{dC_s}{dt} = G_{CO_2}^F = k_a (C_{seq} - C_s) \quad (8)$$

where  $C_{seq}$  is the adsorption equilibrium CO<sub>2</sub> concentration on the adsorbent (mol/kg) corresponding to the prevailing gas-phase concentration,  $C_s$  is the existing adsorbed CO<sub>2</sub> concentration (mol/kg), and  $k_a$  (s<sup>-1</sup>) is a parameter that "lumps" together the effects of external and intraparticle mass transport and the sorption processes and that, as a result, is often a strong function of temperature and pressure[27], although, typically, in modeling it is taken as temperature/pressure-independent. To calculate  $C_{seq}$ , we utilize the data reported by Ding and Alpay [22,27] for CO<sub>2</sub> adsorption on potassium-promoted LDH. They showed that the CO<sub>2</sub> adsorption on this adsorbent follows a Langmuir adsorption isotherm under both dry and wet conditions, described by the following equation:

$$C_{seq} = \frac{m_{CO_2} b_{CO_2} P_{CO_2}}{1 + b_{CO_2} P_{CO_2}} \quad (9)$$

where  $m_{CO_2}$  (mol/kg) is the total adsorbent capacity and  $b_{CO_2}$  (bar<sup>-1</sup>) the adsorption equilibrium constant, which is described by the van't Hoff equation:

$$b_{CO_2} = b_{CO_2}(T_0) \exp[-\Delta H_a / R(1/T - 1/T_0)] \quad (10)$$

The heat of adsorption,  $\Delta H_a$  (kJ/mol), under wet conditions for a region of temperatures from 481 to 753 K was calculated to be -17 kJ/mol, while  $b_{CO_2}$  at 673 K is equal to 23.6 bar[27]. Equations 6 and 8 must be complemented by initial and boundary conditions. For simplicity, we assume here that the reactor, prior to the initiation of the reaction/adsorption step, has undergone a start-up procedure as described by Ding and Alpay [22] that involves (i) heating the reactor to the desired temperature under atmospheric pressures by feeding H<sub>2</sub> on the reactor feed side and the chosen sweep gas on the permeate side, (ii) supplying water to the system so that the feed H<sub>2</sub>O/H<sub>2</sub> ratio is the same as the H<sub>2</sub>O/CO ratio to be used during the reaction step, (iii) pressurizing the feed and permeate sides to the desired pressure conditions, and (iv) switching from H<sub>2</sub> to CO to initiate the reaction/adsorption step. In the simulations, the conditions prevailing at the start of step (iv) are those prevailing at steady state during step (iii). In addition, during step (iv) the following conventional boundary conditions prevail [16-20]:

$$\text{at } V = 0; \quad \frac{dx_j^F}{dV} = -\frac{u_0^F (x_{j_0}^F - x_j^F)}{A^F \mathbf{e}_b^F D_L^F} \quad (11)$$

$$\text{at } V = V_R; \quad \frac{dx_j^F}{dV} = 0 \quad (12)$$

where  $u_0^F$  is the inlet superficial velocity (m/s),  $V_R$  the total reactor volume (m<sup>3</sup>),  $x_j^F$  the mole fraction, and  $x_{j_0}^F$  the inlet mole fraction for species  $j$ .

Assuming that the catalyst and adsorbent particles have the same size, the pressure drop in a packed bed can be calculated using the Ergun equation:

$$-\frac{dP^F}{dV} = 10^{-6} \frac{f^F (G_m^F)^2}{A^F g_c d_p^F \mathbf{r}_F^F} \quad (13)$$

$$\text{at } V = 0, \quad P^F = P_0^F \quad (14)$$

$$f^F = \left( \frac{1 - \mathbf{e}_b^F}{(\mathbf{e}_b^F)^3} \right) \left( 1.75 + \frac{150(1 - \mathbf{e}_b^F)}{N_{\text{Re}}^F} \right) \quad (15)$$

$$N_{\text{Re}}^F < 500(1 - \mathbf{e}_b^F) \quad (16)$$

$$N_{\text{Re}}^F = d_p^F G_m^F / \mathbf{m}^F \quad (17)$$

where  $P^F$  is the feed-side pressure (bar),  $P_0^F$  the inlet feed-side pressure,  $\mu^F$  the viscosity (Pa·s),  $d_p^F$  the particle diameter in the feed side (m),  $G_m^F = \mathbf{r}_F^F \mathbf{m}^F$  the superficial mass flow velocity in the feed side ( $\text{kg}/\text{m}^2 \cdot \text{s}$ ),  $\mathbf{r}_F^F$  the density of the fluid ( $\text{kg}/\text{m}^3$ ), and  $g_c$  the gravity conversion factor equal to 1 in SI units.

Because the CMS membranes do not show substantial  $\text{CO}_2$  permeation [33], we assume that no adsorbent or catalyst is present in the permeate side. For the permeate side, the following equation is, therefore, utilized:

$$\frac{dC_j^P}{dt} + k \frac{dn_j^P}{dV} = \mathbf{a}_m k U_j (P_j^F - P_j^P) + (A^F)^2 \frac{d}{dV} \left( D_L^P \frac{dC_j^P}{dV} \right); \quad (18)$$

j=1,2,...n

where  $k = A^F/A^P$ , with  $A^P$  being the cross-sectional area on the permeate side ( $\text{m}^2$ ), and  $D_L^P$  ( $\text{m}^2/\text{s}$ ) is the axial Taylor-Aris dispersion coefficient on the permeate side[36] for empty tubes given as:

$$D_L^P = D_m^P + \frac{(u^P)^2 (d_t^P)^2}{192 D_m^P} \quad (19)$$

where  $D_m^P$  is the molecular diffusivity ( $\text{m}^2/\text{s}$ ),  $u^P$  is the velocity at the permeate side (m/s), and  $d_t^P$  is the membrane inside diameter (m). In the simulations, the conditions prevailing in the permeate side at the start of step (iv) are those prevailing at steady state during step (iii). In addition, during step (iv) the following conditions prevail in the permeate side:

$$V = 0; \quad \frac{dx_j^P}{dV} = -\frac{u_0^P (x_{j_0}^P - x_j^P)}{A^F D_L^P} \quad (20)$$

$$V = V_R; \quad \frac{dx_j^P}{dV} = 0 \quad (21)$$

where  $x_j^P$  is the mole fraction,  $x_{j_0}^P$  the inlet mole fraction for species  $j$  on the permeate side, and  $u_0^P$  the superficial flow velocity (m/s) at the inlet. Because no adsorbent or catalyst is present in the permeate side, we ignore any potential pressure drops.

The reactor conversion (based on CO, which is typically the limiting reagent) is defined by the following equation:

$$X_{CO} = \frac{n_{CO_0}^F - (n_{CO_{ex}}^F + n_{CO_{ex}}^P)}{n_{CO_0}^F} \quad (22)$$

where  $n_{CO_0}^F$  is the inlet molar flow rate of CO and  $n_{CO_{ex}}^F$  and  $n_{CO_{ex}}^P$  are the CO molar flow rates at the exit of the reactor feed and permeate sides correspondingly (mol/s). The yield of product hydrogen, defined as the fraction of moles of CO fed into the reactor that have reacted to produce hydrogen, is given by the following equation:

$$Y_{H_2} = \frac{(n_{H_{2,ex}}^F - n_{H_{2,0}}^F) + (n_{H_{2,ex}}^P - n_{H_{2,0}}^P)}{n_{CO_0}^F} \quad (23)$$

where  $n_{H_{2,ex}}^F$  and  $n_{H_{2,ex}}^P$  are the hydrogen molar flow rates at the exit of respectively the reactor feed and permeate sides and  $n_{H_{2,0}}^F$  and  $n_{H_{2,0}}^P$  the  $H_2$  molar flow rates potentially present at the inlet of the reactor feed and permeate sides (mol/s).  $Y_{H_2} = 1$  when all of the CO has reacted completely to produce  $CO_2$  and  $H_2$ .

Equations 6-23 can be written in dimensionless form by defining the following variables and groups:

$$\mathbf{t}_a = (k_a)^{-1}; \mathbf{t}_F = \frac{\mathbf{e}^F V_R}{A^F u_0^F}; \mathbf{g} = \frac{\mathbf{t}_F}{\mathbf{t}_a}; \mathbf{h} = \frac{V}{V_R}; u^F = \frac{Q^F}{A^F}; u_0^F = \frac{Q_0^F}{A^F}; \mathbf{x}^F = \frac{u^F}{u_0^F}; \mathbf{x}^P = \frac{u^P}{u_0^P};$$

$$\Psi^F = \frac{P^F}{P_0^F}; \Psi^P = \frac{P^P}{P_0^P}; \mathbf{w} = \frac{P_0^P}{P_0^F}; \mathbf{a}_j = \frac{MW_j}{MW_{H_2}}; x_j^F = \frac{P_j^F}{P^F}; x_j^P = \frac{P_j^P}{P^P}; \mathbf{t} = k_a \mathbf{t}; \mathbf{d}_j = \frac{U_j}{U_{H_2}};$$

$$K'_{eq1} = \frac{K_{eq1}}{(P_0^F)^2}; K'_{CO} = K_{CO} P_0^F; K'_{H_2} = K_{H_2} P_0^F;$$

$$Da = \frac{\mathbf{b}_c (1 - \mathbf{e}_b^F) \mathbf{r}_c k_1 (T_0) V_R RT}{A^F u_0^F (P_0^F)^{1.5}}; \mathbf{b}_{CO_2} = b_{CO_2} P_0^F; Pe = \frac{A^F u_0^F}{U_{H_2} V_R \mathbf{a}_m RT}$$

$$;\Theta^F = \frac{\mathbf{e}_b^F A^F D_L^F}{u_0^F V_R}; \Theta^P = \frac{A^F D_L^P}{u_0^P V_R}$$

$$Ha = \frac{(1 - \mathbf{b}_c)(1 - \mathbf{e}_b^F) V_R \mathbf{r}_a k_a RT m_{CO_2}}{A^F u_0^F P_0^F}; \quad \Lambda = \frac{Ha}{Da}; \quad \Omega = (Da)(Pe);$$

$$\Xi = 10^{-6} f^F \frac{(u_0^F)^2 MW_{H_2} V_R}{A^F g_c d_p^F RT}; \mathbf{l} = \frac{A^P u_0^P}{A^F u_0^F}; \mathbf{q}_{seq} = \frac{C_{seq}^F}{m_{CO_2}}; \mathbf{q}_s = \frac{C_s^F}{m_{CO_2}}; \quad (24)$$

The dimensionless equations equivalent to Equations 6-18 are

$$\begin{aligned} \mathbf{g} \frac{\partial \mathbf{x}_j^F}{\partial \mathbf{t}} = & \left( \mathbf{x}^F \frac{\partial \mathbf{x}_j^F}{\partial \mathbf{h}} + x_j^F \frac{\partial \mathbf{x}^F}{\partial \mathbf{h}} + \frac{x_j^F \mathbf{x}^F}{\Psi^F} \frac{\partial \Psi^F}{\partial \mathbf{h}} \right) \frac{Da \mathbf{d}_j}{\Omega} \left( x_j^F - x_j^P \mathbf{w} \frac{\Psi^P}{\Psi^F} \right) + Da \frac{1}{\Psi^F} R_j^F - Da \Lambda \frac{1}{\Psi^F} G_j^F + \\ & + \Theta^F \frac{\partial^2 x_j^F}{\partial \mathbf{h}^2} + 2\Theta^F \frac{1}{\Psi^F} \left( \frac{\partial x_j^F}{\partial \mathbf{h}} \right) \left( \frac{\partial \Psi^F}{\partial \mathbf{h}} \right), j=1,2,\dots,n-1 \end{aligned} \quad (25)$$

$$\frac{\partial \mathbf{x}^F}{\partial \mathbf{h}} = -\frac{\mathbf{x}^F}{\Psi^F} \frac{\partial \Psi^F}{\partial \mathbf{h}} - \frac{Da}{\Omega} \sum_j \mathbf{d}_j \left( x_j^F - x_j^P \mathbf{w} \frac{\Psi^P}{\Psi^F} \right) + Da \frac{1}{\Psi^F} \sum_j R_j^F - \Lambda Da \frac{1}{\Psi^F} G_{CO_2}^F \quad (26)$$



$$\frac{\mathbf{g}}{\mathbf{e}^F \mathbf{I} k} \frac{\partial x_j^P}{\partial t} = - \left( \mathbf{x}^P \frac{\partial x_j^P}{\partial \mathbf{h}} + x_j^P \frac{\partial \mathbf{x}^P}{\partial \mathbf{h}} + \frac{x_j^P \mathbf{x}^P}{\Psi^P} \frac{\partial \Psi^P}{\partial \mathbf{h}} \right) + \frac{Da}{\mathbf{I} \Omega} \mathbf{d}_j \left( x_j^F \frac{\Psi^F}{\mathbf{w} \Psi^P} - x_j^P \right) +$$

$$\Theta^P \frac{\partial^2 x_j^P}{\partial \mathbf{h}^2} + 2\Theta^P \frac{1}{\Psi^P} \left( \frac{\partial x_j^P}{\partial \mathbf{h}} \right) \left( \frac{\partial \Psi^P}{\partial \mathbf{h}} \right), j=1,2,\dots,n-1 \quad (27)$$

$$\frac{\partial \mathbf{x}^P}{\partial \mathbf{h}} = - \frac{\mathbf{x}^P}{\Psi^P} \frac{\partial \Psi^P}{\partial \mathbf{h}} + \frac{Da}{\mathbf{I} \Omega} \sum_j \mathbf{d}_j \left( x_j^F \frac{\Psi^F}{\mathbf{w} \Psi^P} - x_j^P \right) \quad (28)$$

$$\frac{\partial \Psi^F}{\partial \mathbf{h}} = - \Xi (\mathbf{x}^F)^2 \Psi^F \sum x_j^F \mathbf{a}_j \quad (29)$$

$$\frac{d\mathbf{q}_s^F}{dt} = \mathbf{q}_{s_{eq}}^F - \mathbf{q}_s^F \quad (30)$$

$$X_{CO} = \frac{x_{CO_0}^F - (x_{CO}^F \Psi^F \mathbf{x}^F)_{ex} + (x_{CO}^P \mathbf{I} \Psi^P \mathbf{w} \mathbf{x}^P)_{ex}}{x_{CO_0}^F} \quad (31)$$

$$Y_{H_2} = \frac{(x_{H_2}^F \Psi^F \mathbf{x}^F)_{ex} - x_{H_2_0}^F + (x_{H_2}^P \mathbf{I} \Psi^P \mathbf{w} \mathbf{x}^P)_{ex} - x_{H_2_0}^P \mathbf{I} \mathbf{w}}{x_{CH_4_0}^F} \quad (32)$$

where in dimensionless form:

$$\mathbf{G}_{CO_2}^F = (\mathbf{q}_{seq}^F - \mathbf{q}_s^F) \quad (33)$$

$$\mathbf{q}_{seq}^F = \frac{\mathbf{b}_{CO_2} x_{CO_2}^F \Psi^F}{1 + \mathbf{b}_{CO_2} x_{CO_2}^F \Psi^F} \quad (34)$$

and  $R_j$  are dimensionless forms of  $R_j$ . Equations 26 and 28 that express the dimensionless velocity distributions are obtained by overall mass balances in the feed and permeate sides. In the absence of substantial pressure drop in the permeate side in Equation 27,

$\Psi^P = 1$  and  $\frac{\partial \Psi^P}{\partial \mathbf{h}} = 0$ . The initial conditions at the start of the adsorption/reaction step are

those prevailing during step 3 previously described. In addition, the following boundary conditions also apply:

$$\mathbf{t} > 0; @ \mathbf{h} = 0; \quad ?^F = 1; \quad ?^P = 1 \quad (35)$$

$$\mathbf{x}^F = 1; \quad \mathbf{x}^P = 1 \quad (36)$$

$$\frac{\partial x_j^F}{\partial \mathbf{h}} = -\frac{1}{\Theta^F} (x_{j0}^F - x_j^F); \quad i=1, 2, \dots, n \quad (37)$$

$$\frac{\partial x_j^P}{\partial \mathbf{h}} = -\frac{1}{\Theta^P} (x_{j0}^P - x_j^P); \quad i=1, 2, \dots, n \quad (38)$$

$$\mathbf{t} > 0; \quad @ \quad \mathbf{h}=1; \quad \frac{\partial x_j^F}{\partial \mathbf{h}} = 0 \quad (39)$$

$$\frac{\partial x_j^P}{\partial \mathbf{h}} = 0 \quad (40)$$

where,  $s = \frac{\sum n_{j0}^P}{\sum n_{j0}^F} = \mathbf{I} \mathbf{w} \frac{\sum x_{j0}^P}{\sum x_{j0}^F}$  is the sweep ratio for the membrane reactor.

The system of coupled nonlinear partial differential Equations 25-34 and accompanying boundary conditions has been solved in MATLAB using the method of lines[37,38]. The system of partial differential equations was converted to a set of ordinary differential equations by discretizing the spatial derivative in the  $\mathbf{h}$  direction using a five-point-biased upwind finite-difference scheme to approximate the convective term. A fourth-order central-difference scheme has been used to approximate the diffusive term. For finite differences, the reactor volume was divided into  $n$  sections with  $n + 1$  nodes. The initial value ordinary differential equations and other explicit algebraic equations at a time  $\mathbf{t}$  were simultaneously solved using ode45.m, a MATLAB built-in solver for initial value problems for ordinary differential equations.

### 7.3 Performance Evaluation via Mathematical Simulation

We report here the behavior of the HAMR and AR simulating water gas shift reaction for hydrogen production with concomitant CO<sub>2</sub> removal. Figure 7.2 shows the hydrogen yield attained by both the AR and HAMR as a function of dimensionless time for different values of Wc/F (Wc is the total weight of the catalyst). The reactor temperature is 250°C, and a CO: H<sub>2</sub>: H<sub>2</sub>O feed ratio of 1:4:1.1 is utilized. Steam is used as the sweep gas. The reaction rate constants are experimentally determined in Sec. 7.3.1 and the membrane permeance are experimentally determined in Sec. 7.3.2. Table 7.5 lists the values of all of the other parameters utilized. Initially, the hydrogen yield for both reactors reaches high values, but it declines as the adsorbent becomes saturated and levels off at the corresponding values for the conventional membrane (in the case of HAMR) or the plug-flow reactor (in the case of AR). The HAMR performs better than the AR. For the conditions in Figure 7.2, the catalyst is sufficiently active that the plug-flow reactor yields (the AR yields level off at these values) approach equilibrium (~84% under the prevailing conditions) for all of the four Wc/F values utilized. On the other hand, the yields for the AR and HAMR systems (prior to the adsorbent saturation) and the MR yields (the HAMR yields level off at these yields) depend on Wc/F, increasing as Wc/F increases, as expected.

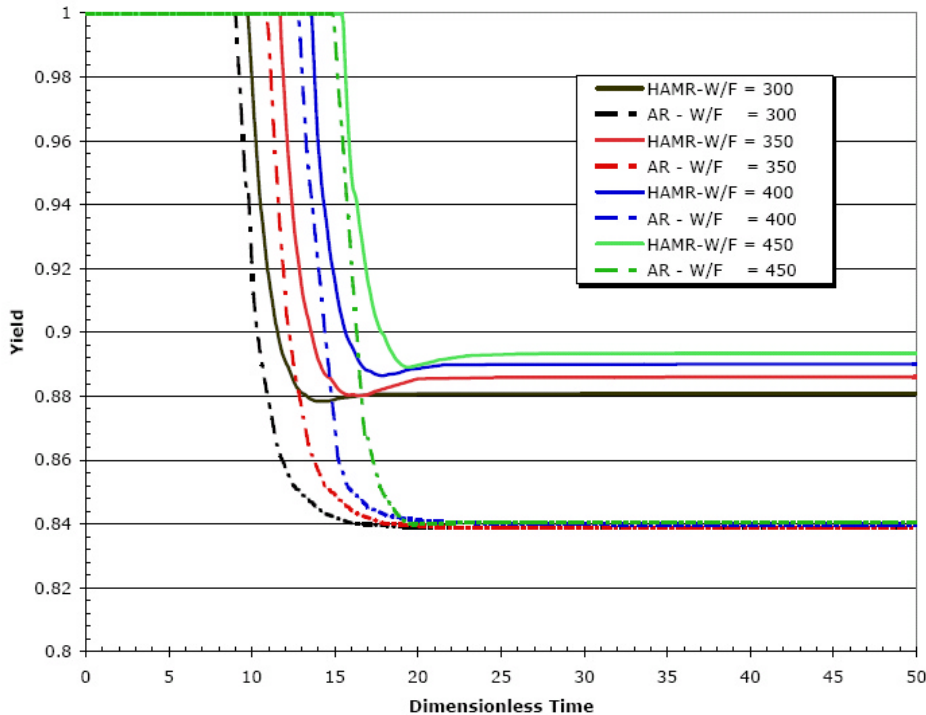


Figure 7.2 Hydrogen yield for the HAMR and AR systems for various Wc/F

Figure 7.3 shows the CO<sub>2</sub> feed-side exit concentration (wet basis) profiles for the HAMR and AR. Low concentrations are observed while the adsorbent remains unsaturated; the concentrations sharply increase, however, after the adsorbent is saturated. The CO<sub>2</sub> concentration for HAMR is higher than that for MR as a result of the hydrogen permeation out of the reactor in the HAMR system.

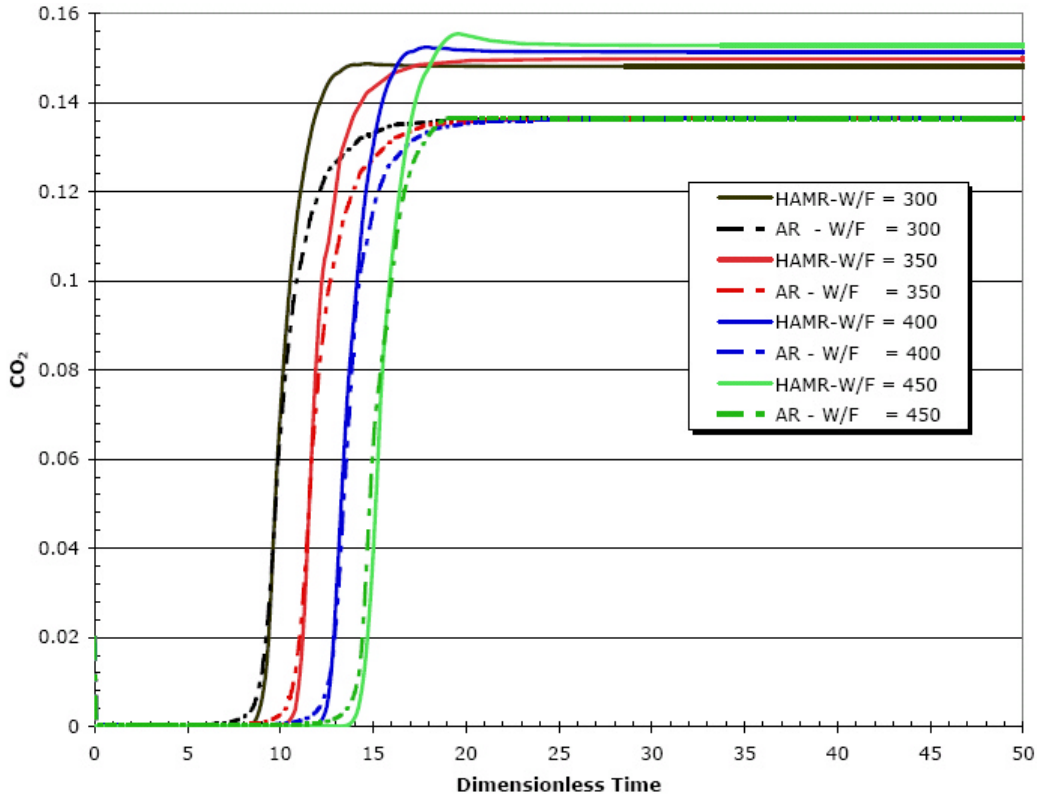


Figure 7.3 CO<sub>2</sub> concentration (wet basis) profiles at the reactor outlet for the AR and HAMR systems at different Wc/F.

Figure 7.4 shows the CO concentration (wet basis) profiles in the permeate-side exit of the HAMR, together with the corresponding exit concentration values for the AR. Clear from Figure 7.4 is the advantage that the HAMR system provides in terms of reduced CO concentrations in the hydrogen product over the AR system, in addition to improved hydrogen yields. The CO concentration in AR jumps to a high value and stays there till the adsorbent gets saturated; after adsorbent saturation there is another big jump and CO concentration levels off to a higher final value as compared to HAMR CO-ppm levels. Thus, unreacted CO is expected to distribute throughout the AR rather quickly. Even though the adsorbent has not been saturated with CO<sub>2</sub>; the established equilibrium assures the presence of unreacted CO.

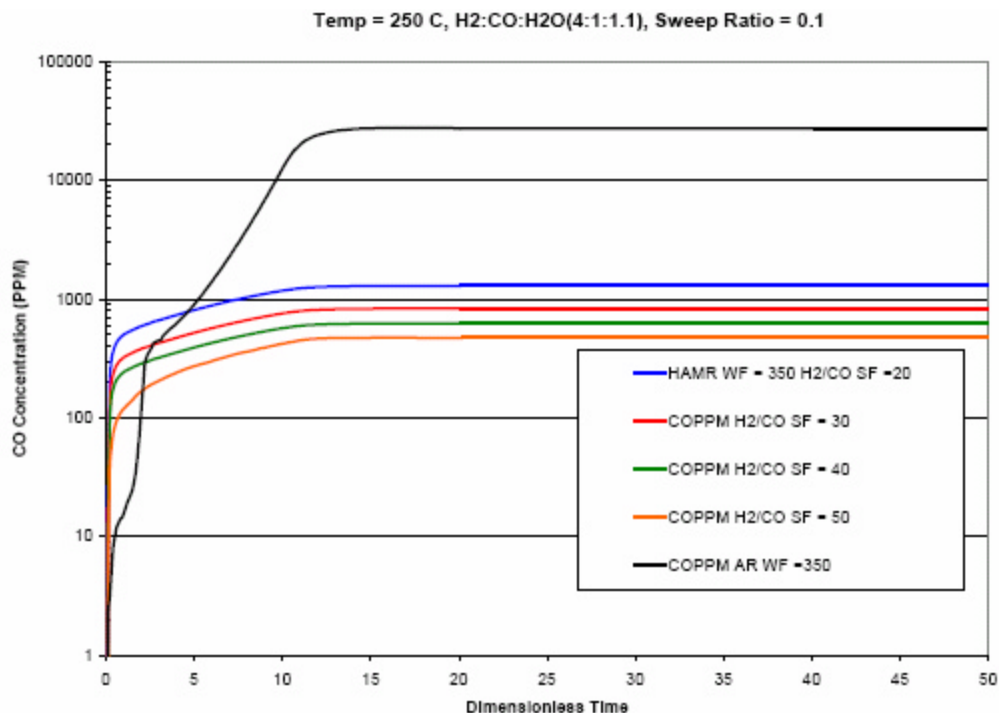


Figure 7.4 CO concentration (wet basis, in ppm) profiles in the HAMR permeate-side exit and AR exit for different  $Wc/F$

A potential disadvantage of the HAMR system, when compared to the AR system, is that only a fraction of the hydrogen product ends up in the permeate stream, while the rest remains mixed with the unreacted CO and CO<sub>2</sub> products in the feed-side stream. The hydrogen recovery is, of course, a strong function of the membrane permeation characteristics and the other operating conditions in the reactor, increasing with increasing membrane permeance and feed-side pressure. Furthermore, one must also take into account, when comparing both reactors that even for the AR system one must eventually separate the hydrogen out of the exit stream and that similar hydrogen losses are likely to occur.

Figure 7.5 shows the effect of  $\beta_c$  (the fraction of reactor volume occupied by catalyst) on the hydrogen yields, while keeping the total volume occupied by the solids and the  $Wc/F$  constant. Decreasing  $\beta_c$  (i.e., increasing the fraction of sorbent present), while maintaining  $Wc/F$  constant, has a significant beneficial effect on the hydrogen yield and also on the product purity for both the HAMR and AR systems (see Figure 7.6 for the CO content of the hydrogen product).

$\beta_c$  is the volume of reactor occupied by the catalyst. In these experiments the total reactor volume stays constant. By decreasing  $\beta_c$  one simultaneously changes both the catalyst volume and the adsorbent volume. Since there is a much larger volume of adsorbent than catalyst changing  $\beta_c$  mostly affects the level of final conversion.

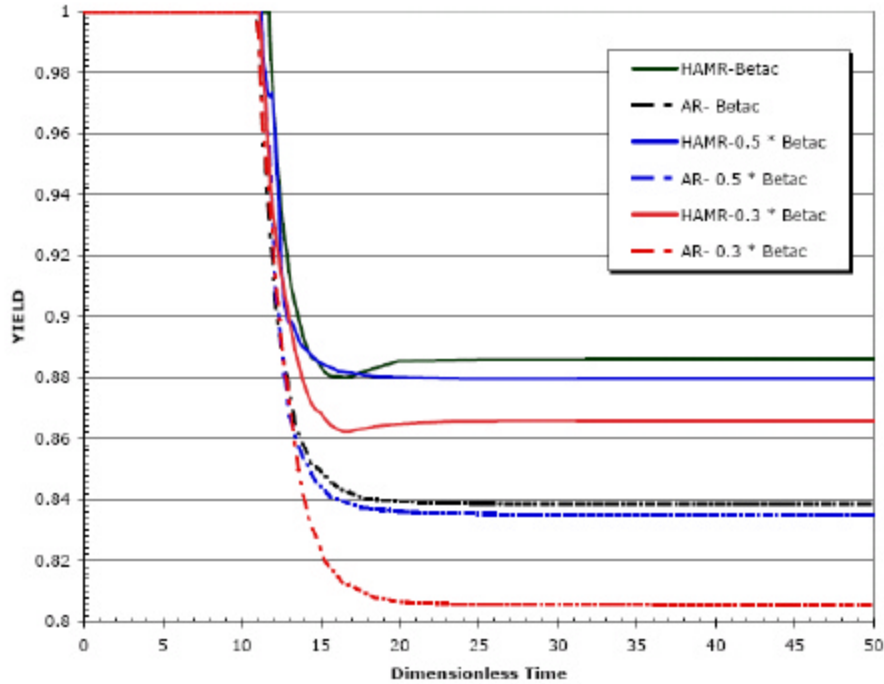


Figure 7.5 Effect of  $\beta_c$  on the hydrogen yields for both the HAMR and AR systems.

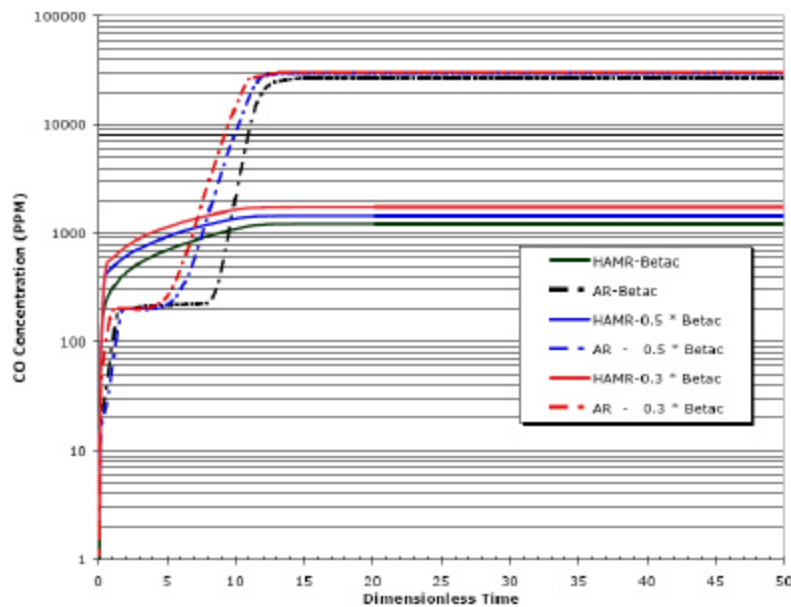


Figure 7.6 Effect of  $\beta_c$  on the CO exit concentration (wet basis, in ppm) for the HAMR (permeate) and AR systems

The effect of using an adsorbent with improved characteristics is shown in Figure 7.7. The hydrogen yields for the HAMR and the AR systems are compared for three values of  $Ha$  (Hatta Number)/ $Da$  (Damkohler Number), one corresponding to the adsorbent of our experimental result shown in Sec. 7.3.2 and two other cases with corresponding values 3 and 5 times larger. A more effective adsorbent significantly expands the "time window" of operation for both the AR and HAMR systems before regeneration must commence. It also significantly increases the hydrogen yields attained. The degree of run time increase is nearly proportional to the degree of increase in the adsorbent capacity as expected. In addition the effect of  $Ha/Da$  appears similar to both HAMR and AR system.

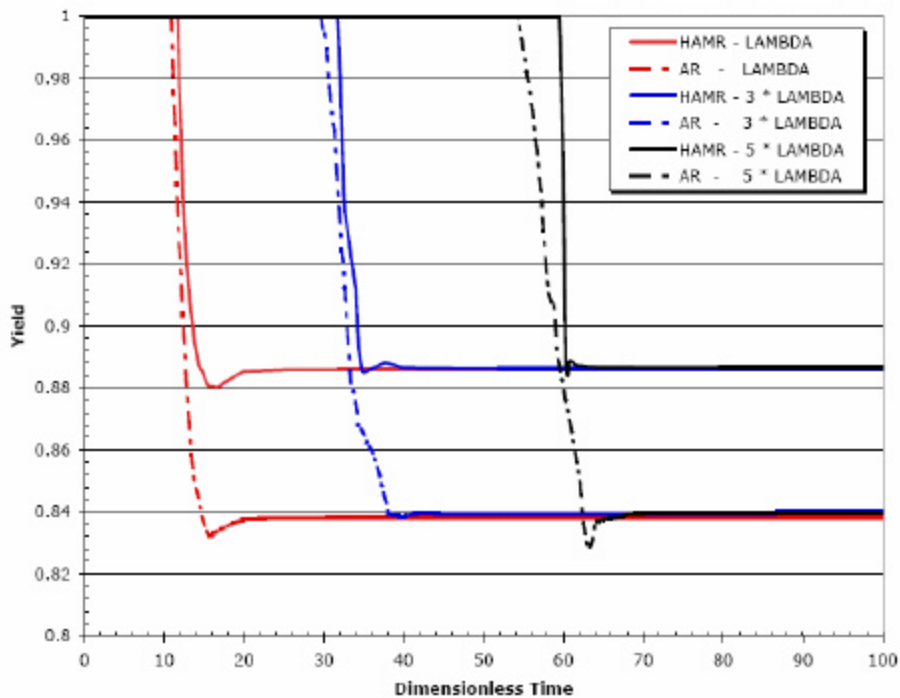


Figure 7.7 Effect of  $Ha/Da$  on the hydrogen yield.

The effect of membrane transport characteristics is shown in Figure 7.8, where the reactor yields corresponding to five different membranes (i.e., five different values of  $(Da)(Pe)$  ((Damkohler Number)(Peclet Number))) are shown. One corresponding to the CMS membrane and the other four membranes has values that are 0.1, 0.333, 0.5, and 5 times the base value. The HAMR system hydrogen yields do benefit from increased hydrogen permeance. The hydrogen yield increases from  $\sim 0.85$  to  $\sim 0.92$  when the permeance increases, i.e.  $(Da)(Pe)$  decreases (since  $(Da)(Pe)$  is inversely proportional to hydrogen permeance).

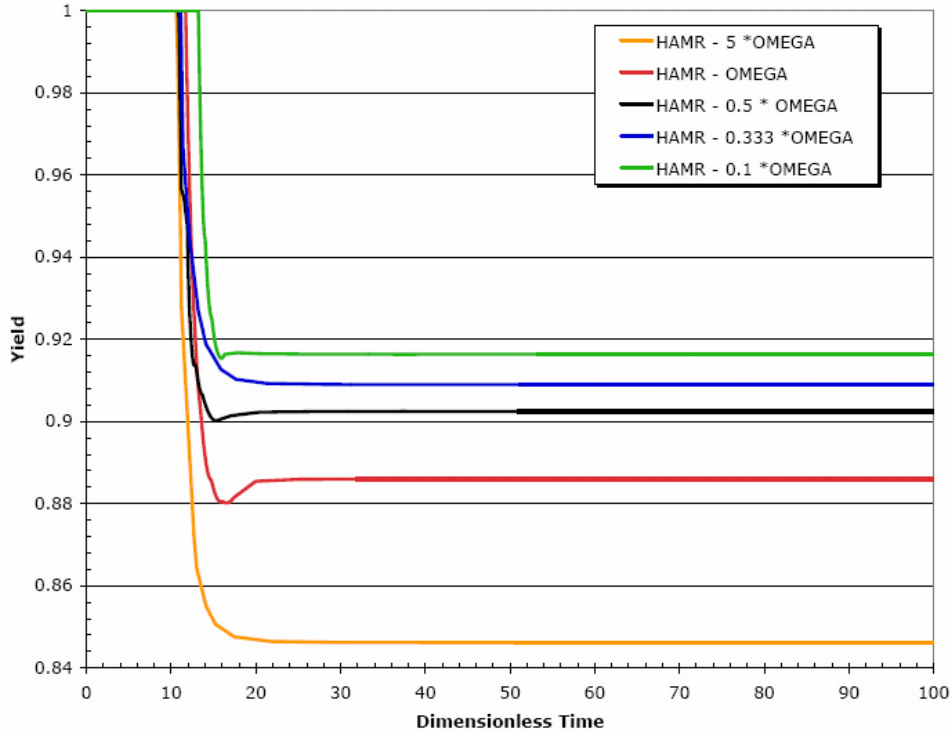


Figure 7.8 Effect of (Da)(Pe) on the hydrogen yield.

Figure 7.9 shows the effect of hydrogen permeance on hydrogen recovery. As expected, increasing the hydrogen permeance has a very beneficial effect on hydrogen recovery, with very high hydrogen recoveries (~87%) attained for 10 times the base case.

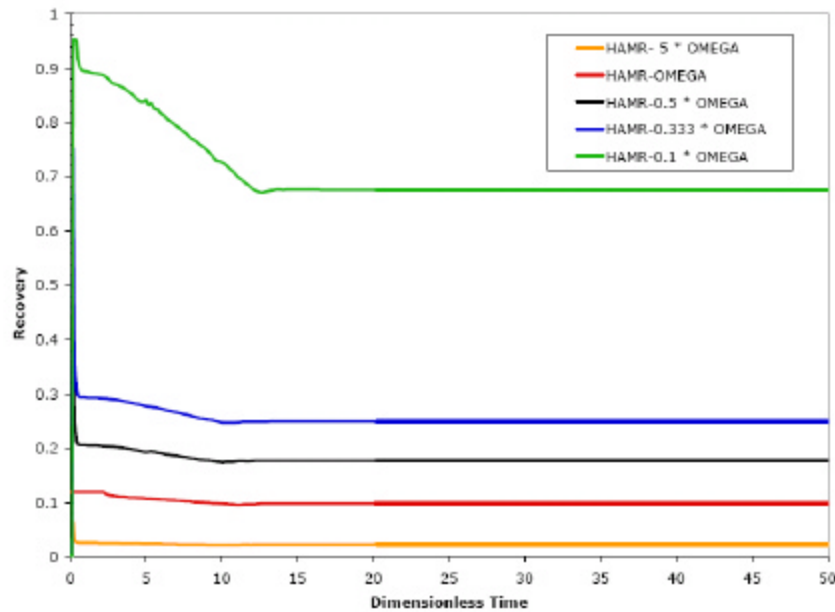


Figure 7.9 Effect of (Da)(Pe) on the hydrogen recovery.



Figure 7.10 shows the effect of the sweep ratio on the hydrogen yield of the HAMR system. Increasing the sweep ratio improves the reactor performance; however, the effect saturates quickly. As shown in Figure 7.10, when the sweep ratio approaches 0.4 time of the base case, the incremental improvement on hydrogen yield becomes insignificant.

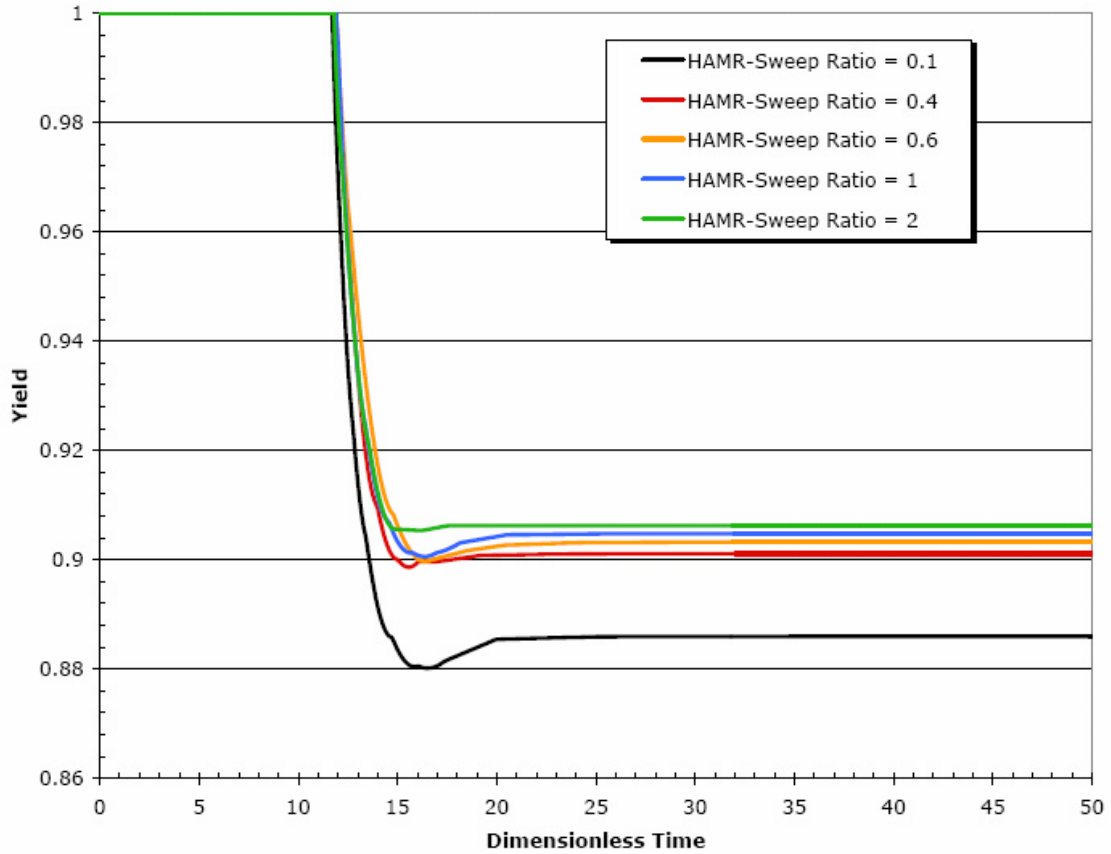


Figure 7.10 Effect of the sweep ratio on the hydrogen yield.

## 7.4 Experimental Verification

### 7.4.1 Kinetic Study on Catalytic Water Gas Shift Reaction

Kinetic constants for water gas shift reaction are critical input parameters for the performance simulation of our proposed HAMR. A laboratory scale reactor system was established as shown in Figure 7.11 to study the reaction kinetics, which was then employed for the HAMR study. Synthetic feed was prepared from pure gas cylinders with mass flow controllers. The reactor temperature was kept at the target temperature within a constant temperature box. The effluent from the reactor was analyzed with mass spectroscopy after water dropout via condensation.

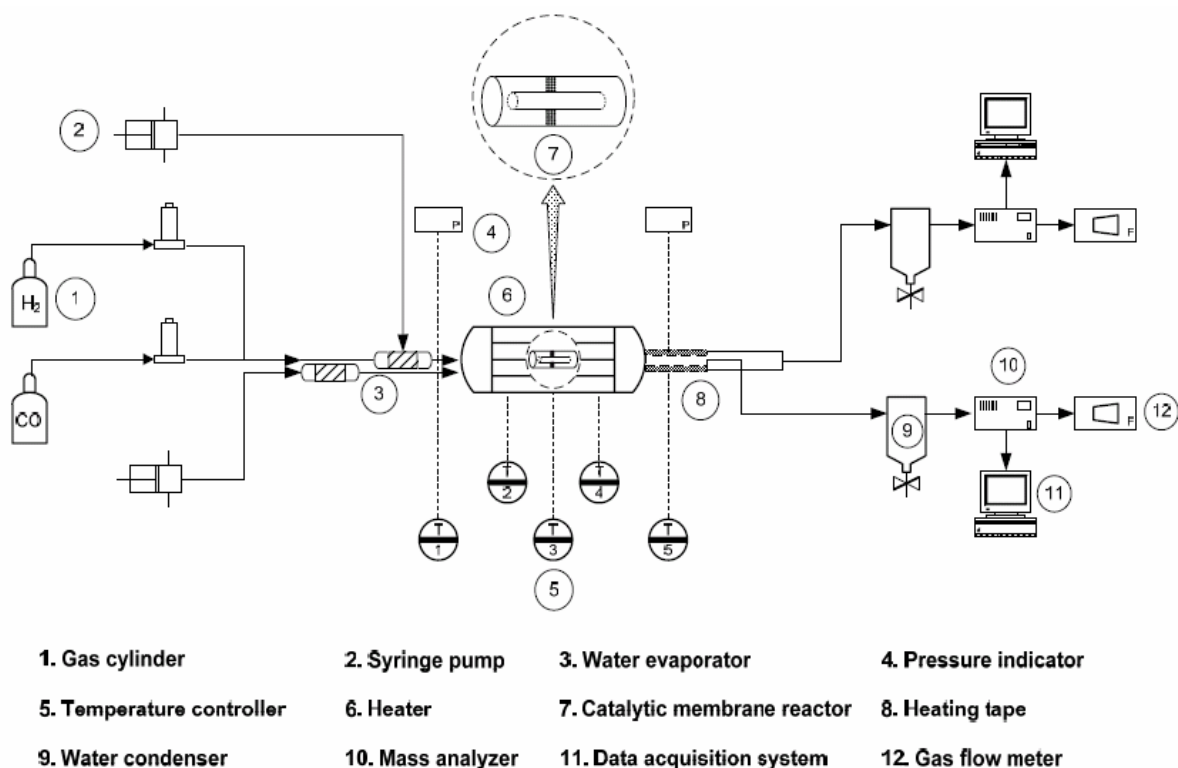


Figure 7.11 Schematic of lab-scale catalytic membrane reactor system

The operating condition selected for determining the reaction kinetics of low temperature shift of the water gas shift reaction is listed in Table 7.2. Three different temperatures were selected, i.e., 205, 225 and 250°C, which covered the temperature range recommended by the catalyst manufacturer for the low temperature shift. Pressure of the reactor was kept at ~50 psig. The feed composition selected for this study was CO:H<sub>2</sub>:H<sub>2</sub>O = 1.0:4.0:2.5. W/F<sub>0</sub> selected ranged from ~30 to as high as ~467, which spanned a wide operating condition for us to obtain representative kinetic parameters.

Table 7.1 Operating conditions for water gas shift reaction kinetic study.

Composition	CO : H2 : H2O = 1.0 : 4.0 : 2.5					
Pressure(psig)	52.5		50		50	
Temperature(C)	205		225		250	
Weight of Catalyst(g)	10		30		30	
Kinetic data	W/Fo CO (g*hr/mol)	CO Conversion(%)	W/Fo CO (g*hr/mol)	CO Conversion(%)	W/Fo CO (g*hr/mol)	CO Conversion(%)
	1.56E+02	77.96	4.67E+02	96.52	4.67E+02	96.63
	7.78E+01	68.47	2.33E+02	95.23	2.33E+02	95.21
	5.19E+01	61.66	1.56E+02	92.22	1.56E+02	92.94
	3.89E+01	50.93	1.17E+02	88.19	1.17E+02	88.43
	3.11E+01	47.96	9.33E+01	79.38	9.33E+01	86.35
2.59E+01	38.48	7.78E+01	71.78	7.78E+01	77.86	
Pre-exponential factor g-mol/(g cat*hr*bar^0.4)	1.52E+08		2.60E+08		2.80E+08	

The reaction rate constants obtained experimentally were then used as shown below to determine the pre-exponential factor and the activation energy.

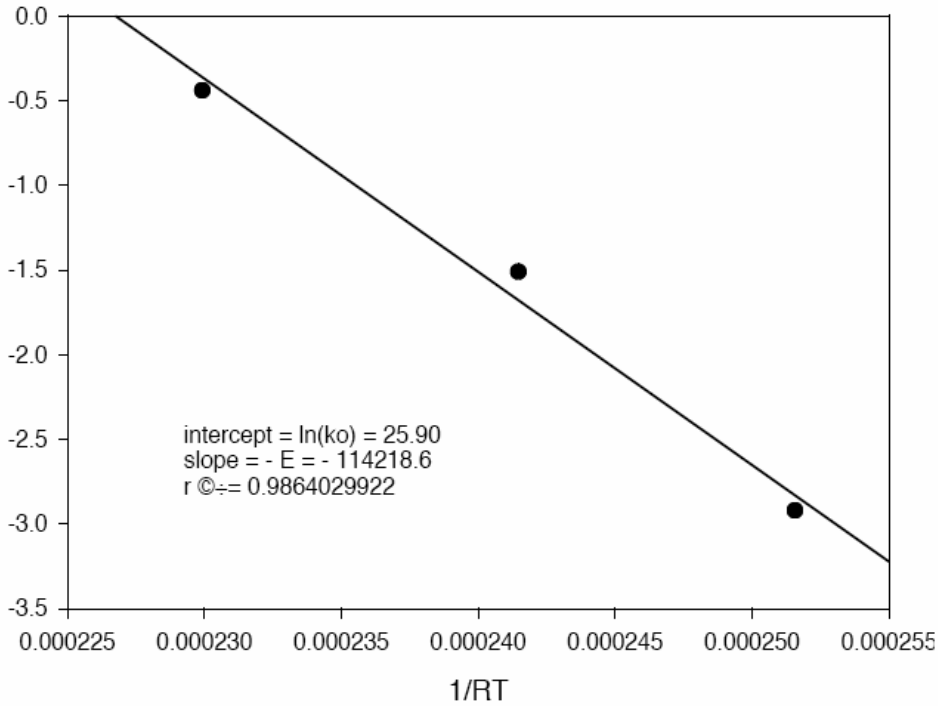


Figure 7.12 Kinetic Parameters Calculations

Table 7.2 Kinetic parameters obtained using experimental data

<b>k<sub>o</sub></b>	<b>1.77E+11</b>
<b>g-mol/(g cat*hr*bar<sup>0.4</sup>)</b>	
<b>E</b>	<b>114218.6</b>
<b>(J/mol)</b>	
<b>E</b>	<b>114.22</b>
<b>(KJ/mol)</b>	

The pre-exponential factor and the activation energy determined based upon the operating condition listed in Table 7.3 above. These kinetic parameters were used in the mathematical simulation.

#### 7.4.2 Adsorption Isotherm

In addition to the catalytic reaction parameters, the adsorption equilibrium capacity and rate for the CO<sub>2</sub> affinity adsorbent, hydrotalcite, used in this study were experimentally determined. The lab scale adsorption isotherm study was performed in an experimental setup presented in Figure 7.13. The adsorption isotherm for CO<sub>2</sub> on hydrotalcite at 250°C was determined by measuring the difference in the input and output CO<sub>2</sub> molar flow rates. The experimental data were then fitted with the Langmuir adsorption isotherm as presented in Figure 7.14.

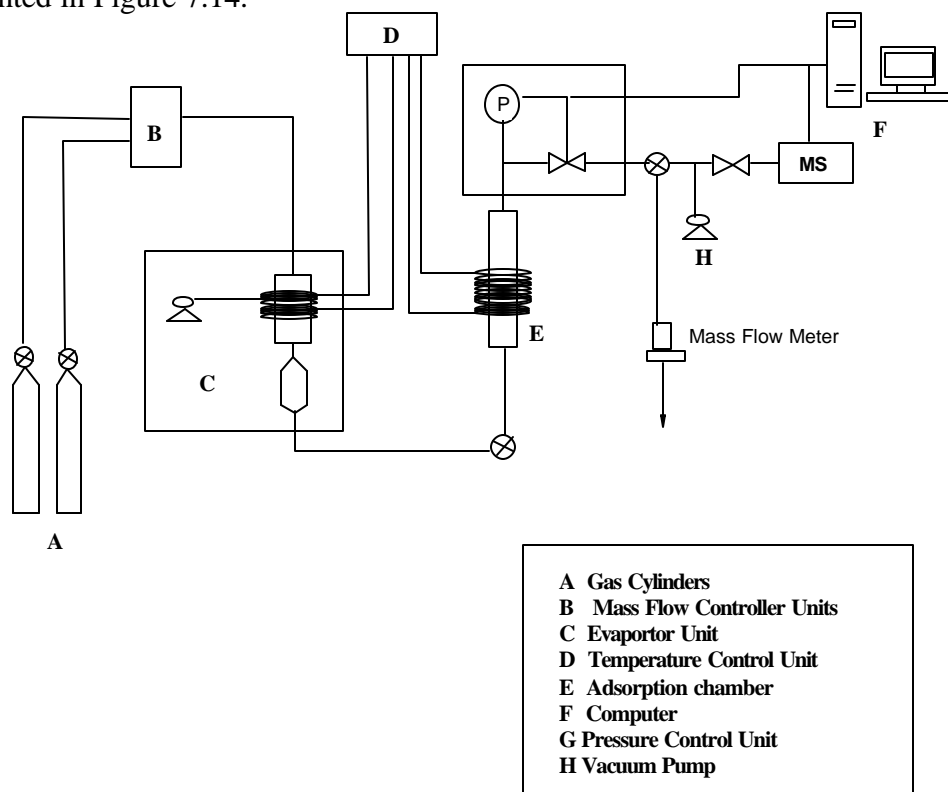


Figure 7.13 Schematic of the lab scale adsorptive system for CO<sub>2</sub> adsorption isotherm study.

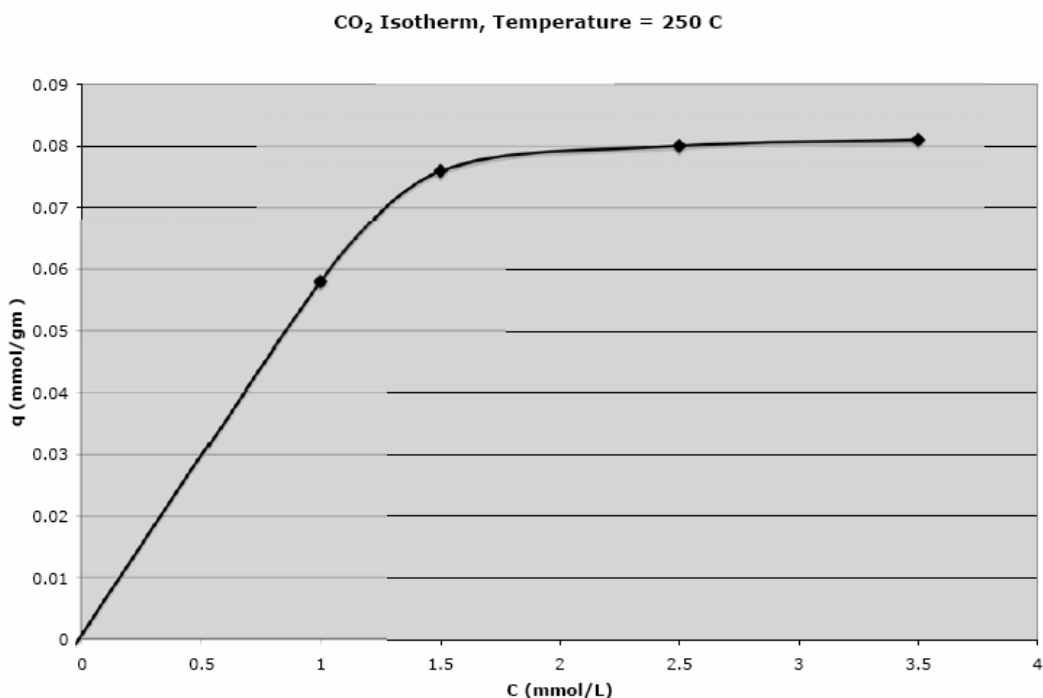


Figure 7.14 Adsorption isotherm of the hydrocalcite adsorbent used for catalytic membrane reactor study.

#### 7.4.3 Characterization of Membranes Selected for HAMR Study

The carbonaceous hydrogen selective membrane was prepared by us and sent to our subcontractor, USC, for performing the catalytic reaction study. Both single component and mixture permeation study were conducted to determine the permeation and separation properties required for the mathematical simulation study. Permeation study of single component, including H<sub>2</sub>, CO, CO<sub>2</sub>, H<sub>2</sub>O, CH<sub>4</sub>, N<sub>2</sub> and He, was performed at 15 to 45 psig as shown in Table 7.4. The results from the measurements from both groups are relatively consistent although minor variation exists, which may be resulted from contamination of the membrane and experimental errors. Then the mixture separation study was performed using two different mixture compositions as shown in Table 7.4. The selectivities obtained from the mixtures were about 50% lower than those obtained from the single component. Specifically hydrogen permeance reduced while CO and CO<sub>2</sub> permeances increase significantly. No explanations could be offered for this discrepancy between the single and the mixture separation differences.

Table 7.3 Permeation and Separation Characteristics of CMS Hydrogen Selective Membrane

Surface Area (m<sup>2</sup>) 0.0027928      Dimension of permeance : [ m<sup>3</sup>/(m<sup>2</sup>\*hr\*bar) ]

	Single gas						Mixed Gas			
	USC(15psig)		USC(45psig)		MP&T(20psig)		H <sub>2</sub> /CO/CO <sub>2</sub> /CH <sub>4</sub>		H <sub>2</sub> /CO/CO <sub>2</sub> /CH <sub>4</sub> /H <sub>2</sub> O	
							5 : 1 : 1 : 1		2.5 : 1 : 1 : 1 : 2.5	
							53 psig		53 psig	
	Permeance	S.F. on H <sub>2</sub>	Permeance	S.F. on H <sub>2</sub>	Permeance	S.F. on H <sub>2</sub>	Permeance	S.F. on H <sub>2</sub>	Permeance	S.F. on H <sub>2</sub>
H <sub>2</sub>	0.3107	1.00	0.3737	1.00	0.3718	1.00	0.2799	1.00	0.2726	1.00
CO	0.0060	51.78	0.0087	42.80			0.0137	20.46	0.0129	21.16
CO <sub>2</sub>	0.0156	19.92	0.0244	15.32	0.0144	25.82	0.0297	9.42	0.0333	8.19
H <sub>2</sub> O	0.4094	0.76							0.4079	0.67
CH <sub>4</sub>	0.0033	94.16	0.0085	43.90	0.0043	86.85	0.0067	41.62	0.0064	42.79
N <sub>2</sub>	0.0057	54.95	0.0074	50.18	0.0067	55.41				
He	0.2066	1.50	0.2886	1.29	0.2610	1.42				

#### 7.4.4 Experimental Results from HAMR Study

Some preliminary laboratory study was performed to verify the mathematical simulation presented in Figure 7.2 to 7.11. The M&P hydrogen selective membrane characterized in Sec. 7.4.3 was used as the reactor to selectively remove hydrogen from the water gas shift reaction products, while the CO<sub>2</sub>-affinity hydrotalcite adsorbent was packed inside the membrane reactor along with a commercial WGS catalyst. The physical parameters, including catalyst and adsorbent dosages, are listed in Table 7.2. The CO conversion vs time was presented in Figure 7.14. As expected a nearly complete conversion of CO was achieved in the beginning of the reactor run, i.e., up to about 40 minutes. Then, the conversion declined and finally settled at 91.5% when the adsorbent was saturated. In comparison with the simulation presented in Figure 7.5, the overall conversion profiles obtained experimentally here is consistent in general with the predicted profile shown in Figure 7.5. However, the experimental results failed to demonstrate a nearly complete 100% conversion in the beginning of the reactor study. Considering the highly fluctuation of the data in this narrow range (i.e., 2%), it would not be surprised that the reactant by-pass through the bed, unsteady state flow pattern due to significant product loss by adsorption, and others, led to the back-mixing of the reactant and product, which diluted the conversion in the beginning of the reaction run. On the other hand, equilibrium conversion of 91.5% was higher than the predicted 89.5% conversion. Slow adsorption of CO<sub>2</sub> by hydrotalcite may be responsible for this higher-than-predicted conversion level. In spite of these minor discrepancies, the HAMR performance prediction is generally consistent with the experimental results. Comparison between the simulation and the experiment is made below in terms of the conversion level and the breakthrough times:

For W/F =350, simulation time for CO conversion in high levels is ~ 27 minutes, where as experimental data shows ~ 40 minutes.

For W/F =350, simulation time for CO<sub>2</sub> breakthrough is ~ 21 minutes, where as experimental data shows ~ 15-18 minutes.

For W/F =300, simulation time for CO conversion in high levels is ~ 19 minutes, where as experimental data shows ~ 20 minutes.

For W/F =300, simulation time for CO<sub>2</sub> breakthrough is ~ 17 minutes, where as experimental data shows ~ 20 minutes.

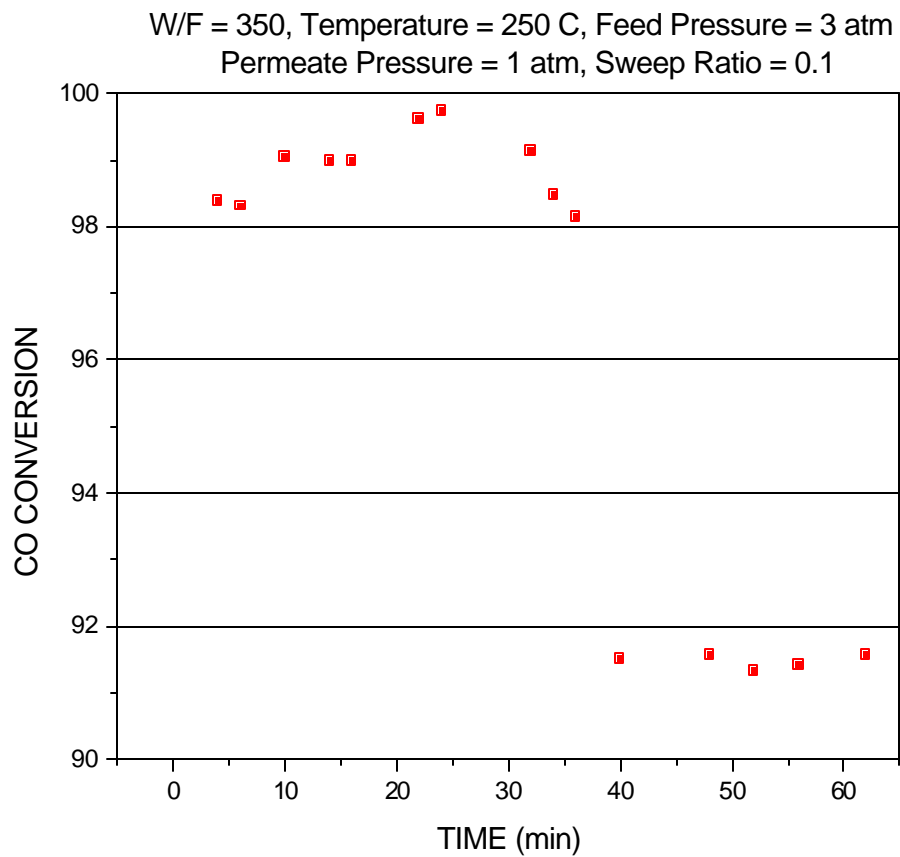


Figure 7.15 CO conversion vs time for HAMR system with W/F=350, T=250C, feed pressure of 3 bar, and permeate pressure =bar, and sweep ratio of 0.1.

W/F =350, Temperature = 250 C, Feed Side Pressure = 3 atm  
Permeate Side Pressure = 1 atm, Sweep ratio = 0.1

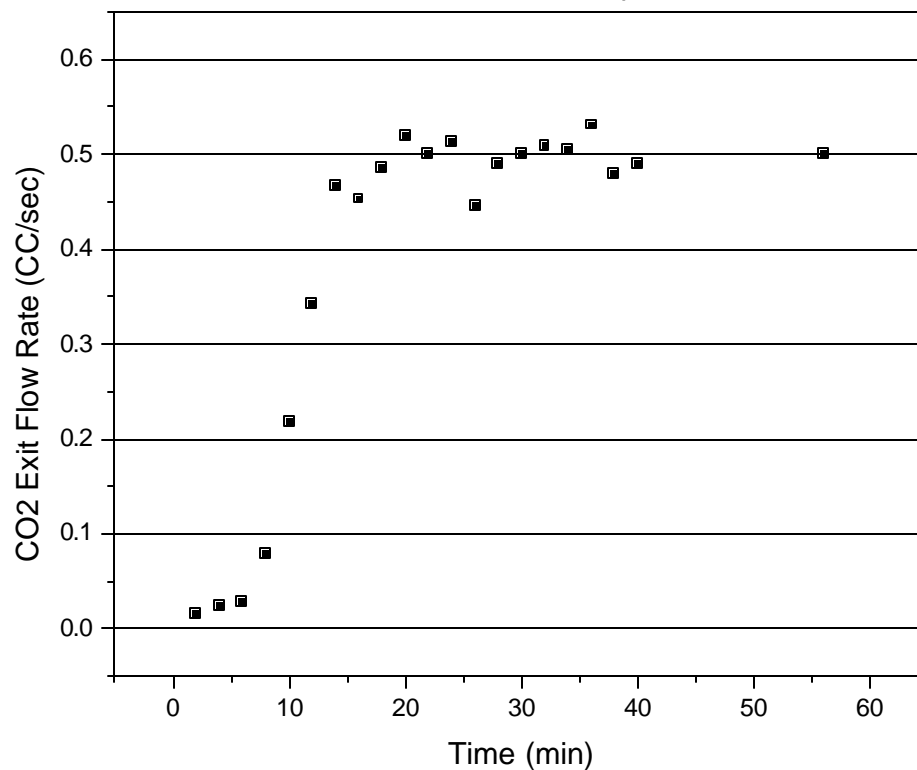


Figure 7.16 CO<sub>2</sub> Concentration at the exit of the reactor

Additional experimental study was performed with W/F=300. The results are presented in Figure 7.16 and 7.18. Since the transition period for CO conversion (i.e., from 100% to the equilibrium % level) in the case of W/F=350 is  $\approx$ 15 minutes, which is much shorter than 20-40 minutes in the case of W/F=300, it is likely that reaction kinetic dominates in this operating condition. Since the transition profile of CO is nearly independent of W/F in this range, it is possible that the reaction kinetics used in this study may require revision.



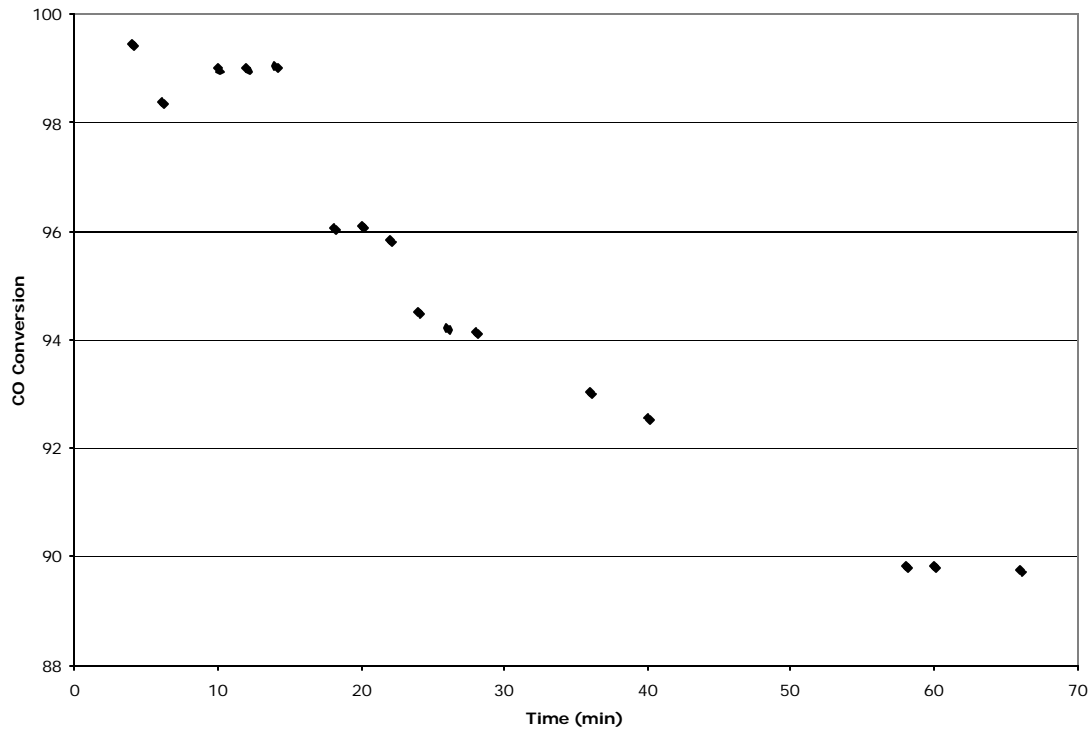


Figure 7.17 CO conversion vs time for HAMR with W/F=300.

W/F = 300, Temperature = 250 C, Feed Side Pressure = 3 atm,  
Permeate Side Pressure = 1 atm, Sweep Ratio = 0.1

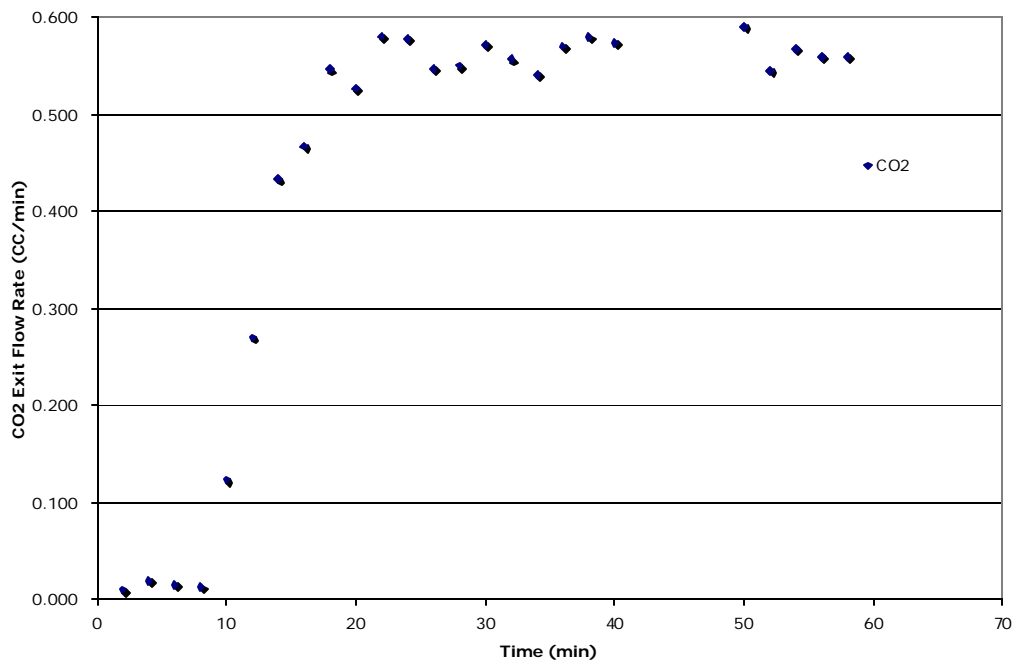


Figure 7.18 CO<sub>2</sub> breakthrough concentrations at the exit of the HAMR reactor.  
For W/F = 300

The experimental results obtained in this study are generally consistent with the mathematical prediction in terms of CO conversion vs time, CO<sub>2</sub> breakthrough profile and the effect of W/F. However, the nearly complete CO conversion in the beginning of the reaction was not demonstrated by the experimental results, most likely as a result of the non-ideal flow pattern in the small lab-scale reactor. The general trend on the effect of W/F predicted by the simulation was verified by the experimental results although additional improvement in reaction kinetics may be required to use as a quantitative predictive tool.

## 7.5 Preliminary Economic Analysis

No comprehensive economic analysis was performed due to the time constraint during this project. Instead, a qualitative economic analysis was performed to demonstrate the potential cost advantage of the proposed hybrid reactor. The two outstanding advantages of our proposed reactor are the enhanced conversion and the reduced CO contaminant concentration. According to our simulation selected in this study, CO conversion of 88% can be achieved with our proposed reactor, vs 80% based upon the thermodynamic equilibrium. This would translate into about 10% reduction in the hydrogen production cost. In addition, the CO concentration of 1,000 ppm was achieved with our proposed reactor, as opposed to ~30,000 ppm of the conventional reactor in a side-by-side comparison selected in this study. As a result, the conventional reactor requires additional WGS reaction to further reduce the CO concentration. This reduced and compact WGS reactor of our proposed process would result in significant capital cost savings because WGS is considered one of the least efficient steps in hydrogen production. Once the optimization of the membrane and adsorbent materials is accomplished, we recommend a comprehensive economic evaluation based upon the mathematical model developed here to quantitatively estimate potential capital and operating cost savings of our proposed hybrid reactor.

## 7.6 Conclusions

We have investigated a novel reactor system, termed the HAMR, for hydrogen production through water gas shift reaction with concomitant CO<sub>2</sub> removal for sequestration. The HAMR combines the reaction and membrane separation steps with adsorption on the membrane feed or permeate sides. The HAMR system is of potential interest to pure hydrogen production for proton exchange membrane (PEM) fuel cells for various mobile and stationary applications. Key conclusions are drawn below:

- The reactor characteristics have been investigated for a range of temperature, pressure, and other experimental conditions relevant to the aforementioned applications and compared with the behavior of the traditional packed-bed reactor, the conventional MR, and an AR. The HAMR outperforms all of the other more conventional reactor systems. It exhibits enhanced CO conversion, hydrogen yield, and product purity for meeting the product purity requirements for PEM operation.

- The performance of the HAMR system depends on the various operating parameters, including the reactor space time, the temperature, and the membrane and adsorbent properties. One of the key advantages of the HAMR system over the corresponding AR system (in addition to improvements in yield) is its ability to deliver a product with a significantly lower CO content through the use of membranes, which preferentially allow the permeation of the hydrogen while excluding CO and other reactants and products. This may be the primary reason for adopting such reactors for fuel-cell application, where a CO-free product is at a premium.
- The disadvantage of the HAMR system is, similar to that for the ARs, in that they require regeneration of the spent adsorbent for continuous operation. The HAMR system may require a dual reactor system, where one of the reactors is in operation while the other reactor is being regenerated.
- Use of effective adsorbent results, for example, in increased yields and longer operational time windows. More highly permeable membranes also increase the reactor yield but, more importantly, also increase the hydrogen recovery ratio.

Our preliminary experimental results are consistent with the prediction with the mathematical model developed here. Additional experimental validation of the HAMR system and extension of the model to incorporate adsorbent regeneration are recommended. Finally, incorporation of temperature to simulate the HAMR under the non-isothermal condition is necessary to truly reflect the WGS reaction, an exotherm reaction.

Table 7.4 Parameter Values Used in Simulations

Parameter	Value	Dimension
$b_{CO_2}$	22.21	bar <sup>-1</sup>
$d_p^F$	0.001	m
$m_{CO_2}$	0.104	mol/kg
$P_0^F$	3	bar
$P_0^P$	2	bar
$s$	0.1	- (Base case)
$T$	250	°C (Base case)

<b><i>g</i></b>	0.4536	-
<b><i>d</i><sub>1</sub></b>	1	-
<b><i>d</i><sub>2</sub></b>	0.0742	-
<b><i>d</i><sub>3</sub></b>	0.189	-
<b><i>d</i><sub>5</sub></b>	0.375	-
<b><i>e</i><sup>F</sup></b>	0.4	-
<b><math>\Lambda</math></b>	0.029	-
<b><i>l</i></b>	0.3	-
<b><i>m</i><sup>F</sup></b>	0.0004	Pa.s
<b><i>t</i><sub>F</sub></b>	10.43	-
<b><i>t</i><sub>a</sub></b>	22.98	-
<b><math>\Omega</math></b>	18.51	-
<b><i>w</i></b>	0.33	-

---

## Nomenclature :

$A^F$	cross sectional area for the reactor feed side ( $m^2$ )
$A^P$	cross sectional area for the reactor permeate side ( $m^2$ )
$b_{CO_2}$	Langmuir model adsorption equilibrium constant for $CO_2$ ( $bar^{-1}$ )
$C_j^F$	gas phase concentration of species j in the feed side ( $kmol/m^3$ )
$C_j^P$	gas phase concentration of species j in the permeate side ( $kmol/m^3$ )
$C_s$	solid phase concentration of $CO_2$ ( $mol/kg$ )
$C_{seq}$	equilibrium solid phase concentration of $CO_2$ ( $mol/kg$ )
$Da$	Damkohler number (dimensionless)
$D_L^F$	axial dispersion coefficient in the feed side ( $m^2/s$ )
$D_L^P$	axial dispersion coefficient in the permeate side ( $m^2/s$ )
$D_m^F$	molecular diffusivity in feed side ( $m^2/s$ )
$D_m^P$	molecular diffusivity in permeate side ( $m^2/s$ )
$d_i^P$	membrane inside diameter (m)
$d_p^F$	particle diameter in feed side (m)
$f^F$	friction factor (dimensionless)
$F_j$	molar flux ( $mol/m^2.s$ )
$g_c$	gravity conversion factor
$G_m^F$	superficial mass flow velocity in the feed side ( $kg/m^2.s$ )
$G_j^F$	dimensionless adsorption rate for species j
$G_j^F$	adsorption rate for species j ( $mol/kg.s$ )
$Ha$	Hatta number (dimensionless)
$k$	$A^F/A^P$
$k_a$	LDF mass transfer coefficient ( $s^{-1}$ )
$K_j$	adsorption equilibrium constant for $CH_4$ , $CO$ and $H_2$ ( $bar^{-1}$ )
$K_{H_2O}$	dissociative adsorption constant of water
$K'_{CO}$	dimensionless kinetic parameter (dimensionless)
$K_{eq1}, K_{eq3}$	equilibrium constant of reaction I and III in Table 1. ( $bar^2$ )
$K_{eq2}$	equilibrium constant of reaction I in Table 1. (dimensionless)
$m_{CO_2}$	Langmuir model total adsorbent capacity constant for $CO_2$ ( $mol/kg$ )
$MW_j$	molecular weight of species j
$N_{Re}^F$	Reynolds number for feed side

$n_{j_0}^F$	inlet molar flow rate for feed side (mol/s)
$n_{j_0}^P$	inlet molar flow rate for permeate side (mol/s)
$n_j^F$	molar flow rate for component $j$ in the feed side (mol/s)
$n_j^P$	molar flow rate for component $j$ in the permeate side (mol/s)
$n_{i,ex}^F$	molar flow rates at the exit of the reactor for component $i$ in the feed side (mol/s)
$n_{i,ex}^P$	molar flow rates at the exit of the reactor for component $i$ in the permeate side (mol/s)
$P_0^F$	inlet feed side pressure(bar)
$Pe$	Peclet Number
$P^F$	feed side pressure (bar)
$P_j^F$	partial pressure of component $j$ in the membrane feed side (bar)
$P_j^P$	partial pressure of component $j$ in the membrane permeate side (bar)
$Q_0^F$	volumetric flow rate (m <sup>3</sup> /s)
$R$	ideal gas constant (m <sup>3</sup> .bar/mol.K)
$r_i$	rate of reaction for $i^{th}$ equation (kmol/kg.s)
$r_i'$	dimensionless rate of reaction for $i^{th}$ equation
$R_j$	reaction rate expression for species $j$ (kmol/kg.s)
$R'_j$	dimensionless reaction rate expression for species $j$
$s$	sweep ratio
$t$	time (second)
$T$	absolute temperature (K)
$T_0$	reference temperature (K)
$u_0^F$	superficial flow velocity at the inlet on feed side (m/s)
$u_0^P$	superficial flow velocity at the inlet on permeate side (m/s)
$u^F$	superficial flow velocity on feed side (m/s)
$u^P$	superficial flow velocity on permeate side (m/s)
$U_j$	membrane permeance for component $j$ (mol/m <sup>2</sup> .bar.s)
$V$	reactor volume (m <sup>3</sup> )
$V_R$	total reactor volume (m <sup>3</sup> )
$W_c$	catalyst weight (kg)
$X_{CH_4}$	methane conversion (dimensionless)

$x_{j0}^F$	inlet mole fraction for species j in the feed side
$x_{j0}^P$	inlet mole fraction for species j in the permeate side
$x_j^F$	mole fraction for species j in the feed side
$x_j^P$	mole fraction for species j in the permeate side
$y_j$	mole fraction of component j
$Y_{H_2}$	hydrogen yield (dimensionless)

### *Subscripts*

0	entrance condition
<i>ads</i>	adsorbent condition
<i>eq.</i>	equilibrium
<i>ex</i>	exit
<i>j</i>	chemical species

### *Superscripts*

<i>F</i>	feed side
<i>P</i>	permeate side

### *Greek Letters*

$\mathbf{a}_m$	membrane area per feed side reactor volume ( $\text{m}^2/\text{m}^3$ )
$\mathbf{a}_j$	$\text{MW}_j/\text{MW}_{\text{H}_2}$
$\mathbf{b}_c$	fraction of the reactor volume occupied by catalysts
$\mathbf{b}_{\text{CO}_2}$	$b_{\text{CO}_2} P_0^F$ (dimensionless)
$\mathbf{g}$	$\mathbf{t}_F/\mathbf{t}_a$ (dimensionless)
$\Delta H_a$	heat of adsorption (kJ/mol)
$\mathbf{d}_j$	separation factor (dimensionless)
$\mathbf{e}^F$	total feed side bed porosity

$\mathbf{e}_b^F$	bed porosity in the feed side
$\mathbf{x}^F$	$u^F / u_0^F$ (dimensionless)
$\mathbf{x}^P$	$u^P / u_0^P$ (dimensionless)
$\mathbf{h}$	$V / V_R$ (dimensionless)
$\Theta^F$	$\mathbf{e}_b^F A^F D_L^F / u_0^F V_R$ (dimensionless)
$\Theta^P$	$A^F D_L^P / u_0^P V_R$ (dimensionless)
$\mathbf{q}_s^F$	$C_s^F / m_{CO_2}$ ,(dimensionless)
$\mathbf{q}_{seq}^F$	$C_{seq}^F / m_{CO_2}$ ,(dimensionless)
$\Lambda$	$Ha / Da$ (dimensionless)
$\mathbf{l}$	$A^P u_0^P / A^F u_0^F$ (dimensionless)
$\mathbf{m}^F$	viscosity (Pa.s)
$\Xi$	$10^{-6} f^F ((u_0^F)^2 MW_{H_2} V_R / A^F g_c d_p^F RT)$ (dimensionless)
$\mathbf{r}_a$	adsorbent density (kg/m <sup>3</sup> )
$\mathbf{r}_c$	catalyst density (kg/m <sup>3</sup> )
$\mathbf{r}_F^F$	fluid density (kg/m <sup>3</sup> )
$\mathbf{t}$	$k_a t$ (dimensionless)
$\mathbf{t}_F$	$\mathbf{e}^F V_R / A^F u_0^F$ (dimensionless)
$\mathbf{t}_a$	$(k_a)^{-1}$ (dimensionless)
$\Psi^F$	$P^F / P_0^F$ (dimensionless)
$\Psi^P$	$P^P / P_0^P$ (dimensionless)
$\Omega$	(Da)(Pe) (dimensionless)
$\mathbf{w}$	$P_0^P / P_0^F$ (dimensionless)



## Literature Cited

1. Park B. *Models and Experiments with Pervaporation Membrane Reactors Integrated with a Water Removal Adsorbent System*, Ph.D. Thesis, University of Southern California, Los Angeles, California, 2001.
2. Park, B.; Tsotsis, T. T. Models and Experiments with Pervaporation Membrane Reactors Integrated With an Adsorbent System. *Chem. Eng. Proc.* **2004**, 43, 1171.
3. Choi, Y.; Stenger, H.G. Water Gas Shift Reaction Kinetics and Reactor Modeling for Fuel Cell Grade Hydrogen. *J. Power Sources* **2003**, 124, 432.
4. Darwish, N. A.; Hilal, N.; Versteeg, G.; Heesink, B. Feasibility of the Direct Generation of Hydrogen for Fuel-cell-powered Vehicles by on-board Steam Reforming of Naphtha. *Fuel*. **2003**, 83, 409.
5. Liu, Z.; Roh, H.; Park, S. Hydrogen Production for Fuel Cells Through Methane Reforming at Low Temperatures. *J. Power Sources* **2002**, 111, 83.
6. Semelsberger, T. A.; Brown, L. F.; Borup, R. L.; Inbody, M. A. Equilibrium Products from Autothermal Processes for Generating Hydrogen-rich Fuel-cell Feeds. *Int. J. Hydrogen Energ.* **2004**, 29, 1047.
7. Elnashaie, S.S.E.H.; Adris, A.; Al-Ubaid, A.S.; Soliman, M.A. On the Non-monotonic Behavior of Methane-steam Reforming Kinetics. *Chem. Eng. Sci.* **1990**, 45, 491.
8. Xu, J.; Froment, G.F. Methane Steam Reforming, Methanation and Water-gas Shift: I. Intrinsic Kinetics. *AIChE J.* **1989**, 35, 88.
9. Han, C.; Harrison, D.P. Simultaneous Shift Reaction and Carbon Dioxide Separation for the Direct Production of Hydrogen. *Chem. Eng. Sci.* **1994**, 49, 5875.
10. Hwang, S. Inorganic Membranes and Membrane Reactors, *Korean J. Chem. Eng.* **2001**, 18, 775.
11. Lim, S.Y.; Park, B.; Hung, F.; Sahimi, M.; Tsotsis, T.T. Design Issues of Pervaporation Membrane Reactors for Esterification. *Chem. Eng. Sci.* **2002**, 57, 4933.
12. Park, B.; Ravi-Kumar, V.S.; Tsotsis, T.T. Models and Simulation of Liquid-phase Membrane Reactors. *Ind. Eng. Chem. Res.* **1998**, 37, 1276.
13. Nam, S.W.; Yoon, S.P.; Ha, H.Y.; Hong, S.; Maganyuk, A.P. Methane Steam Reforming in a Pd-Ru Membrane Reactor. *Korean J. Chem. Eng.* **2000**, 17, 288.
14. Saracco, G.; Specchia, V. Catalytic Inorganic-membrane Reactors: Present Experience and Future Opportunities. *Catal. Rev.-Sci. Eng.* **1994**, 36, 305.
15. Sanchez, J.; Tsotsis, T.T. *Catalytic Membranes and Membrane Reactors*; Wiley-VCH: Weinheim, 2002.
16. Xiu, G. H.; Li, P.; Rodrigues, A. E. Subsection-controlling Strategy for Improving Sorption-enhanced Reaction Process. *Chem. Eng. Res. Des.* **2004**, 82, 192.
17. Xiu, G.; Li, P.; Rodrigues, A. E. Adsorption-enhanced Steam-methane Reforming with Intraparticle-diffusion Limitations. *Chem. Eng. J. (Amsterdam, Netherlands)* **2003**, 95, 83.
18. Xiu, G.; Li, P.; Rodrigues, A. E. New Generalized Strategy for Improving Sorption-enhanced Reaction Process. *Chem. Eng. Sci.* **2003**, 58, 3425.
19. Xiu, G.; Soares, J. L.; Li, P.; Rodrigues, A. E. Simulation of Five-step One-bed Sorption-enhanced Reaction Process. *AIChE J.* **2002**, 48, 817.
20. Xiu, G.; Li, P.; Rodrigues, A. E. Sorption-enhanced Reaction Process with Reactive Regeneration. *Chem. Eng. Sci.* **2002**, 57, 3893.

21. Lee, D. K.; Baek, I. H.; Yoon, W. L. Modeling and Simulation for the Methane Steam Reforming Enhanced by in Situ CO<sub>2</sub> Removal Utilizing the CaO Carbonation for H<sub>2</sub> Production. *Chem. Eng. Sci.* **2004**, 59, 931.
22. Ding, Y.; Alpay, E. Adsorption-enhanced Steam-methane Reforming. *Chem. Eng. Sci.* **2000**, 55, 3929.
23. Ortiz, A. L.; Harrison, D. P. Hydrogen Production Using Sorption-Enhanced Reaction. *Ind. Eng. Chem. Res.* **2001**, 40, 5102.
24. Balasubramanian, B.; Ortiz, A. L.; Kaytakoglu, S.; Harrison, D. P. Hydrogen from Methane in a Single-step Process. *Chem. Eng. Sci.* **1999**, 54, 3543.
25. Waldron, W. E.; Hufton, J. R.; Sircar, S. Production of Hydrogen by Cyclic Sorption Enhanced Reaction Process. *AIChE J.* **2001**, 47, 1477.
26. Hufton, J. R.; Mayorga, S.; Sircar, S. Sorption-enhanced Reaction Process for Hydrogen Production. *AIChE J.* **1999**, 45, 248.
27. Ding, Y.; Alpay, E. Equilibria and Kinetics of CO<sub>2</sub> Adsorption on Hydrotalcite Adsorbent. *Chem. Eng. Sci.* **2000**, 55, 3461.
28. Park, B. A Hybrid Adsorbent-membrane Reactor (HAMR) System for Hydrogen Production. *Korean J. Chem. Eng.* **2004**, 21, 782.
29. Chen, Z.; Elnashaie, S. S. E. H. Bifurcation Behavior and Efficient Pure Hydrogen Production for Fuel Cells Using a Novel Autothermic Membrane Circulating Fluidized-Bed (CFB) Reformer: Sequential Debottlenecking and the Contribution of John Grace. *Ind. Eng. Chem. Res.* **2004**, 43, 5449.
30. Prasad, P.; Elnashaie, S. S. E. H. Novel Circulating Fluidized-Bed Membrane Reformer Using Carbon Dioxide Sequestration. *Ind. Eng. Chem. Res.* **2004**, 43, 494.
31. Prasad, P.; Elnashaie, S. S. E. H. Coupled Steam and Oxidative Reforming for Hydrogen Production in a Novel Membrane Circulating Fluidized-Bed Reformer. *Ind. Eng. Chem. Res.* **2003**, 42, 4715.
32. Chen, Z.; Yan, Y.; Elnashaie, S. S. E. H. Novel Circulating Fast Fluidized-bed Membrane Reformer for Efficient Production of Hydrogen from Steam Reforming of Methane. *Chem. Eng. Sci.* **2003**, 58, 4335.
33. Ciora, R. J.; Fayyaz, B.; Liu, P. K. T.; Suwanmethanond, V.; Mallada, R.; Sahimi, M.; Tsotsis, T. T. Preparation and Reactive Applications of Nanoporous Silicon Carbide Membranes. *Chem. Eng. Sci.* **2004**, 59, 4957.
34. Edwards, M. F.; Richardson, J. F. Gas Dispersion in Packed Beds. *Chem. Eng. Sci.* **1968**, 23, 109.
35. Karger, J.; Ruthven, D.M. *Diffusion in Zeolites and Other Microporous Solids*; Wiley Publishers: New York, 1992.
36. Levenspiel, O. *Chemical Reaction Engineering*, 3rd Edition; Wiley: New York, 1998.
37. Schiesser, W. E. *The Numerical Method of Lines: Integration of Partial Differential Equations*; Academic Press: San Diego, 1991.
38. Vande Wouwer, A.; Saucez, P.; Schiesser, W. E. Simulation of Distributed Parameter Systems Using a Matlab-Based Method of Lines Toolbox: Chemical Engineering Applications. *Ind. Eng. Chem. Res.* **2004**, 43, 3469.
39. Vasileiadis, S. P. *Catalytic Ceramic Membrane Reactors for the Methane-Steam Reforming Reaction: Experiments and Simulation*, Ph.D. Thesis, University of Southern California, Los Angeles, California 1994

## Chapter 8

### Overall Conclusions

This chapter summarizes the overall conclusions drawn from this study.

#### LDH Materials for CO<sub>2</sub>-Affinity Membranes and Adsorbents

- *In-situ* DRIFTS, DTA, TG/MS and HTXRD techniques were applied in this study to investigate the thermal evolution behavior of the Mg-Al-CO<sub>3</sub> LDH as a function of temperature and atmosphere. The LDH materials exhibits CO<sub>2</sub> affinity beginning at temperature >190°C. The LDH maintains its double layer structure up to 280°C. Beyond this temperature, the degradation of the LDH structure was observed under the inert atmosphere studied here. However, the LDH structure can be restored when the atmosphere exposed is appropriate.
- The LDHs are shown capable of CO<sub>2</sub> exchanging reversibly for a broad region of conditions. These experimental observations qualify the LDH as base material for the formation of CO<sub>2</sub> permselective membranes and CO<sub>2</sub>-affinity adsorbents for high temperature membrane reactor applications as proposed in this project. The ability to reversibly adsorb CO<sub>2</sub> is critical from the standpoint of being able to regenerate the adsorbents. The presence of a relatively mobile CO<sub>2</sub> phase within the LDH structure is important in determining the permeation rate through the membrane.

#### Synthesis and Characterization of CO<sub>2</sub>-Affinity Membranes

- The CO<sub>2</sub> permeation enhancement via the LDH material was demonstrated in several experimental membranes prepared in this project. The two synthesis techniques and one post-treatment technique developed here successfully demonstrated the technical feasibility of the formation of the LDH-based membrane. Additional work with the focus on minimization of defects is recommended to upgrade the CO<sub>2</sub> selectivity and permeance for future commercial use.
- Combining the observations from permeance, pore size distribution, EDAX and SEM, we concluded that the hydrotalcite crystals were deposited within the pore size of the starting Al<sub>2</sub>O<sub>3</sub> membranes with the pore sizes of 40Å, 500 Å, and 0.2µm. >90% gas permeance was reduced and the pore size was reduced dramatically, capable of delivering Knudsen selectivity or better. This LDH-based membrane via in-situ crystallization is suitable for post-treatment by the CVD/I technique.
- Post treatment by CVD with the protocol we developed is effective in reducing the residual permeance of the LDH membrane to a minimum. For instance, the CO<sub>2</sub> permeance of 0.26 m<sup>3</sup>/m<sup>2</sup>/hr/bar at 300°C was observed for one of the membranes after the post treatment by CVD/I technique. Further, our analysis indicates that >50% of the CO<sub>2</sub> permeance is likely attributed to the enhancement by the LDH

materials. The balance is contributed by defects remaining in the membrane.

- The ideal selectivity for CO<sub>2</sub>/N<sub>2</sub> of ~1.6 at 100 to 300°C was obtained for the LDH membrane prepared via in-situ crystallization and the CVD/I post treatment. In comparison with the ideal selectivity through Knudsen diffusion of 0.8, the selectivity obtained from the LDH membrane is about double of what delivered by the Knudsen diffusion. Evidently, the enhanced selectivity is not sufficient to be commercially viable. An optimization study is necessary to reduce the defect to a minimum via the membrane synthesis; thus, minimal post treatment is required to achieve the CO<sub>2</sub> enhancement without sacrificing permeance significantly.
- The slip casting technology developed here successfully developed a LDH membrane with the residual pore size of <40Å while keeping most of the original permeance, i.e., 30 to 40 m<sup>3</sup>/m<sup>2</sup>/hr/bar available, which could be an ideal starting material for the post treatment with CVD/I. Thus, the slip casting technique could be a promising LDH synthesis approach. No post treatment study is performed for this type of the LDH membrane due to the time constraint.
- Another type of membranes, carbonaceous base, demonstrated significant selectivity for CO<sub>2</sub>/N<sub>2</sub>, i.e., 4 to 10, up to 220°C, which was much beyond the Knudsen selectivity. Surface affinity of the membrane toward CO<sub>2</sub> was identified as the dominating mechanism at this operating temperature range. Selectivity at this level is comparable or higher than the selectivity of CO<sub>2</sub>/N<sub>2</sub> reported in the literature at the proposed reaction temperature. Pore size reduction was attempted without any success in boosting the CO<sub>2</sub> affinity. Additional study including characterization of this type of membrane in a mixture environment is recommended for future development.

#### Characterization of CO<sub>2</sub>-Affinity Adsorbents

- Diffusivity constants and adsorption isotherms for carbon dioxide in Mg-Al-CO<sub>3</sub> LDH2 at 200 - 250°C were determined by the gravimetric method. Diffusivity constants determined by experiments and those obtained by molecular dynamic simulations are in good qualitative agreement.
- The experimental results for CO<sub>2</sub> uptake vs pressure have been evaluated with the Langmuir and various empirical adsorption isotherm equations. It was observed that the heterogeneity of the material and the interaction between CO<sub>2</sub> and LDH increased with temperature. Also it was found that the experimental data were nonlinearly fitted best with the Toth equation based on  $\chi^2$  values.
- Our study observed that the amount of CO<sub>2</sub> uptake and the BET surface area increased as the particle size decreased. When the uptake amount was normalized with the BET surface area, it was found that the specific uptake amount was fairly constant for all the ranges of particle sizes. The adsorption isotherm obtained from data with different particle sizes of LDH were evaluated with Langmuir isotherm and

Langmuir-Freundlich equation. It was observed that the values of  $b_{CO_2}$  and  $n$  were relatively constant for the whole range of particle sizes. In summary, the adsorption isotherm can be described with the proposed specific property if the particle size effect is significant.

#### Hybrid Reactors for Water Gas Shift Reaction

- The HAMR combines the reaction and membrane separation steps with adsorption on the membrane feed or permeate sides. The reactor characteristics have been investigated for a range of temperature, pressure, and other experimental conditions relevant to the aforementioned applications and compared with the behavior of the traditional packed-bed reactor, the conventional MR, and an AR. The HAMR outperforms all of the other more conventional reactor systems. It exhibits enhanced CO conversion, hydrogen yield, and product purity.
- One of the key advantages of the HAMR system over the corresponding AR system (in addition to improvements in yield) is its ability to deliver a product with a significantly lower CO content through the use of membranes, which preferentially allow the permeation of the hydrogen while excluding CO and other reactants and products. This may be the primary reason for adopting such reactors for fuel-cell application, where a CO-free product is at a premium.
- The disadvantage of the HAMR system is, similar to that for the ARs, in that the HAMR requires regeneration of the spent adsorbent. For continuous operation; the HAMR may require a dual reactor system, where one of the reactors is in production while the other reactor is being regenerated.
- Our preliminary experimental results are consistent with the prediction with the mathematical model. Additional experimental validation of the HAMR system and the expansion of the model to incorporate adsorbent regeneration are recommended. Finally, incorporation of temperature as a variable to simulate the HAMR under the non-isothermal condition is necessary to truly reflect the WGS reaction, an exothermic reaction.

## Acronyms

A:	Arrhenious constant
AR:	Adsorptive reactor
BET:	Brunauer-Emmett-Teller
CMS:	Carbon molecular sieve
CVD/I:	Chemical Vapor Deposition/Infiltration
D:	Diffusivity
DA:	Double Alkoxide
DCP:	Inductively Coupled Plasma
DSC:	Differential Scanning Calorimetry
DTA:	Differential Thermal Analysis
DRIFTS:	Diffuse Reflectance Infrared Fourier Transform Spectroscopy
E:	Activation energy
HAMR:	Hybrid adsorbption-membrane reactor
HT	Hydrotalcite
HTXRD:	High temperaure x-ray diffraction
ICP:	Inductive Ccoupling plasma
IGCC:	Integrated aas combined cycle
LDF:	Linear driving force
LDH:	Layered double hydroxide
LHV:	Lower Heating Value
LTS:	Low temperature shift
$M_{\infty}$ :	Amount uptaken at complete saturation
MB-MS:	Molecular Beam Mass Spectrometry
MR:	Membrane reactor
MS:	Mass spectroscopy
Mt:	Amount uptaken at time, t
R:	Gas constant
SA:	Single Alkoxide
SEM:	Scanning Electron Microscopy
TEM:	Transmission electron microscopy
TEOS:	Tetraethyltho silicate
TG:	Thermo gravimetric
TGA:	Thermal gravimetric analysis
WGS:	Water gas shift
XRD:	X-ray diffraction

## List of Publications

- Kim, N., Kim, Y., Tsotsis, T.T., and Sahimi, M. “Atomistic Simulation of Nanoporous Layered Double Hydroxide Materials and their Properties. I. Structural Properties,” *J. Chem. Phys.*, 122, 2147, 2005.
- Kim, Y., Yang, W., Liu, P.K.T., Sahimi, M., and Tsotsis, T.T., “The Thermal Evolution of the Structure of a Mg-Al-CO<sub>3</sub> Layered Double Hydroxide (LDH). Sorption Reversibility Aspects,” *Ind. Eng. Chem. Res.*, 43, 4559, 2004.
- Yang, W., Kim, Y., Liu, P.K.T., Sahimi, M. and T. T. Tsotsis, “A Study by *In-Situ* Techniques of the Thermal Evolution of the Structure of a Mg-Al-CO<sub>3</sub> Layered Double Hydroxide (LDH),” *Chem. Eng. Sci.*, 57, 2945, 2002.